Tunable Coupling and Ultrastrong Interaction in Circuit Quantum Electrodynamics

Dissertation

by

Alexander Theodor Baust

Garching, 30. April 2015

Advisor: Prof. Dr. Rudolf Gross

Fakultät für Physik

Technische Universität München

TECHNISCHE UNIVERSITÄT MÜNCHEN

Fakultät für Physik
Lehrstuhl E23 für Technische Physik

Walther-Meißner-Institut für Tieftemperaturforschung
der Bayerischen Akademie der Wissenschaften

Tunable Coupling and Ultrastrong Interaction in Circuit Quantum Electrodynamics

Alexander Theodor Baust

Vollständiger Abdruck der von der Fakultät für Physik der Technischen Universität München zur Erlangung des akademischen Grades eines

Doktors der Naturwissenschaften

genehmigten Dissertation.

Vorsitzender:	Univ.-Prof. Dr. Ulrich Gerland
Prüfer der Dissertation:	1. Univ.-Prof. Dr. Rudolf Gross
	2. Univ.-Prof. Jonathan J. Finley, Ph. D.

Die Dissertation wurde am 30.04.2015 bei der Technischen Universität München eingereicht und durch die Fakultät für Physik am 09.06.2015 angenommen.

Das Schönste ist die Gipfelstunde,
die Gedanken noch ganz in der Wand,
der man soeben entstiegen ist,
und dabei schweifen die Blicke schon
wieder weiter zu einem anderen Ziel.

Hermann Buhl

Abstract

Superconducting quantum bits (qubits) coupled to coplanar waveguide resonators have not only proven to be essential building blocks of quantum information and simulation architectures, but are also capable of giving deep insight into the physics of light-matter interaction. In analogy to cavity quantum electrodynamics (QED), where atoms interact with the light field in an optical cavity, in circuit QED superconducting qubits acting as 'artificial atoms' interact with the modes of a quasi-onedimensional superconducting microwave transmission line resonator. As the mode volumes of these transmission line resonators are small compared to those of optical cavities and the dipole moments of the artificial atoms are large compared to those of their natural counterparts, the regime of strong and even ultrastrong light-matter interaction is easily achieved in circuit QED.

With increasing complexity of today's experimental setups, a profound understanding of the coupling mechanisms between the circuit QED building blocks has become a main research focus. We therefore study the influence of a Josephson junction inserted into a superconducting line shared between a galvanically coupled superconducting flux qubit and a transmission line resonator and find a nontrivial relation between the coupling strength and the junction's critical current.

For many applications it is not sufficient to engineer the coupling strength to a fixed value, but the coupling between adjacent circuits must be tunable and switchable in situ by an external control parameter. The latter becomes even more important in the light of recent proposals for quantum simulations of many-body physics. In this work, we present important experimental progress towards the development of a complete toolbox required for this purpose. In particular, we demonstrate the *flux qubit coupler*, a circuit QED setup enabling switchable and tunable coupling between two frequency-degenerate transmission line resonators mediated by a superconducting flux qubit. We provide a detailed analysis of the tunable coupling in time and frequency domain and show that the coupling between two resonators can be reduced by more than one order of magnitude. We show how the coupling can be tuned by either adjusting the magnetic flux through the qubit loop or saturating the qubit using a strong drive signal. We discuss the parameter regime for optimal coupler performance both with respect to resonator input and qubit drive power. We also show how additional resonant modes originate from the galvanic coupling of the flux qubit to the resonators and provide a detailed analysis of the mode structure. We show that one of these resonant modes is even coupled ultra-strongly to the qubit and present an unambiguous spectroscopic proof of the breakdown of the Jaynes-Cummings model.

Kurzfassung

An koplanare Wellenleiter-Resonatoren gekoppelte supraleitende Quantenbits (Qubits) haben sich nicht nur als essentielle Bausteine von Quanteninformations- und -simulationsarchitekturen erwiesen, sondern gewähren auch tiefgehende Einblicke in die Physik der Licht-Materie-Wechselwirkung. In Analogie zur Hohlraum-Quantenelektrodynamik (cavity QED oder kurz CQED), in der Atome mit den quantisierten Moden eines Lichtfeldes in einem optischen Hohlraumresonator interagieren, wechselwirken im Feld der Schaltkreis-Quantenelektrodynamik (circuit QED oder kurz cQED) supraleitende Quantenbits, die sich wie künstliche Atome verhalten, mit den quantisierten Moden eines quasi-eindimensionalen, supraleitenden Mikrowellen-Übertragungsleitungsresonators. Da die Modenvolumina solcher Übertragungsleitungsresonatoren klein im Vergleich zu denen optischer Hohlraumresonatoren sind und die Dipolmomente von künstlichen Atomen groß im Vergleich zu denen ihrer natürlichen Gegenstücke sind, kann das Regime der starken und sogar der ultrastarken Licht-Materie-Wechselwirkung in der Schaltkreis-Quantenelektrodynamik leicht erreicht werden.

Mit zunehmender Komplexität heutiger Versuchsanordnungen ist ein tiefgreifendes Verständnis der Kopplungsmechanismen zwischen den einzelnen Bausteinen der Schaltkreis-QED zu einem zentralen Forschungsschwerpunkt geworden. Deshalb untersuchen wir den Einfluss eines Josephson-Kontaktes, der sich in dem gemeinsamen Zweig eines galvanisch gekoppelten Flussquantenbits und eines Übertragungsleitungsresonators befindet, und finden einen nichttrivialen Zusammenhang zwischen der Kopplungsstärke und dem kritischen Strom des Kontaktes.

Für viele Anwendungen ist es jedoch nicht ausreichend, die Kopplungsstärke konstruktiv auf einen vorgegebenen Wert einzustellen. Es ist vielmehr notwendig, die Kopplungsstärke zwischen angrenzenden Schaltkreisen in situ mit Hilfe eines von außen einstellbaren Kontrollparameters abstimmen und schalten zu können. Dies ist insbesondere vor dem Hintergrund jüngster Exposés zu Quantensimulationen im Bereich der Vielteilchen-Physik von großer Bedeutung. In dieser Arbeit stellen wir wichtige experimentelle Fortschritte hin zur Realisierung eines Baukastens zu diesem Zweck vor. Insbesondere demonstrieren wir den *Flussquantenbitkoppler*, einen Schaltkreis-QED-Versuchsaufbau, der eine über ein supraleitendes Flussquantenbit vermittelte schaltbare und abstimmbare Kopplung zwischen zwei frequenzentarteten Übertragungsleitungsresonatoren ermöglicht. Wir stellen eine detaillierte Analyse der abstimmbaren Kopplung in der Zeit- und Frequenzdomäne zur Verfügung und zeigen, dass die Kopplung zwischen zwei Resonatoren um mehr als eine Größenordnung reduziert werden kann. Wir zeigen, dass die Kopplung entweder durch Anlegen eines magnetischen Flusses am Qubit oder durch Anregung des Qubits mittels eines starken Mikrowellensignals abgestimmt werden kann. Wir diskutieren den Parameterraum im Hinblick auf Resonator-Eingangsleistung und Qubit-Anregungsleistung, bei dem die optimale Leistungsfähigkeit des Kopplers erreicht wird.

Wir zeigen auch, dass die galvanische Kopplung des Flussqubits an die beiden Resonatoren zur Entstehung von zusätzlichen resonanten Moden führt und stellen eine detaillierte Untersuchung der Modenstruktur zur Verfügung. Wir zeigen darüber hinaus, dass eine dieser Moden ultrastark an das Qubit gekoppelt ist und weisen nach, dass in diesem Fall eine Beschreibung mit dem Jaynes-Cummings-Modell nicht mehr möglich ist.

Contents

Page

List of Figures

Introduction

Over the last decade, the research field of circuit quantum electrodynamics (QED) has evolved into a powerful experimental platform for the study of light-matter interaction, fundamental aspects of quantum mechanics, quantum information processing and, recently, also quantum simulation [1, 2]. It was already shown in the late 1990s that quantum two-level systems, referred to as quantum bits or qubits, can be realized by macroscopic devices comprised of billions of atoms and electrons and that coherent control of quantum states can be done by means of such devices [3, 4]. The field of circuit QED started with the seminal work of Wallraff *et al.* [5] when a Cooper pair box qubit [6] was coupled to a superconducting microwave transmission line resonator. This experiment can be seen as the first solid-state implementation of the prototypical cavity quantum electrodynamics experiment where the light field confined in a three-dimensional optical cavity interacts with a single atom [7–11]. Achieving the regime of *strong coupling*, where the coupling strength between light field and atom is large compared to the decay rates of the atom and the optical cavity, is hard to achieve in the cavity QED architecture due to the large mode volumes of the three-dimensional optical cavities and the small dipole moments of atoms. In the field of circuit QED, however, the small mode volumes of quasi-one-dimensional superconducting resonators in combination with the large dipole moments of the micrometer-sized quantum bits make the regime of strong coupling easily achievable even if decay rates of the artificial solid-state atoms are significant.

As a consequence, it was soon recognized that the circuit QED architecture provides all necessary components to reach the long-term goal of realizing a universal quantum computer based on five criteria formulated by DiVincenzo [12]. In the early years of circuit QED, an important task was the development of different types of superconducting qubits with long coherence times. Today, the most widespread types are the transmon qubit [13–15], where the quantum information is encoded into different excitation states of a nonlinear superconducting LC-resonator and the flux qubit [16–19] where the qubit states are symmetric and antisymmetric superpositions of clock- and counter-clockwise circulating persistent currents in a superconducting loop intersected by three or four Josephson junctions. Improved fabrication methods for both qubits and resonators provided coherence times long enough to implement single- and multiple qubit gates [20–23] and to perform proof-of-principle experiments representing important steps towards a universal quantum computation architectures. The latter include protocols for prime factor calculation [24] or quantum error correction [25, 26]. Furthermore, specialized qubit designs have been introduced [27] as the main building block of the surface code [28, 29] which, as of today, seems to be the most promising architecture for a universal quantum computer. The next critical steps towards a universal quantum computer are the realization of a logical memory with longer lifetimes than physical qubits and operations on logical qubits [2].

However, the applications of the circuit QED architecture are not limited to quantum information processing. The quantum mechanical resemblance of quantum bits to atoms allows to gain insight into fundamental aspects of quantum mechanics such as nonclassical states of light [30–32], entanglement [33, 34], quantum teleportation [35, 36] or regimes of light-matter-interaction not accessible with atoms [37–39]. Furthermore, the circuit QED architecture also allows to model quantum systems which are difficult or even impossible to study in the laboratory and are impossible to simulate using classical computers [40, 41]. A good example is the dynamical Casimir effect [42], where a superconducting circuit is used to model a mirror undergoing relativistic motion. Today, one major focus of quantum simulation is many-body physics of interacting spin systems [43–46] described by the Bose-Hubbard model [47] which aims at observing the transition between the Mott insulator regime and the regime of superfluidity [48, 49]. Furthermore, there is a proposal to simulate the regime of ultrastrong coupling with a standard circuit QED setup [50]. Such a simulation can not only be used to gain further insight into physics beyond the Jaynes-Cummings-model [51], but the fact that this regime can also be accessed directly in experiments [37, 39] also allows to compare the predictions of quantum simulations with experimental findings.

With increasing experimental complexity and the demand to integrate more and more components such as qubits and resonators into the respective setups, the coupling between individual building blocks has become a very important research topic in circuit QED. One main focus is on engineering the coupling strength between qubits and resonators. A good example is the coupling strength between a flux qubit and a transmission line resonator which can be engineered in a range spanning several orders of magnitude [52] by coupling the qubit either non-galvanically or galvanically to the signal line of the resonator. In the latter case, the coupling strength can be enhanced by inserting an additional Josephson junction into the shared branch between qubit and signal line [37, 51]. However, a systematic study of the coupling strengths in galvanically coupled qubit-resonator systems has yet to be done. Furthermore, the maximum qubit-resonator coupling strength that can be achieved in circuit QED still has to be determined.

Recent proposals for quantum simulation protocols and progress in quantum information and communication lead to increased demand for tunable coupling between individual circuit QED building blocks [48, 49]. While the coupling between qubits and resonators can be switched off by tuning the qubit away from the resonator [24, 25, 29], dedicated coupler circuits are required to realize tunable and switchable coupling between two fixed-frequency devices such as resonators. For instance, single Josephson junctions and SQUIDs have been used as coupler circuits since their inductance can take negative values and can therefore compensate the mutual inductance between inductively coupled circuit QED building blocks. Furthermore, their inductance can be tuned using external control parameters such as bias currents or external magnetic flux. In this way, the catch and release of photons in a microwave resonator has been demonstrated [53, 54]. Furthermore, Josephson junctions and SQUIDs have also been used as tunable couplers between two qubits [27, 55–57] or between a single qubit and a resonator [58]. In this work, we report on the successful realization of the flux qubit coupler, a device allowing for tunable and switchable coupling between frequency-degenerate transmission line resonators.

This thesis is divided into four parts. In chapter one, we introduce the theoretical foundations of circuit quantum electrodynamics. We provide a detailed description of the building blocks relevant for our work, namely transmission line resonators and superconducting flux qubits. The dipolar interaction between the latter is described by the quantum Rabi model which, in the case of sufficiently small coupling strengths, can be approximated by the renowned Jaynes-Cummings-model. Coupling a flux qubit to two frequency-degenerate, geometrically coupled transmission line resonators constitutes the quantum switch architecture. We provide a detailed description of the corresponding Hamiltonian and discuss how the flux applied to the qubit and the qubit population can be used to tune and switch the coupling between the two resonators.

In the second chapter, we discuss the experimental techniques required for our measurements. The samples investigated in the course of this thesis are operated at millikelvin temperatures which requires complex experimental setups allowing us to deliver dc and microwave signals from room temperature to the samples and also demand specialized techniques for signal detection. We show how the characteristic transition frequencies of coupled qubit-resonator systems can be inferred from transmission spectroscopy measurements and how time-domain measurements provide access to the coherence properties of our quantum bits.

In chapter three, we study a flux qubit coupled galvanically to the signal line of a transmission line resonator where the coupling strength is determined by an additional Josephson junction inserted into the shared branch between qubit and resonator signal line. Our findings show that there is a nontrivial dependence of the coupling strength on the critical current of the coupling Josephson junction. This provides a starting point for further systematic studies of galvanically coupled qubit-resonator systems with and without coupling junction. Furthermore, we test our time-domain spectroscopy setup by characterizing the energy decay rate of our qubit.

In the last chapter, we demonstrate tunable and switchable coupling between two frequency-degenerate transmission line resonators. In our setup, a flux qubit is coupled galvanically to the signal lines of two coplanar stripline resonators. We first perform a spectroscopic characterization of our sample and find that the galvanic coupling gives rise to a resonant mode which is coupled ultrastrongly to the qubit. With the demonstration of physics beyond the Jaynes-Cummings model, our sample provides interesting insights into the regime of ultrastrong light-matter interaction and also represents an important step towards a systematic understanding of galvanically coupled qubit-resonator systems. Finally, we show that the coupling between the two resonators can be tuned over more than one order of magnitude by varying the magnetic flux applied to the qubit and can be switched to the desired coupling strength by varying the qubit population. In this way, we demonstrate the working principle of the quantum switch architecture and our measurement results suggest that our work indeed adds the missing tool of tunable coupling between frequency-degenerate transmission line resonators to the circuit QED toolbox.

Chapter 1

Superconducting quantum circuits

Circuit quantum electrodynamics (QED) has become a versatile toolbox for quantum information processing, quantum simulation and the study of light-matter interaction and fundamental aspects of quantum mechanics. The circuit QED architecture is based on two classes of superconducting circuits, namely linear circuits such as resonators and nonlinear circuits such as quantum bits. In this chapter we will lay the theoretical foundations necessary to understand how macroscopic circuits with dimensions ranging from the nanometer to the centimeter range can exhibit quantum mechanical behaviour and resemble microscopic entities such as natural atoms studied in the field of cavity QED.

We begin with a short introduction to superconductivity before introducing the most important linear element in the circuit QED architecture, the coplanar waveguide resonator. Subsequently, the superconducting flux qubit is introduced and its quantum mechanical description is provided. In Sec. 1.4, the theoretical framework of circuit QED is discussed and the coupling between a linear quantum mechanical oscillator and a two-level system is studied in detail. Adding a second resonator interacting with both the qubit and the first resonator constitutes the prototypical circuit for the field of two-resonator circuit QED. We will see how the qubit can be used to tune and switch the coupling between the two resonators and how the quantum nature of the qubit can be exploited to generate non-classical states such as Greenberger-Horne-Zeilinger or Schrödinger Cat states.

1.1 Superconductivity

The effect of superconductivity was discovered in 1911 when Heike Kamerlingh Onnes investigated the temperature dependence of the resistance of mercury and found that it drops to an immeasurably small value below a certain temperature [59]. Today, this characteristic temperature is called the *transition temperature* T_c and the transition to the superconducting phase has been observed in a wide range of materials. The transition temperatures for two materials widely used in the field of circuit QED, niobium and aluminum, are given by[1] $T_{\mathrm{c,Nb}} = 9.2\,\mathrm{K}$ and $T_{\mathrm{c,Al}} = 1.2\,\mathrm{K}$.

The charge carriers of the superconducting phase are strongly correlated electrons referred to as *Cooper pairs*. Quantum mechanically, the state of the Cooper pair condensate can be described by a macroscopic wave function given by

$$\Psi_{\mathrm{sc}}(\mathbf{r},t) = \sqrt{n_{\mathrm{s}}(\mathbf{r},t)}\mathrm{e}^{\imath\theta(\mathbf{r},t)}, \tag{1.1}$$

where n_{s} is the density of Cooper pairs and $\theta(\mathbf{r},t)$ is the phase of the wave function Ψ_{sc}. At $T = 0$, for weak coupling superconductors such as Al the quasiparticle energy spectrum is separated by the energy gap $\Delta_{\mathrm{sc}}(0) \approx 1.76\, k_{\mathrm{B}} T_{\mathrm{c}}$, where k_{B} is the Boltzmann constant. For aluminum, this yields an energy gap of $2\Delta_{\mathrm{sc,Al}}(0) \approx 88\,\mathrm{GHz} \times h$ which is well above typical transition frequencies of aluminum based quantum circuits which are typically on the order of several gigahertz. However, most circuit QED experiments are conducted at finite temperatures below approx. 100 mK. The strong temperature dependence of the Cooper pair density ensures that the number of quasiparticles, i.e. (thermally) split Cooper pairs, with a continuous excitation spectrum is negligible for $T > 0$ as long as $T \ll T_{\mathrm{c}}$.

The relation between the supercurrent density [61]

$$\mathbf{J}_{\mathrm{s}} = q_{\mathrm{s}} n_{\mathrm{s}}(\mathbf{r},t) \left(\frac{\hbar}{m_{\mathrm{s}}} \nabla\theta(\mathbf{r},t) - \frac{q_{\mathrm{s}}}{m_{\mathrm{s}}} \mathbf{A}(\mathbf{r},\mathbf{t}) \right), \tag{1.2}$$

where m_{s} and q_{s} are the mass and charge of a Cooper pair and $\mathbf{A}$ is the magnetic vector potential, and the electromagnetic field in a superconductor is given by the London equations

$$\frac{\partial \Lambda \mathbf{J}_{\mathrm{s}}}{\partial t} = \mathbf{E}, \tag{1.3}$$

$$\nabla \times (\Lambda \mathbf{J}_{\mathrm{s}}) + \mathbf{b} = 0, \tag{1.4}$$

in which $\Lambda = m_{\mathrm{s}}/(n_{\mathrm{s}} q_{\mathrm{s}}^2)$ is the London coefficient, $\mathbf{E}$ is the electric field and $\mathbf{b}$ is the magnetic flux density. A notable consequence of these equations is that magnetic fields are expelled from the insides of superconductors, i.e. $\mathbf{b} = 0$, when cooled down below their transition temperature. However, near the surface the magnetic flux density is not completely cancelled, but decays exponentially towards the inside of the superconductor.

[1] The stated values are valid for bulk material. We note that the transition temperatures increase for thin Al films [60]. However, for the samples discussed in this thesis the film thicknesses justify using the transition temperatures of the respective bulk materials.

The corresponding length scale is given by the London penetration depth,

$$\lambda_{\mathrm{L}} = \sqrt{\frac{m_{\mathrm{s}}}{\mu_0 n_{\mathrm{s}} q_{\mathrm{s}}^2}}, \tag{1.5}$$

where μ_0 is the vacuum permeability. For bulk aluminum, the London penetration depth is 16 nm [62], however, we note that its effective value increases dramatically for thin films. For the particular 90 nm thin Al films used in this work, one finds $\lambda_{\mathrm{L,Al,90nm}} \approx 190\,\mathrm{nm}$ [63].

1.2 Coplanar waveguide resonators

In architectures for quantum information processing, resonators serve two main purposes. On the one hand, they act as quantum buses transferring quantum information, i.e. data encoded in photonic states, from one building block to another. On the other hand, resonators are used to store quantum information. In experiments, mostly resonators in a quasi-one-dimensional transmission line geometry fabricated in thin-film technology on dielectric substrates are used. We start with a classical description of transmission lines and introduce their characteristic parameters. We present two important transmission line resonator designs, namely the coplanar waveguide and the coplanar stripline resonator.

If a resonator is cooled down to low temperatures T such that $\hbar\omega_{\mathrm{R}} \gg k_{\mathrm{B}}T$, where ω_{R} is the resonant frequency and k_{B} is the Boltzmann constant, classical electric quantities such as magnetic flux and electric charge are promoted to quantum mechanical operators and the resonator can be modeled as a quantum harmonic oscillator. Finally, we discuss the case of two coupled resonators and give a short introduction to input-output theory, a powerful mathematical tool allowing to calculate the scattering parameters of coupled resonators analytically.

1.2.1 Transmission line theory

Electrically conductive structures designed to carry alternating currents at radio frequencies are subsumed under the term *transmission lines*. As the wavelengths of the transmitted signals typically are on the same order of magnitude as the physical dimensions of the transmission line, electrical quantities such as voltages and currents can vary over its length [64]. Therefore, transmission lines are referred to as *distributed element circuits* in contrast to *lumped element circuits* whose electrical components such as inductors, capacitors or resistors exhibit physical dimensions which can be treated point-like as compared to the wavelengths of the transmitted electrical signals.

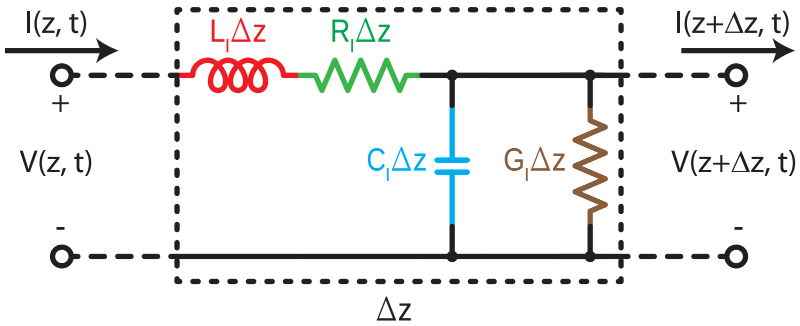

Figure 1.1: Distributed element representation of a transmission line. The transmission line is subdivided into parts of length Δz with a series inductance per unit length L_l and a series resistance per unit length R_l. The connection to ground (lower line) is modeled by a shunt capacitance per unit length C_l and a shunt conductance per unit length G_l. Voltage and current vary over the length of the transmission line.

Schematically, a transmission line can be represented as a two-wire line as shown in Fig. 1.1. A short section of length Δz can be modeled as lumped element circuit with a series inductance per unit length L_l representing the self inductance of the two conductors and a series resistance per unit length R_l taking into account the finite conductivity of the inductors. The shunt capacitance per unit length C_l arises from the close proximity of the two conductors. Dielectric losses in the material surrounding the conductors are represented by a shunt conductance per unit length G_l. For superconducting transmission lines and low-loss dielectric materials as discussed in the course of this thesis, R_l and G_l can be neglected. For a detailed description of transmission line theory and waveguide designs, we refer to Refs. [64–66]. In what follows, we restrict ourselves to the most relevant results needed throughout this thesis.

The phase velocity of electromagnetic waves propagating along a loss-free transmission line is given by [67]

$$v_{\mathrm{ph}} = \frac{c}{\sqrt{\epsilon_{\mathrm{eff}}}} = \frac{1}{\sqrt{L_l C_l}}, \tag{1.6}$$

where c is the speed of light in vacuum and ϵ_{eff} is the effective dielectric constant. The latter is a function of the transmission line geometry and the relative permittivity of the dielectric surrounding the conductors of the transmission line [68]. The characteristic impedance Z_0 of a transmission line is given by

$$Z_0 = \sqrt{\frac{L_l}{C_l}}. \tag{1.7}$$

The characteristic impedance is a very important quantity since it defines the reflection coefficient Γ at the transition between two transmission lines with characteristic impedances Z_1 and Z_2, respectively, and is given by [64]

$$\Gamma = \frac{Z_2 - Z_1}{Z_2 + Z_1}. \tag{1.8}$$

Most microwave equipment is designed to have a characteristic impedance of $50\,\Omega$. Hence, all microwave components fabricated in-house should also be designed to that characteristic impedance in order to minimize reflections.

1.2.2 Transmission line resonators

A transmission line resonator is formed by adding boundary conditions to a section of a transmission line with finite length l. In the course of this thesis, we restrict ourselves to the case where the boundary conditions are formed by two identical capacitors C_c inserted into the signal line coupling the transmission line to an external load R_L. The distributed element representation of a capacitively coupled transmission line resonator [67] is shown in Fig. 1.2. This results in the formation of standing waves with current

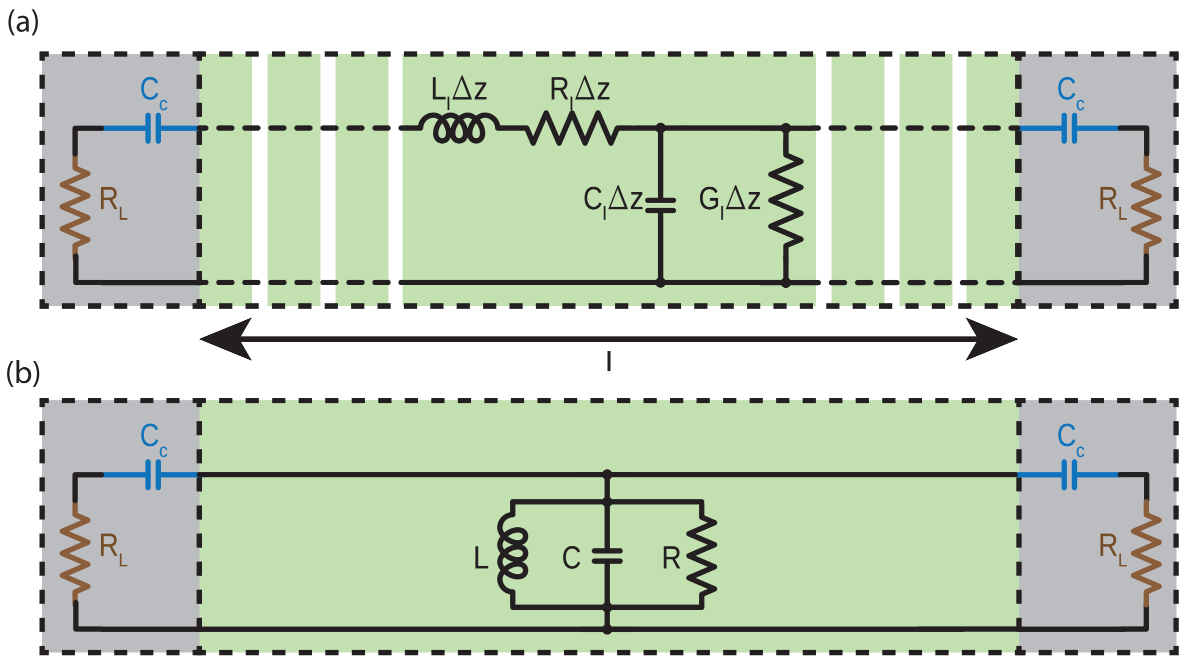

Figure 1.2: (a) Distributed element representation of a transmission line resonator. The resonator (length l, highlighted by the green rectangles) is coupled symmetrically to an external load R_L via the coupling capacitors C_c (grey rectangles). (b) Parallel LCR-representation of the transmission line resonator.

nodes at the position of the coupling capacitors. The only modes fulfilling this boundary condition are those with wavelengths

$$\lambda_n = \frac{2l}{n}, \tag{1.9}$$

where n is a non-negative integer. Since the length l of the resonator matches half the wavelength of the fundamental resonant mode, a transmission line coupled capacitively on both sides is also called *half-wavelength resonator* or $\lambda/2$-*resonator*. Using Eq. (1.6), we can calculate the resonant frequency of the n-th mode as

$$f_n = \frac{\omega_n}{2\pi} = \frac{v_{\mathrm{ph}}}{\lambda_n} = n\frac{c}{2l\sqrt{\epsilon_{\mathrm{eff}}}} = \frac{n}{2l\sqrt{L_l C_l}} = \frac{n}{2\sqrt{\tilde{L}\tilde{C}}}, \tag{1.10}$$

where $\tilde{L} \equiv L_l l$ is the total inductance and $\tilde{C} \equiv C_l l$ is the total capacitance of the transmission line resonator. We note that large coupling capacitors C_{c} shift the resonance frequency of the n-th mode by [67]

$$\delta\omega \approx -\omega_n \frac{C_{\mathrm{c}}}{C}. \tag{1.11}$$

Close to resonance, the transmission line resonator can be modeled as a lumped element, parallel LCR-circuit as shown in Fig. 1.2(b). The inductance L_n, capacitance C and resistance R modeling the resonant mode n are given by [67]

$$L_n = \frac{2L_l l}{n^2\pi^2}, \tag{1.12}$$

$$C = \frac{C_l l}{2}, \tag{1.13}$$

$$R = \frac{Z_0}{\alpha l}, \tag{1.14}$$

where we introduce the attenuation constant α. We note that $\alpha = 0$ for a lossless transmission line resonator. Neglecting the frequency shift introduced by the coupling capacitors, the resonant frequency of the mode n is then given by $\omega_n = 1/\sqrt{L_n C}$.

Another very important characteristic quantity of a resonator is its quality factor Q. The general definition for a mode with resonant frequency ω_n is given by [64]

$$Q = \omega_n \frac{\text{time-average energy stored}}{\text{energy loss per second}}. \tag{1.15}$$

Introducing the decay rate of each resonant mode $\gamma_n = 2\pi\delta f_n$, the corresponding quality factor is given by

$$Q_n = \frac{f_n}{\delta f_n} = \frac{\omega_n}{\kappa_n}. \tag{1.16}$$

In most experiments, all resonators are connected to external circuitry, in most cases by means of coupling capacitors. The energy loss per second in Eq. (1.15) then is a combination of internal energy loss mechanisms and transfer of energy to that external circuitry. The former are taken into account by the *internal* quality factor Q_{int} and the latter by the *external* quality factor Q_{ext}. The quality factor taking into account both loss channels is referred to as *loaded* quality factor Q_{L} and is given by [64]

$$\frac{1}{Q_{\mathrm{L}}} = \frac{1}{Q_{\mathrm{int}}} + \frac{1}{Q_{\mathrm{ext}}}. \tag{1.17}$$

The internal quality factor is linked to the attenuation constant α by $Q_{\mathrm{int}} = n\pi/2\alpha l$. For a detailed description of the various loss mechanisms we refer the reader to Refs. [67, 69–71]. The external quality factor can be engineered to the desired value by adjusting the coupling capacitors C_{c}. If Q_{L} is governed by the external quality factor, i.e. $Q_{\mathrm{ext}} \ll Q_{\mathrm{int}}$, the resonator is referred to as *overcoupled*. Contrarily, if internal losses dominate over the transfer of stored energy to the feed lines via the coupling capacitors (i.e. $Q_{\mathrm{ext}} \gg Q_{\mathrm{int}}$), the resonator is referred to as *undercoupled* [67]. Today, the highest internal quality factors that can be reached with coplanar transmission line resonators exceed one million[2] [72]. Thus far, higher internal quality factors can only be reached in the emerging field of three-dimensional circuit QED, where 3D-cavities with $Q_{\mathrm{int}} = 7.4 \cdot 10^8$, corresponding to a photon lifetime of 10 ms, have been demonstrated [73].

The (loaded) quality factor also manifests itself in transmission measurements through the resonator. Each resonant mode n exhibits a Lorentzian line shape given by

$$F_{\mathrm{Lor},n}(f) = A_n \frac{\delta f_n}{(f - f_n)^2 + \delta f_n^2/4} \tag{1.18}$$

where f_n is the resonant frequency, A_n is the insertion loss and δf_n is the full width at half maximum of the resonance.

1.2.2.1 Kinetic inductance

We briefly come back to the inductance per unit length indicated in Fig. 1.1. For superconducting lines, it is comprised of a purely geometric contribution and the kinetic inductance. While the former accounts for the electric energy stored external to the conductor, the latter accounts for the kinetic energy of the charge carriers of the supercurrent [74]. For superconducting lines with dimensions much larger than the London penetration depth λ_{L}, the kinetic contribution to the inductance per unit length can typically be neglected. However, for thin superconducting lines the kinetic inductance L_{kin} has to

[2] We note that the achievable quality factors depend strongly on resonant frequency and material of the respective coplanar transmission line resonators.

be taken into account and is given by [74–76]

$$L_{\mathrm{kin}} = \mu_0 \lambda_{\mathrm{L}}^2 \frac{l}{S}, \tag{1.19}$$

where l is the length and S is the cross section of the line.

1.2.2.2 Coplanar waveguide resonator

In the field of circuit QED, one of the most widespread transmission line resonator designs is the coplanar waveguide resonator (CPW). It is sketched in Fig. 1.3. The signal line is realized as a thin strip line of width W whose ends form one half of the capacitors determining the coupling to the feed lines. The ground planes are separated by a distance G from the signal line and are wide enough that they can be treated as semi-infinite [66]. Signal line and ground planes are fabricated on a dielectric substrate with relative dielectric constant ϵ_{r}. Since the resonator is typically mounted inside a box made of conducting material (e.g. gold-plated copper), we consider an additional ground plane on the back side of the substrate. This architecture is referred to as *conductor-backed* CPW. We note that the theoretical model described above is only valid if all ground planes are at the same electrical potential. In experiments, this is ensured by connecting all ground planes with low-resistance electric conductors such as bond wires.

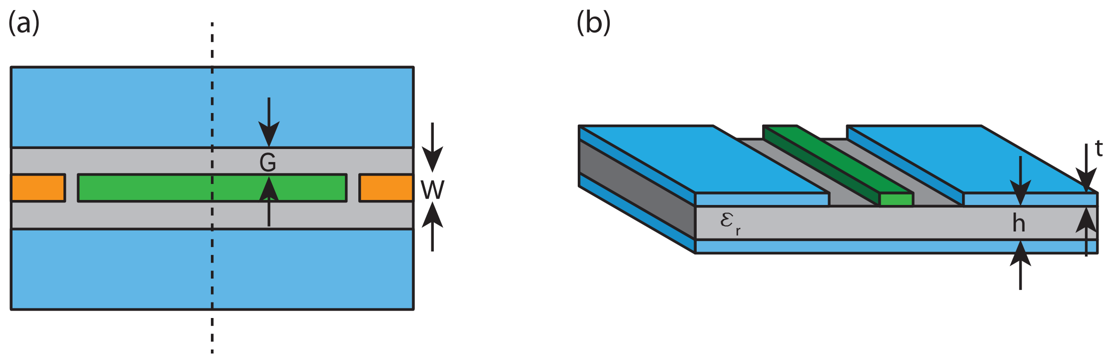

Figure 1.3: The conductor-backed coplanar waveguide resonator. (a) Top view. The signal line is shown in green, the feed lines in orange, the ground planes in blue, and the dielectric substrate in grey. Subfigure (b) shows the cut along the dashed black line. (b) Side view. The lower ground plane (shown in blue) takes the effects of a conducting sample package into account. The space above the top ground planes and the signal line is assumed to be vacuum.

In order to design the CPW to the desired frequency and impedance, the effective dielectric constant ϵ_{eff}, cf. Eq. (1.10) has to be known. For the conductor-backed CPW, it can be calculated analytically following Ref. [68] from the CPW geometry and the substrate relative dielectric constant ϵ_{r}.

1.2.2.3 Coplanar stripline resonator

The coplanar stripline resonator layout is very similar to that of the CPW. The only qualitative difference is that one of the two ground planes is missing, see Fig. 1.4. We will see in Sec. 4.1 why this layout is advantageous in certain scenarios. Again, there are analytical expressions allowing to calculate resonant frequency and impedance from ϵ_r of the substrate and the geometry of the coplanar stripline [77].

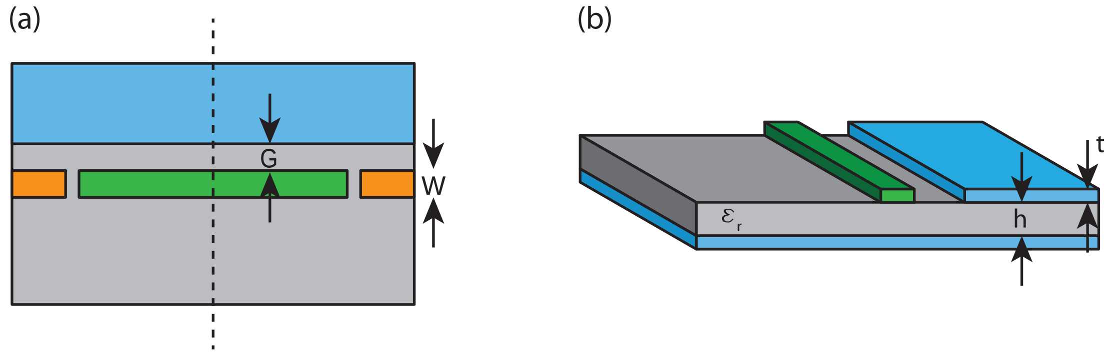

Figure 1.4: The conductor-backed coplanar stripline resonator. In contrast to the conductor-backed CPW, it misses one of the semi-infinite ground planes. (a) Top view. (b) Side view, cut along the dashed black line.

1.2.3 Quantum mechanical description

Thus far, the distributed transmission line resonator has been modeled as a parallel lumped element circuit as shown in Fig. 1.2(b). Next, we turn to a quantum mechanical description where electric quantities are represented by quantum mechanical operators. The derivation presented below follows mainly Ref. [78].

The classical Hamiltonian of the lossless parallel LC-circuit is given by

$$H_{\mathrm{LC}} = \frac{\Phi^2}{2L} + \frac{q^2}{2C} \tag{1.20}$$

where $\Phi = LI$ is the flux through the inductor. The potential energy of the capacitor is $(q - q_0)^2/2C$, where q_0 is the offset charge of the capacitor. The current through the inductor and the voltage at the node connecting the inductor and the capacitor are obtained from Hamilton's equations of motion,

$$\dot{q} = \frac{\partial H_{\mathrm{LC}}}{\partial \Phi} = \frac{\Phi}{L} = I, \tag{1.21}$$

$$\dot{\Phi} = -\frac{\partial H_{\mathrm{LC}}}{\partial q} = -\frac{q}{C} = V. \tag{1.22}$$

The quantities q and Φ correspond to generalized canonical position and momentum variables. Hence, they can be mapped to quantum mechanical operators $\hat{q}$ and $\hat{\Phi}$ obeying the commutation relation

$$[\hat{\Phi},\hat{q}] = -\imath\hbar. \tag{1.23}$$

With the resonant frequency $\omega_{\mathrm{R}} = 1/\sqrt{LC}$, we find

$$\hat{H}_{\mathrm{LC}} = \hbar\omega_{\mathrm{R}}\left(\hat{a}^\dagger\hat{a} + \frac{1}{2}\right). \tag{1.24}$$

The bosonic annihilation and creation operators are given by

$$\hat{a} = +\imath\frac{1}{\sqrt{2L\hbar\omega_{\mathrm{R}}}}\hat{\Phi} + \frac{1}{\sqrt{2C\hbar\omega_{\mathrm{R}}}}\hat{q}, \tag{1.25}$$

$$\hat{a}^\dagger = -\imath\frac{1}{\sqrt{2L\hbar\omega_{\mathrm{R}}}}\hat{\Phi} + \frac{1}{\sqrt{2C\hbar\omega_{\mathrm{R}}}}\hat{q}, \tag{1.26}$$

obeying the commutation relation

$$[\hat{a},\hat{a}^\dagger] = 1. \tag{1.27}$$

Using the above equation and the characteristic impedance of Eq. (1.7), we can express the charge and flux operators in terms of the annihilation and creation operators as

$$\hat{q} = \sqrt{\frac{\hbar}{2Z_0}}(\hat{a}^\dagger + \hat{a}) \quad \text{and} \tag{1.28}$$

$$\hat{\Phi} = \imath\sqrt{\frac{\hbar Z_0}{2}}(\hat{a}^\dagger - \hat{a}) \tag{1.29}$$

in analogy to a massive particle moving in a harmonic potential [79].

1.2.4 Coupled resonators

We consider the scenario depicted in Fig. 1.5 where two resonators A and B with identical resonant frequency ω_{R} are coupled. Depending on the current and voltage distribution in the resonators, the coupling can be of capacitive (for nonzero voltages) or inductive (for nonzero currents) nature or can be a combination of both. The coupling rate, here and in what follows denoted by g_{AB}, is assumed to be small compared to the resonant frequency. The Hamiltonian of the two coupled resonators then reads

$$\hat{H}_{\mathrm{RR}} = \hbar\omega_{\mathrm{R}}\left(\hat{a}^\dagger\hat{a} + \frac{1}{2}\right) + \hbar\omega_{\mathrm{R}}\left(\hat{b}^\dagger\hat{b} + \frac{1}{2}\right) + \hbar g_{\mathrm{AB}}\left(\hat{a}\hat{b}^\dagger + \hat{a}^\dagger\hat{b}\right), \tag{1.30}$$

in which $\hat{a}$ ($\hat{b}$) and $\hat{a}^\dagger$ ($\hat{b}^\dagger$) denote the annihilation and creation operators of resonator A (B).

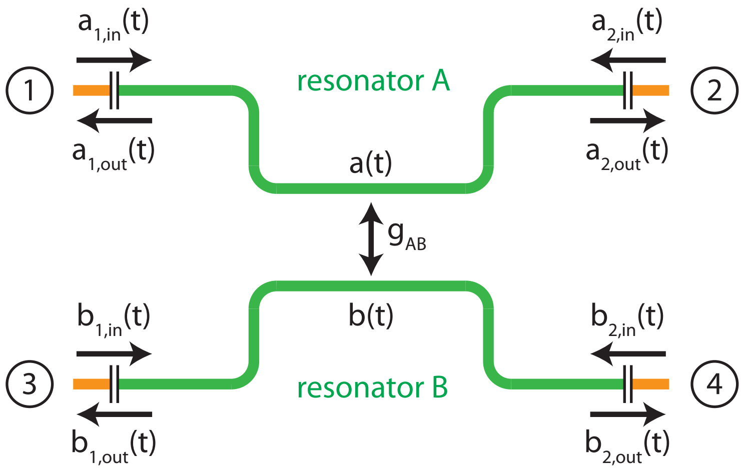

Figure 1.5: Two coupled resonators A and B. The coupling strength is given by g_{AB}. The encircled numbers are used to identify the ports and thus the S-parameters of the coupled resonators. The internal fields of resonator A and B are denoted by $a(t)$ and $b(t)$, respectively. The corresponding input (output) fields are denoted by $a_{1,2,\mathrm{in}}$ ($a_{1,2,\mathrm{out}}$) for resonator A and analogously for resonator B.

The Hamiltonian of Eq. (1.30) can be diagonalized introducing the operators

$$\hat{c}_{\pm} = \frac{1}{\sqrt{2}}\left(\hat{a} \pm \hat{b}\right) \quad \text{and} \quad \hat{c}_{\pm}^{\dagger} = \frac{1}{\sqrt{2}}\left(\hat{a}^{\dagger} \pm \hat{b}^{\dagger}\right), \tag{1.31}$$

yielding

$$\hat{H}_{\mathrm{RR}} = \hbar(\omega_{\mathrm{R}} - g_{\mathrm{AB}})\left(\hat{c}_{-}^{\dagger}\hat{c}_{-} + \frac{1}{2}\right) + \hbar(\omega_{\mathrm{R}} + g_{\mathrm{AB}})\left(\hat{c}_{+}^{\dagger}\hat{c}_{+} + \frac{1}{2}\right). \tag{1.32}$$

This result corresponds to a linear combination of two harmonic oscillators with resonant frequencies $\omega_{\mathrm{R}} \pm g_{\mathrm{AB}}$. The eigenmodes $\hat{c}_{-}$ and $\hat{c}_{+}$ correspond to in-phase and out-of-phase oscillating currents in the resonators and are referred to as the parallel mode and antiparallel mode, respectively.

Next, we analyze the scattering parameters, i.e. the frequency response of two coupled resonators. To this end, we use input-output theory as presented in Ref. [80].

We define the Fourier components of the fields $\hat{a}(t)$ and $\hat{b}(t)$ inside the resonators A and B as

$$\hat{a}(t) = \frac{1}{\sqrt{2\pi}} \int_{-\infty}^{\infty} \mathrm{e}^{\imath\omega(t-t_0)}\hat{a}(\omega)\mathrm{d}\omega \tag{1.33}$$

$$\hat{b}(t) = \frac{1}{\sqrt{2\pi}} \int_{-\infty}^{\infty} \mathrm{e}^{\imath\omega(t-t_0)}\hat{b}(\omega)\mathrm{d}\omega. \tag{1.34}$$

The Fourier components of the input and output fields are defined in the same way. We denote the Fourier components of the input fields by $\hat{a}_{1,\mathrm{in}}$ and $\hat{a}_{2,\mathrm{in}}$ for resonator A and by $\hat{b}_{1,\mathrm{in}}$ and $\hat{b}_{2,\mathrm{in}}$ for resonator B, cf. Fig. 1.5. Furthermore, we no longer restrict ourselves to the case of identical resonators, instead, we consider two resonators with resonant frequencies ω_A and ω_B and decay rates κ_A and κ_B. However, we assume equal coupling rates to the two feed lines for both resonators. Again, we denote the coupling between the resonators by g_AB. The Hamiltonian of the two coupled resonators then reads

$$\hat{H}_\mathrm{AB} = \hbar\omega_\mathrm{A}\left(\hat{a}^\dagger\hat{a} + \frac{1}{2}\right) + \hbar\omega_\mathrm{B}\left(\hat{b}^\dagger\hat{b} + \frac{1}{2}\right) + \hbar g_\mathrm{AB}\left(\hat{a}\hat{b}^\dagger + \hat{a}^\dagger\hat{b}\right), \tag{1.35}$$

Following Ref. [80], the Heisenberg equations of motion for the fields inside resonators A and B read

$$\frac{\mathrm{d}\hat{a}(t)}{\mathrm{d}t} = -\frac{\imath}{\hbar}[\hat{a}(t),\hat{H}_\mathrm{AB}] - \kappa_\mathrm{A}\hat{a}(t) + \sqrt{\kappa_\mathrm{A}}\hat{a}_{1,\mathrm{in}}(t) + \sqrt{\kappa_\mathrm{A}}\hat{a}_{2,\mathrm{in}}(t) \tag{1.36}$$

$$\frac{\mathrm{d}\hat{b}(t)}{\mathrm{d}t} = -\frac{\imath}{\hbar}[\hat{b}(t),\hat{H}_\mathrm{AB}] - \kappa_\mathrm{B}\hat{b}(t) + \sqrt{\kappa_\mathrm{B}}\hat{b}_{1,\mathrm{in}}(t) + \sqrt{\kappa_\mathrm{B}}\hat{b}_{2,\mathrm{in}}(t). \tag{1.37}$$

The commutators are calculated to

$$[\hat{a}(t),\hat{H}_\mathrm{AB}] = \hbar\omega_\mathrm{A}\hat{a}(t) + \hbar g_\mathrm{AB}\hat{b}(t) \quad \text{and} \tag{1.38}$$

$$[\hat{b}(t),\hat{H}_\mathrm{AB}] = \hbar\omega_\mathrm{B}\hat{b}(t) + \hbar g_\mathrm{AB}\hat{a}(t), \tag{1.39}$$

yielding a system of two coupled differential equations:

$$\begin{aligned}
0 &= -\imath(\omega_\mathrm{A} - \omega)\hat{a}(t) - \kappa_\mathrm{A}\hat{a}(t) - \imath g_\mathrm{AB}\hat{b}(t) + \sqrt{\kappa_\mathrm{A}}\hat{a}_{1,\mathrm{in}}(t) + \sqrt{\kappa_\mathrm{A}}\hat{a}_{2,\mathrm{in}}(t) \\
0 &= -\imath(\omega_\mathrm{B} - \omega)\hat{b}(t) - \kappa_\mathrm{B}\hat{b}(t) - \imath g_\mathrm{AB}\hat{a}(t) + \sqrt{\kappa_\mathrm{B}}\hat{b}_{1,\mathrm{in}}(t) + \sqrt{\kappa_\mathrm{B}}\hat{b}_{2,\mathrm{in}}(t)
\end{aligned} \tag{1.40}$$

The relations between input and output fields are given by

$$\begin{aligned}
\hat{a}_{1,\mathrm{out}}(t) + \hat{a}_{1,\mathrm{in}}(t) &= \sqrt{\kappa_\mathrm{A}}\hat{a}(t), \\
\hat{a}_{2,\mathrm{out}}(t) + \hat{a}_{2,\mathrm{in}}(t) &= \sqrt{\kappa_\mathrm{A}}\hat{a}(t), \\
\hat{b}_{1,\mathrm{out}}(t) + \hat{b}_{1,\mathrm{in}}(t) &= \sqrt{\kappa_\mathrm{B}}\hat{b}(t), \\
\hat{b}_{2,\mathrm{out}}(t) + \hat{b}_{2,\mathrm{in}}(t) &= \sqrt{\kappa_\mathrm{B}}\hat{b}(t).
\end{aligned} \tag{1.41}$$

To derive the scattering parameters of the coupled resonators, we identify the classical input (output) fields $a_{1,\mathrm{in(out)}}$, $a_{2,\mathrm{in(out)}}$, $b_{1,\mathrm{in(out)}}$ and $b_{2,\mathrm{in(out)}}$ with the complex envelope functions of the corresponding field operators [81, 82]. Furthermore, we assume that an input field is applied only to port 1, cf. Fig. 1.5, and the input fields at all other ports are zero, i.e. $a_{2,\mathrm{in}}(t) = b_{1,\mathrm{in}}(t) = b_{2,\mathrm{in}}(t) = 0$. With these boundary conditions, the coupled differential equations (1.40) can be solved analytically, yielding the expressions

$$S_{11} = \left|\frac{a_{1,\mathrm{out}}}{a_{1,\mathrm{in}}}\right| = \left|\frac{-g_{\mathrm{AB}}^2 + (\omega-\omega_{\mathrm{A}})(\omega-\omega_{\mathrm{B}}+\imath\kappa_{\mathrm{B}})}{g_{\mathrm{AB}}^2 - (\omega-\omega_{\mathrm{A}}+\imath\kappa_{\mathrm{A}})(\omega-\omega_{\mathrm{B}}+\imath\kappa_{\mathrm{B}})}\right| \tag{1.42}$$

$$S_{21} = \left|\frac{a_{2,\mathrm{out}}}{a_{1,\mathrm{in}}}\right| = \left|\frac{\kappa_{\mathrm{A}}(\imath(-\omega+\omega_{\mathrm{B}})+\kappa_{\mathrm{B}})}{g_{\mathrm{AB}}^2 - (\omega-\omega_{\mathrm{A}}+\imath\kappa_{\mathrm{A}})(\omega-\omega_{\mathrm{B}}+\imath\kappa_{\mathrm{B}})}\right| \tag{1.43}$$

$$S_{31} = \left|\frac{b_{1,\mathrm{out}}}{a_{1,\mathrm{in}}}\right| = \left|\frac{g_{\mathrm{AB}}\sqrt{\kappa_{\mathrm{A}}\kappa_{\mathrm{B}}}}{g_{\mathrm{AB}}^2 - (\omega-\omega_{\mathrm{A}}+\imath\kappa_{\mathrm{A}})(\omega-\omega_{\mathrm{B}}+\imath\kappa_{\mathrm{B}})}\right| \tag{1.44}$$

$$S_{41} = \left|\frac{b_{2,\mathrm{out}}}{a_{1,\mathrm{in}}}\right| = \left|\frac{g_{\mathrm{AB}}\sqrt{\kappa_{\mathrm{A}}\kappa_{\mathrm{B}}}}{g_{\mathrm{AB}}^2 - (\omega-\omega_{\mathrm{A}}+\imath\kappa_{\mathrm{A}})(\omega-\omega_{\mathrm{B}}+\imath\kappa_{\mathrm{B}})}\right|. \tag{1.45}$$

Figure 1.6 shows theoretical calculations for the S-parameters S_{21} and S_{31} of two coupled resonators. In Fig. 1.6(a), identical resonators are assumed. Two transmission maxima at $\omega_{\mathrm{A}} \pm g_{\mathrm{AB}} = \omega_{\mathrm{B}} \pm g_{\mathrm{AB}}$ with identical relative transmission are observed. In Fig. 1.6(b), however, we assume unequal resonant frequencies while we leave the other parameters unchanged. Still, we observe two transmission maxima, however, there is no analytic solution for their frequencies and the respective relative transmissions.

Next, we discuss the transmission minimum of S_{21} referred to as antiresonance [83]. It occurs at $\omega = \omega_{\mathrm{B}}$, cf. Eq. (1.43). In the same way, if also S_{34}, i.e. the transmission through resonator B, is experimentally accessible, the bare resonant frequencies of both resonators can be determined with high precision as shown in Fig. 1.6(d). We will use these findings to characterize the flux qubit tunable coupler in Sec. 4.2.1.

1.3 Superconducting three Josephson junction flux qubit

Even though linear superconducting devices such as transmission line resonators show quantum mechanical behaviour, they are not sufficient for most quantum information processing applications. To this end, non-linear devices have to be used. Today, one of the most important building blocks of the circuit QED architecture is the Josephson junction since it represents the only known electronic element which is both dissipationless and non-linear [84]. After a short introduction to Josephson physics and flux quantisation, we introduce the flux qubit, a superconducting loop intersected by three Josephson junctions. In this circuit, the quantum states correspond to symmetric and antisymmetric superpositions of clockwise and counterclockwise persistent currents. In contrast to another widely used quantum bit, the transmon [13, 14], the flux qubit comes very close to an ideal quantum mechanical two-level-system as, due to the large anharmonicity of

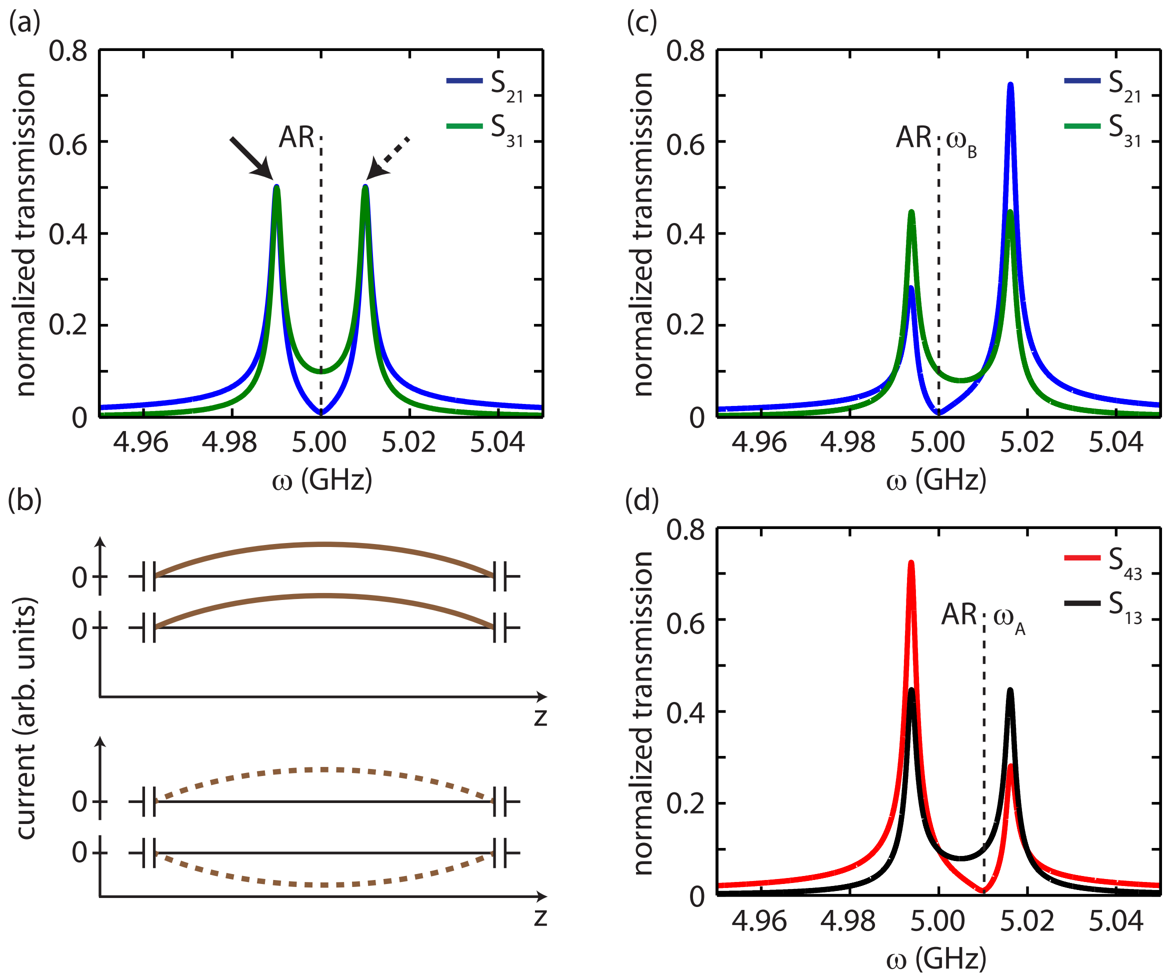

Figure 1.6: Theoretical transmission spectra through two coupled resonators. The S-parameter nomenclature follows the definition shown in Fig. 1.5. (a) Identical resonators with $\omega_\mathrm{A} = \omega_\mathrm{B} = 5\,\mathrm{GHz}$ and $\kappa_\mathrm{A} = \kappa_\mathrm{B} = 1\,\mathrm{MHz}$. Two transmission maxima can be identified. They correspond to in-phase (solid arrow) and out-of-phase (dashed arrow) oscillating currents in the resonators. The antiresonance (AR) is located in the center between the two peaks. (b) Current distribution for the parallel (top) and antiparallel (bottom) first harmonic modes. (c) Theoretical S_{21} and S_{31} transmission spectra for two resonators with unequal resonant frequency ($\omega_\mathrm{A} = 5.01\,\mathrm{GHz}$, $\omega_\mathrm{B} = 5\,\mathrm{GHz}$, $\kappa_\mathrm{A} = \kappa_\mathrm{B} = 1\,\mathrm{MHz}$). The antiresonance allows for a precise determination of ω_B. (d) Same as (c) for S_{43} and S_{13}. The antiresonance occurs at ω_A.

the flux qubit potential, the third energy level is far detuned and not relevant in most experiments.

1.3.1 Josephson effect

The Josephson effect describes the tunneling of Cooper pairs through a thin insulating barrier separating two superconductors. It was postulated in 1962 by Brian D. Josephson [85] and demonstrated experimentally one year later by J. M. Rowell *et al* [86]. For a detailed description of the Josephson effect, we refer to Refs. [61, 87, 88].

A Josephson junction of the SIS-type[3] is depicted in Fig. 1.7. The macroscopic wave function describing the Cooper pair condensate in both superconductors separated by the insulating barrier is given by $\Psi_{1,2} = \sqrt{n_{1,2}} e^{\imath\phi_{1,2}}$, cf. Eq. (1.1). If the barrier is thin, the two wave functions overlap. Similar to the hydrogen atom, where the coupling energy arises from the overlap of the electronic wave functions of the constituting atoms, the Josephson junction can also be regarded as a molecule with the corresponding coupling energy $E_{\mathrm{J}} = E_{\mathrm{J0}}(1 - \cos\varphi)$, where $E_{\mathrm{J0}} = I_{\mathrm{c}}\Phi_0/2\pi$ [89]. Here, the critical Josephson current I_{c} is the maximum supercurrent that can flow through the barrier and $\Phi_0 = h/2e$ is the flux quantum with Planck's constant h and the Cooper pair electric charge $-2e$.

The supercurrent I_{s} through the barrier is described by the first Josephson equation, also known as the current-phase-relation,

$$I_{\mathrm{s}} = I_{\mathrm{c}} \sin\varphi \tag{1.46}$$

where, in the absence of a magnetic vector potential, the phase difference φ is defined by $\varphi = \phi_2 - \phi_1$.

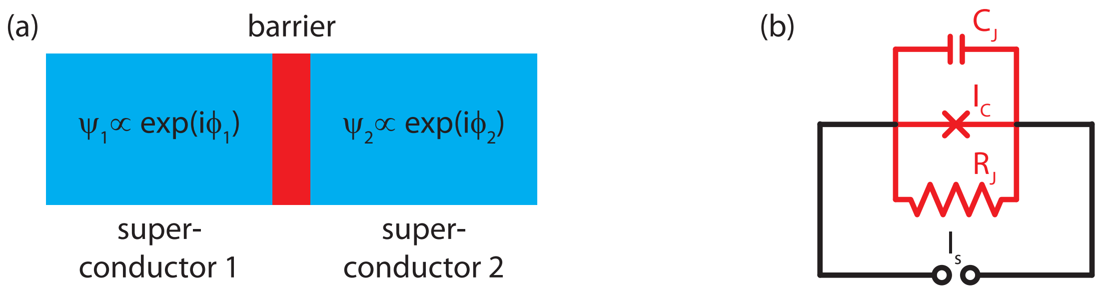

Figure 1.7: (a) Sketch of an SIS-type Josephson junction. Two superconductors with corresponding wave functions $\Psi_{1,2}$ are separated by a thin insulating barrier. (b) Equivalent circuit of a Josephson junction. In the RCSJ-model, a real Josephson junction is modeled as an ideal junction shunted by a resistance R_{J} and a capacitance C_{J}.

The second Josephson equation, also known as the voltage-phase-relation reads

$$\frac{\partial\varphi}{\partial t} = \frac{2\pi}{\Phi_0} V \tag{1.47}$$

where V denotes the voltage drop across the Josephson junction [61]. We note that this relation is used to define the Volt since 1990 [90].

The most important property of a Josephson junction for applications in circuit quan-

[3] superconductor-insulator-superconductor

tum electrodynamics is that it behaves as a nonlinear inductance. Considering the time derivative of the first Josephson equation (1.46) yields

$$\frac{dI_\mathrm{s}}{dt} = I_\mathrm{c} \cos\varphi \frac{d\varphi}{dt}. \tag{1.48}$$

With the second Josephson equation, one arrives at

$$\frac{dI_\mathrm{s}}{dt} = I_\mathrm{c} \cos\varphi \frac{2\pi}{\Phi_0} V. \tag{1.49}$$

Comparing this to the law of induction, $V = L\dot{I}$, the Josephson inductance is defined as

$$L_\mathrm{J} = \frac{\Phi_0}{2\pi I_\mathrm{c} \cos\varphi}. \tag{1.50}$$

A real Josephson junction can be modeled by an equivalent circuit as depicted in Fig. 1.7(b). In this resistively and capacitively shunted junction (RCSJ) model, the (in general voltage dependent) resistance R_J in parallel to the ideal Josephson junction accounts for quasiparticle tunneling. The resemblance of a Josephson junction to a plate capacitor is taken into account by a shunt capacitance C_J. Kirchhoff's law provides a classical equation of motion for the phase difference φ [91],

$$\frac{\Phi_0}{2\pi} C_\mathrm{J} \ddot{\varphi} + \frac{\Phi_0}{2\pi} \frac{1}{R_\mathrm{J}} \dot{\varphi} = I_\mathrm{s} - I_\mathrm{c} \sin\varphi. \tag{1.51}$$

Multiplying both sides of Eq. (1.51) with $(\Phi_0/2\pi)$, the result can be interpreted as the classical equation of motion of a 'phase particle' with mass M and damping ς in the so-called tilted washboard potential $U(\varphi)$, where

$$M = \left(\frac{\Phi_0}{2\pi}\right)^2 C_\mathrm{J}, \tag{1.52}$$

$$\varsigma = \left(\frac{\Phi_0}{2\pi}\right)^2 \frac{1}{R_\mathrm{J}} \quad \text{and} \tag{1.53}$$

$$U(\varphi) = E_\mathrm{J0}(1 - \cos\varphi - \frac{I_\mathrm{s}}{I_\mathrm{c}}\varphi). \tag{1.54}$$

The junction parameters are related by the Steward-McCumber-parameter [92, 93]

$$\beta_\mathrm{c} = \frac{2\pi}{\Phi_0} I_\mathrm{c} R_\mathrm{J}^2 C_\mathrm{J}. \tag{1.55}$$

Josephson junctions with $\beta_\mathrm{c} > 1$ are referred to as underdamped and their current-voltage characteristic shows a hysteric behaviour. Conversely, overdamped contacts with $\beta_\mathrm{c} < 1$

do not show a hysteric current-voltage characteristic [90].

1.3.2 Quantum mechanical description of a Josephson junction

Thus far, we have treated the Josephson junction as a classical system where both the phase difference φ and its time derivative $\dot{\varphi}$, which is proportional to the charge $Q = C_J V = \frac{\hbar}{2e} C_J \dot{\varphi}$, have been treated as purely classical variables. In this section, we discuss the limits of the classical description following Ref. [89].

To this end, we consider a strongly underdamped junction, i.e. $\beta_c \gg 1$, with capacitance C_J. The energy of the electric field is given by

$$K = \frac{Q^2}{2C_J} = \frac{1}{2} C_J \left(\frac{\hbar}{2e}\right) \dot{\varphi}^2, \tag{1.56}$$

which corresponds to the energy related to an extra charge Q on one of the junction electrodes relative to the other due to the finite voltage V. Together with the potential energy, the total energy of the junction is then given by

$$E_{J,tot} = E_{J0} \left(1 - \cos\varphi + \frac{1}{2}\left(\frac{\hbar C_J}{2eI_c}\right)^2 \dot{\varphi}^2\right). \tag{1.57}$$

For a quantum mechanical description of the Josephson junction, we consider this equation as the Hamiltonian of the junction and identify the corresponding kinetic energy with the electric field energy K. Together with the mass analogue of Eq. (1.52), we find that the momentum corresponds to the quantity $\frac{\hbar}{2e} Q$. This allows us to promote the classical variables Q and φ to quantum mechanical operators

$$Q \to \hat{Q} = -\imath 2e \frac{\partial}{\partial \varphi}, \tag{1.58}$$

$$\varphi \to \hat{\varphi}. \tag{1.59}$$

As a consequence, the Hamiltonian of a Josephson junction can be written as

$$\hat{H}_{JJ} = \frac{\hat{Q}^2}{2C_J} + E_{J0}(1 - \cos\hat{\varphi}) = -E_C \frac{\partial^2}{\partial \hat{\varphi}^2} + E_{J0}(1 - \cos\hat{\varphi}), \tag{1.60}$$

where $E_C = (2e)^2/2C_J$ is the charging energy of the junction for a single Cooper pair. The commutation relation for the operators reads

$$[\hat{\varphi}, \hat{Q}] = \imath 2e \tag{1.61}$$

and the uncertainty relation for the number of Cooper pairs $N = Q/2e$ and the phase is given by

$$\Delta N \times \Delta\varphi \geq 1. \tag{1.62}$$

1.3.3 Flux quantization

Postulated by London in 1950 [94] and demonstrated experimentally by Doll and Näbauer [95] and Deaver and Fairbank [96], flux quantization is a direct proof of the macroscopic quantum nature of superconductivity. We consider a superconducting ring, cf. Fig.1.8, where the Cooper pair condensate is described by a macroscopic wave function, cf. Eq. (1.1)

$$\Psi(\mathbf{r},t) = \Psi_0(\mathbf{r},t)\mathrm{e}^{\imath\phi(\mathbf{r},t)}. \tag{1.63}$$

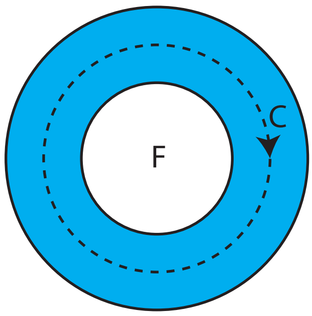

Figure 1.8: Superconducting ring (blue) with an integration path C enclosing the area F.

For the superconducting circulating current in the ring shown in Fig. 1.8, a stationary solution is only expected if the macroscopic wave function interferes constructively along the circumference of the ring. Integrating the supercurrent density $\mathbf{J}_\mathrm{s}$, cf. Eq. (1.2), along a closed path C yields [61, 90]

$$\oint_C (\Lambda \mathbf{J}_\mathrm{s}) \cdot d\mathbf{l} + \int_F \mathbf{b} \cdot d\mathbf{F} = n\Phi_0 \tag{1.64}$$

where $\mathbf{b} = \mathrm{rot}\mathbf{A}$ is the magnetic flux density and F is the area enclosed by the closed path C. The left hand side of Eq. (1.64) is called the fluxoid which is an integer multiple of the flux quantum Φ_0. If the path C is located deep inside the superconductor such that the supercurrent density is zero, Eq. (1.64) simplifies to the flux quantisation

$$\int_F \mathbf{b} \cdot d\mathbf{F} = n\Phi_0. \tag{1.65}$$

1.3.4 Flux qubit potential

A persistent current flux qubit consists of a superconducting loop intersected by three Josephson junctions as shown in Fig. 1.9. Two of them are designed to the same critical current I_c while the critical current of the third junction, referred to as the α-junction, is designed to αI_c. Typical values for α range from 0.5 to 0.8 and typical junction areas are $0.02\,\mu\mathrm{m}^2$ - $0.04\,\mu\mathrm{m}^2$[52]. The flux qubit potential can be written as the sum of the

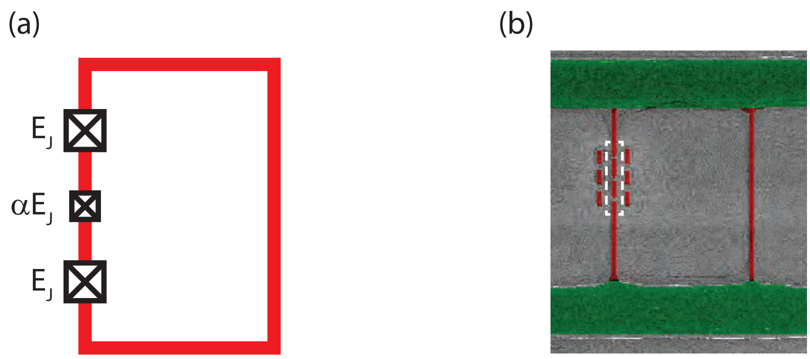

Figure 1.9: (a) Sketch of a three Josephson junction flux qubit. The superconducting ring (red loop) is intersected by three Josephson junctions where two of them are of equal size and the size of the third junction is reduced by a factor α. (b) Flux qubit fabricated in Al-technology on a silicon substrate coupled galvanically to the signal lines of two coplanar stripline resonators (green stripes). The position of the three Josephson junctions is highlighted by the white dashed rectangle. Sample image by courtesy of E. Hoffmann [97].

potential energies of the three juncions [16],

$$U_{\mathrm{Q}} = E_{\mathrm{J0}}[(1-\cos\varphi_1) + (1-\cos\varphi_2) + \alpha(1-\cos\varphi_3)] \tag{1.66}$$

where $\varphi_{1,2}$ denote the phase differences of the identical Josephson junctions and φ_3 is the phase difference of the α-junction. The phase difference φ_3 in Eq. (1.66) can be eliminated using fluxoid quantisation. If the geometric inductance of the qubit loop is small compared to the Josephson inductance, the flux qubit potential rewrites to[4]

$$U_{\mathrm{Q}} = E_{\mathrm{J0}}[2 + \alpha - \cos\varphi_1 - \cos\varphi_2 - \alpha\cos(2\pi f + \varphi_1 - \varphi_2)], \tag{1.67}$$

where $f = \Phi_{\mathrm{ext}}/\Phi_0$ is the frustration and Φ_{ext} is the magnetic flux threading the qubit loop. The flux qubit potential of Eq. (1.67) is shown in Fig. 1.10 for $\alpha = 0.7$ and $\Phi_{\mathrm{ext}} = \Phi_0/2$. The potential is 2π-periodic in both φ_1 and φ_2 which allows us to define unit cells by

[4] We use the sign convention of Ref. [16].

connecting neighbouring potential maxima. Within each unit cell, we find two potential minima which we identify with counterclockwise and clockwise persistent currents in the qubit loop. As can be seen from Fig. 1.10(b) and Fig. 1.10(c), the potential barrier between two adjacent minima within one unit cell is significantly lower than the potential barrier between adjacent minima in different unit cells.

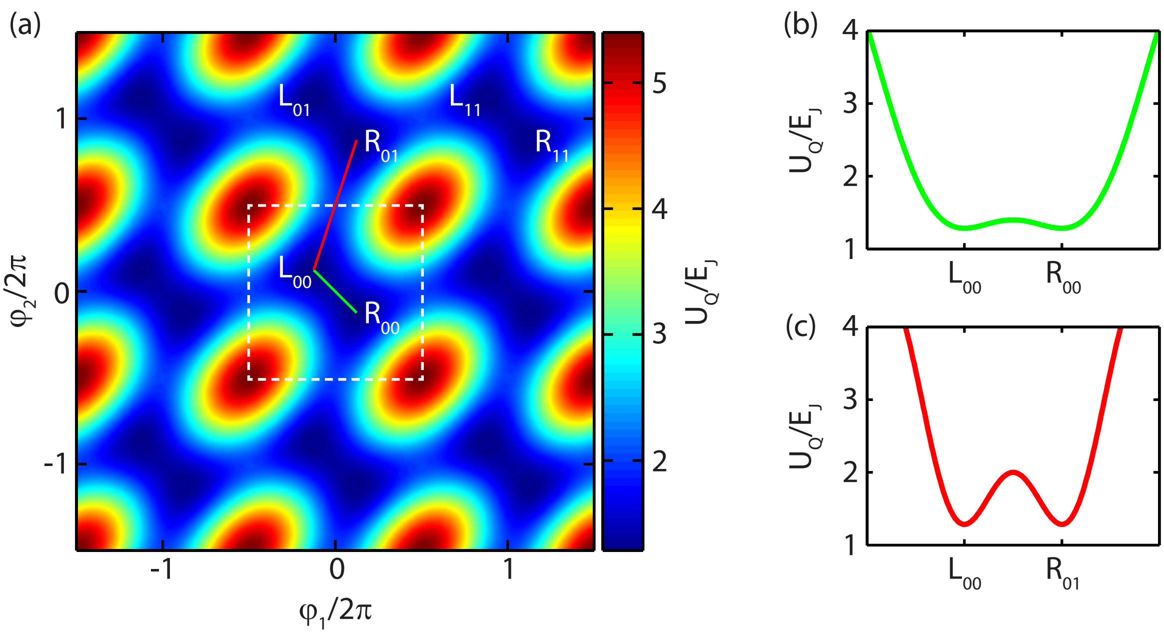

Figure 1.10: (a) Potential landscape of a three-Josephson flux qubit for $\alpha = 0.7$ and $f = 0.5$. A unit cell is defined by the white dashed square. In each unit cell, two minima, denoted by L and R, can be identified corresponding to counterclockwise and clockwise persistent currents in the qubit loop. (b) Cut through the qubit potential along the line connecting two minima within one unit cell. A double well potential can be observed. (c) Same as (b), cut along a line connecting two minima in adjacent unit cells. The potential barrier is significantly larger as compared to the one shown in (b).

1.3.5 Flux qubit as a quantum system

Following Eq. (1.60), we can write the full Hamiltonian of the three Josephson junction flux qubit as [98]

$$\hat{H}_{\mathrm{Q,full}} = \frac{1}{2}\left(\frac{\hat{Q}_1^2}{2C_{\mathrm{J}}} + \frac{\hat{Q}_2^2}{2C_{\mathrm{J}}(1+2\alpha)}\right) + E_{\mathrm{J0}}[2+\alpha-\cos\hat{\varphi}_1-\cos\hat{\varphi}_2-\alpha\cos(2\pi f+\hat{\varphi}_1-\hat{\varphi}_2)] \tag{1.68}$$

in which $\hat{Q}_{1,2}$ are the charge operators of the junctions corresponding to the phase operators $\hat{\varphi}_{1,2}$ and C_{J} is the capacitance of a regular junction.

Close to a degeneracy point, where $f = n + \frac{1}{2}$, $n \in \mathbb{Z}$, the flux qubit can be described quantum mechanically by a general two-level Hamiltonian

$$\hat{H}_{\mathrm{Q}} = \frac{\epsilon}{2}\hat{\sigma}_z + \frac{\Delta}{2}\hat{\sigma}_x = \frac{1}{2}\begin{pmatrix} \epsilon & \Delta \\ \Delta & -\epsilon \end{pmatrix}, \tag{1.69}$$

where $\hat{\sigma}_z$ and $\hat{\sigma}_x$ denote Pauli operators. The eigenstates of $(\epsilon/2)\hat{\sigma}_z$ correspond to the counterclockwise and clockwise persistent currents mentioned above. We assign to them the states $|+I_{\mathrm{p}}\rangle$ and $|-I_{\mathrm{p}}\rangle$. They are coupled via the energy term Δ proportional to the tunneling matrix element of the potential barrier shown in Fig. 1.10. Due to the lower barrier height, the dominant coupling mechanism between the states $|+I_{\mathrm{p}}\rangle$ and $|-I_{\mathrm{p}}\rangle$ is tunneling through the potential barrier between two minima within one unit cell referred to as intracell tunneling. For $\varphi_1 = -\varphi_2$, the qubit potential of Eq. (1.67) simplifies to a double well potential. While Δ is independent of the magnetic flux threading the qubit loop, the energy bias ϵ is given by

$$\epsilon(\Phi_{\mathrm{ext}}) = 2\left.\frac{\partial U_{\mathrm{Q}}}{\partial \Phi_{\mathrm{ext}}}\right|_{\varphi_1=-\varphi_2} \delta\Phi_{\mathrm{ext}} = 2I_{\mathrm{p}}\delta\Phi_{\mathrm{ext}}, \tag{1.70}$$

where $\delta\Phi_{\mathrm{ext}} = [\Phi_{\mathrm{ext}} - \Phi_0/2](\mathrm{mod}\,\Phi_0)$. For the minima of the double-well potential, we find $\varphi_1 = -\varphi_2 = \pm\,\arccos(1/2\alpha)$, yielding an expression for the persistent current

$$I_{\mathrm{p}} = I_{\mathrm{c}}\sqrt{1-(1/2\alpha)^2}. \tag{1.71}$$

The energy level diagram of the Hamiltonian of Eq. (1.69) is shown in Fig. 1.11(a). At the degeneracy point $\delta\Phi_{\mathrm{ext}} = 0$, the classically degenerate energy levels are split by the tunnel coupling Δ. The qubit ground and excited states are given by an antisymmetric and symmetric superposition of $|+I_{\mathrm{p}}\rangle$ and $|-I_{\mathrm{p}}\rangle$, respectively. The qubit transition energy between ground and excited state depends on the external magnetic flux and is given by

$$\hbar\omega_{\mathrm{Q}} = \sqrt{\Delta^2 + \epsilon(\Phi_{\mathrm{ext}})^2}. \tag{1.72}$$

Figure 1.11(b) shows the classical expectation values of the qubit persistent current $I_{\mathrm{p}}\langle\hat{\sigma}_z\rangle = \partial U_{\mathrm{Q}}/\partial\Phi_{\mathrm{ext}}$ of the qubit ground and excited state. As can be seen, the expectation value of the persistent current is zero at the degeneracy point.

1.3.6 Coherence

In all practical applications, it is impossible to isolate a qubit from the environment. Interaction with e.g. a thermal bath or other uncontrolled external or internal degrees

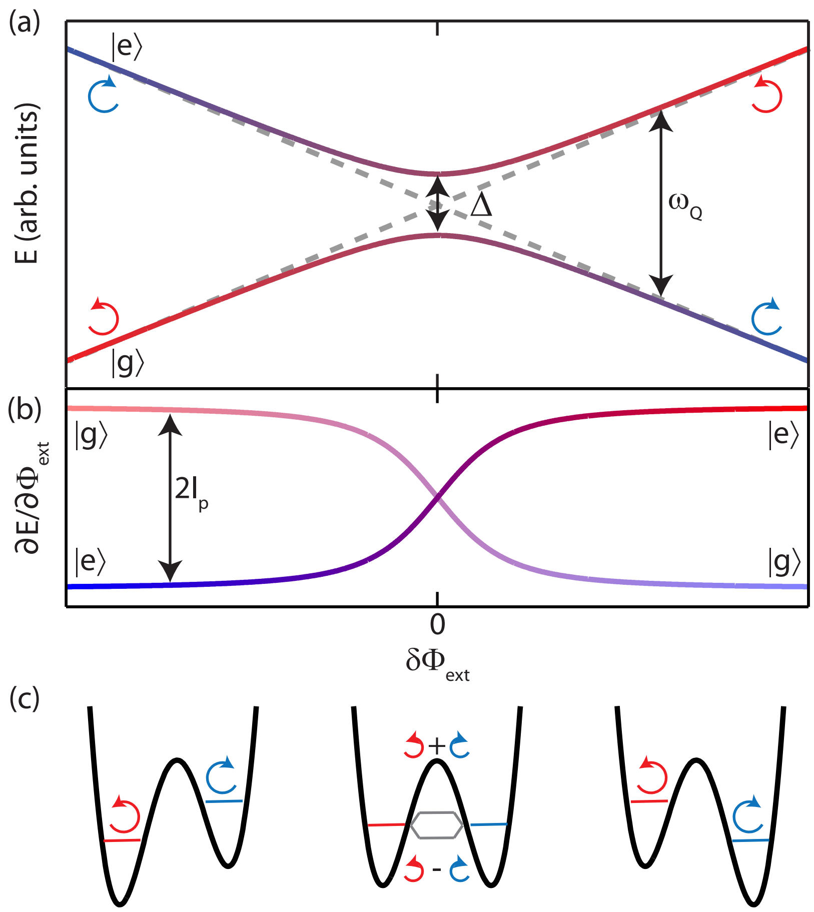

Figure 1.11: (a) Eigenenergies of the flux qubit Hamiltonian of Eq. (1.69) as a function of the frustration. Depending on the external magnetic flux, the ground state corresponds to a counterclockwise or clockwise persistent current. Around the degeneracy point $\delta\Phi_{\rm ext} = 0$, the energy degeneracy is lifted by the tunnel coupling Δ. Dashed grey lines: Eigenenergies for the classical case $\Delta = 0$. (b) Expectation value of the circulating currents for ground and excited state as a function of the frustration. The circulating current associated with the excited state is drawn with reduced opacity. (c) Double-well potential along the line connecting intracell minima, cf. Fig. 1.10, for three different frustration values. The double well potential in the center corresponds to $\delta\Phi_{\rm ext} = 0$, where ground and excited state are given by antisymmetric and symmetric superpositions of counterclockwise and clockwise persistent currents.

of freedom will lead to a loss of quantum information, a process subsumed under the term *decoherence* [99, 100]. Following Bloch-Redfield theory [101, 102], decoherence of a quantum two-level system is described in terms of two characteristic rates. The first one is the so-called longitudinal relaxation rate $\Gamma_1 = T_1^{-1}$ describing the relaxation of the excited qubit state to the ground state. The rate Γ_1 can be measured directly by means of Rabi measurements, cf. Sec. 2.2 and Sec. 3.3. The loss of phase coherence within a qubit state is described by the pure dephasing rate $\Gamma_\varphi = T_\varphi^{-1}$ [99]. In contrast to the longitudinal relaxation rate, it cannot be measured directly. Instead, the transverse relaxation rate

$$T_2^{-1} = \Gamma_2 = \frac{1}{2}\Gamma_1 + \Gamma_\varphi \tag{1.73}$$

has to be extracted from Ramsey and spin echo measurements [17, 103]. For flux qubits, the highest reported coherence times are $T_1 = 12\,\mu\text{s}$ and $T_\varphi > 100\,\mu\text{s}$ [104, 105]. Significantly longer coherence times of some $10\,\mu\text{s}$ can be reached with transmon qubits in 3D microwave cavities [106].

1.4 Circuit quantum electrodynamics

Coupling a quantum mechanical two-level system such as a flux qubit to a quantum mechanical harmonic oscillator such as a transmission line resonator constitutes the prototypical setup of the circuit quantum electrodynamics (QED) [5] architecture. This scenario represents the circuit equivalent of the prototypical setup of cavity QED where a natural atom interacts with the light field confined in a three-dimensional optical cavity. The correspondence between cavity and circuit QED is depicted in Fig. 1.12.
In order to use circuit QED as a platform for the study of light-matter interaction or quantum information and simulation protocols, the regime of strong coupling, where the coupling strength between the light field and the two-level system has to be much larger than the qubit and cavity decay rates, has to reached. This goal is hard to achieve with natural atoms and three-dimensional cavity resonators in the field of cavity QED [107, 108]. However, in the field of circuit QED, the large dipole moments of superconducting qubits and the small mode volumes of the quasi-one-dimensional transmission line resonators lead to coupling strengths exceeding the ones observed in cavity QED by several orders of magnitude, making the limit of strong coupling easily attainable.
In this section, we provide the quantum mechanical treatment of the interaction between a flux qubit and a transmission line resonator.

1.4.1 Rabi model

We consider a flux qubit with the Hamiltonian of Eq. (1.69) and a single resonant mode described by the Hamiltonian of Eq. (1.24) coupled via dipolar interaction [109]. The corresponding Hamiltonian is given by

$$\begin{aligned}\hat{\hat{H}} &= \hat{H}_\mathrm{Q} + \hat{H}_\mathrm{LC} + \hat{H}_\mathrm{int} = \\ &= \frac{\epsilon}{2}\hat{\sigma}_z + \frac{\Delta}{2}\hat{\sigma}_x + \hbar\omega_\mathrm{R}\left(\hat{a}^\dagger\hat{a} + \frac{1}{2}\right) + \hbar g\hat{\sigma}_z(\hat{a}^\dagger + \hat{a}).\end{aligned} \tag{1.74}$$

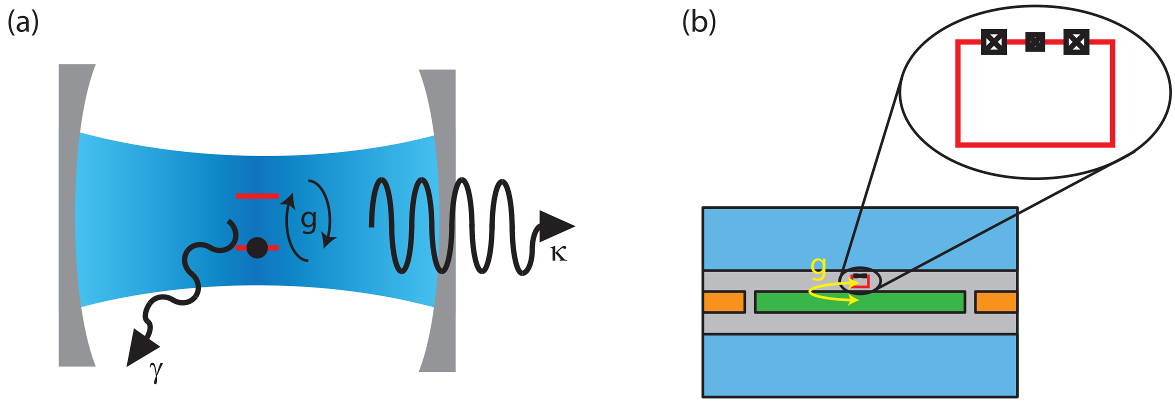

Figure 1.12: (a) Cavity QED architecture. A natural (two-level) atom interacts with the light field confined in a three-dimensional optical cavity. Photons are exchanged between light field and atom at the coupling rate g. Photons are lost from the cavity at rate κ and incoherent relaxation of the qubit occurs at rate γ. (b) Prototypical setup of the circuit QED architecture. A single artificial atom (here: a flux qubit) interacts with the microwave field inside a quasi-one-dimensional transmission line resonator.

For a flux qubit coupled to a transmission line resonator, the coupling is of inductive nature. The corresponding coupling energy is [110]

$$\hbar g = M I_{\mathrm{p}} I_{\mathrm{res}} \tag{1.75}$$

where M is the mutual inductance between resonator and qubit and I_{p} is the qubit persistent current, cf. Eq. (1.71). $I_{\mathrm{res}} = \sqrt{\hbar\omega_{\mathrm{R}}/2L_{\mathrm{R}}}$ is the rms value of the current flowing in the signal line of the resonator with resonant frequency ω_{R} and inductance L_{R}.

In what follows we drop the term $\hbar\omega_{\mathrm{R}}/2$ since it merely represents an energy offset. We rotate the Hamiltonian of Eq. (1.74) into the eigenbasis of the qubit by performing the transformations

$$\hat{\sigma}_z \to \cos\theta\hat{\sigma}_z - \sin\theta\hat{\sigma}_x \tag{1.76}$$
$$\hat{\sigma}_x \to \sin\theta\hat{\sigma}_z + \cos\theta\hat{\sigma}_x, \tag{1.77}$$

where we introduce the mixing angle $\theta = \arctan(\Delta/\epsilon)$ with $\sin\theta = \Delta/\hbar\omega_{\mathrm{Q}}$ and $\cos\theta = \epsilon/\hbar\omega_{\mathrm{Q}}$. With this transformation, the Hamiltonian of Eq. (1.74) reads

$$\hat{H} = \frac{\hbar\omega_{\mathrm{Q}}}{2}\hat{\sigma}_z + \hbar\omega_{\mathrm{R}}\hat{a}^\dagger\hat{a} + \hbar g(\hat{a}^\dagger + \hat{a})(\cos\theta\hat{\sigma}_z - \sin\theta\hat{\sigma}_x). \tag{1.78}$$

At the degeneracy point $\Phi_{\mathrm{ext}} = \Phi_0/2$, we find $\epsilon = 0$ and therefore $\cos\theta = 0$, simplifying the Hamiltonian of Eq. (1.78) to

$$\hat{H}_{\epsilon=0} = \frac{\hbar\omega_{\mathrm{Q}}}{2}\hat{\sigma}_z + \hbar\omega_{\mathrm{R}}\hat{a}^\dagger\hat{a} - \hbar g\sin\theta\hat{\sigma}_x(\hat{a}^\dagger + \hat{a}). \tag{1.79}$$

In analogy to the Rabi model [111] which describes the interaction of a natural atom and a classical light field, we refer to the Hamiltonian of Eq. (1.79) as a quantum Rabi model. Following Ref. [112], we refer to the more general Hamiltonian of Eq. (1.78) as a generalized Rabi model.

Defining the qubit state raising and lowering operators $\hat{\sigma}_\pm = (\hat{\sigma}_x \pm \imath\hat{\sigma}_y)/2$, the generalized Rabi Hamiltonian rewrites to

$$\hat{H} = \frac{\hbar\omega_{\mathrm{Q}}}{2}\hat{\sigma}_z + \hbar\omega_{\mathrm{R}}\hat{a}^\dagger\hat{a} + g\cos\theta(\hat{a}^\dagger + \hat{a})\hat{\sigma}_z - g\sin\theta(\hat{a}^\dagger\hat{\sigma}_+ + \hat{a}\hat{\sigma}_- + \hat{a}^\dagger\hat{\sigma}_- + \hat{a}\hat{\sigma}_+). \tag{1.80}$$

1.4.2 Jaynes-Cummings model

In 1963, E. T. Jaynes and F. W. Cummings presented a theoretical study of the interaction between an atom and a quantized mode of a radiation field [113]. Because of its importance, it is sometimes referred to as the standard model of quantum optics [80, 114]. Below, we derive the Jaynes-Cummings model by transforming the Hamiltonian of Eq. (1.80) into the interaction picture following Ref. [115]. To this end, we split the Hamiltonian into two parts,

$$\hat{H}_0 = \frac{\hbar\omega_{\mathrm{Q}}}{2}\hat{\sigma}_z + \hbar\omega_{\mathrm{R}}\hat{a}^\dagger\hat{a} \tag{1.81}$$

$$\hat{H}_1 = g\cos\theta(\hat{a}^\dagger + \hat{a})\hat{\sigma}_z - g\sin\theta(\hat{a}^\dagger\hat{\sigma}_+ + \hat{a}\hat{\sigma}_- + \hat{a}^\dagger\hat{\sigma}_- + \hat{a}\hat{\sigma}_+). \tag{1.82}$$

The transformation into the interaction picture is performed by calculating

$$\hat{H}_{\mathrm{int}} = \mathrm{e}^{\imath\hat{H}_0 t/\hbar}\hat{H}_1\mathrm{e}^{-\imath\hat{H}_0 t/\hbar}. \tag{1.83}$$

Using the Baker-Campbell-Hausdorff formula [116], we find that the annihilation and creation operators and the Pauli operators are transformed to

$$\hat{a} \to \hat{a}\mathrm{e}^{-\imath\omega_{\mathrm{R}}t}, \tag{1.84}$$

$$\hat{a}^\dagger \to \hat{a}^\dagger\mathrm{e}^{\imath\omega_{\mathrm{R}}t}, \tag{1.85}$$

$$\hat{\sigma}_- \to \hat{\sigma}_-\mathrm{e}^{-\imath\omega_{\mathrm{Q}}t}, \tag{1.86}$$

$$\hat{\sigma}_+ \to \hat{\sigma}_+\mathrm{e}^{\imath\omega_{\mathrm{Q}}t}, \tag{1.87}$$

$$\hat{\sigma}_z \to \hat{\sigma}_z. \tag{1.88}$$

Applying these transformations to the Hamiltonian of Eq. (1.80) yields

$$\begin{aligned}\hat{H}_{\text{int}} &= g\cos\theta(\hat{a}^\dagger \mathrm{e}^{\omega_\mathrm{R}t} + \hat{a}\mathrm{e}^{-\omega_\mathrm{R}t})\hat{\sigma}_z + \\ &- g\sin\theta(\hat{a}^\dagger\hat{\sigma}_+\mathrm{e}^{\imath(\omega_\mathrm{R}+\omega_\mathrm{Q})t} + \hat{a}\hat{\sigma}_-\mathrm{e}^{-\imath(\omega_\mathrm{R}+\omega_\mathrm{Q})t} + \hat{a}^\dagger\hat{\sigma}_-\mathrm{e}^{\imath(\omega_\mathrm{R}-\omega_\mathrm{Q})t} + \hat{a}\hat{\sigma}_+\mathrm{e}^{-\imath(\omega_\mathrm{R}-\omega_\mathrm{Q})t}).\end{aligned} \tag{1.89}$$

In circuit (and also cavity) QED, the resonator mode frequency ω_R is typically on the same order of magnitude as the qubit (atom) transition frequency ω_Q such that $|\omega_\mathrm{R} - \omega_\mathrm{Q}| \ll \omega_\mathrm{R}, (\omega_\mathrm{R} + \omega_\mathrm{Q})$. This allows to identify fast and slowly rotating terms in the interaction Hamiltonian of Eq. (1.89). If in addition the coupling strength g, which defines the timescale of the slowly rotating terms [117], is small enough to fulfill $g \ll \omega_\mathrm{R}, (\omega_\mathrm{R} + \omega_\mathrm{Q})$, we can perform a rotating wave approximation, reducing the above interaction Hamiltonian to

$$\hat{H}_{\text{int,RW}} = -g\sin\theta(\hat{a}^\dagger\hat{\sigma}_-\mathrm{e}^{\imath(\omega_\mathrm{R}-\omega_\mathrm{Q})t} + \hat{a}\hat{\sigma}_+\mathrm{e}^{-\imath(\omega_\mathrm{R}-\omega_\mathrm{Q})t}). \tag{1.90}$$

By rotating the Hamiltonian back into the Schrödinger picture and reintroducing the energy offset $\hbar\omega_\mathrm{R}/2$ we arrive at the Jaynes-Cummings Hamiltonian,

$$\hat{H}_{\text{JC}} = \frac{\hbar\omega_\mathrm{Q}}{2}\hat{\sigma}_z + \hbar\omega_\mathrm{R}\left(\hat{a}^\dagger\hat{a} + \frac{1}{2}\right) - g\sin\theta(\hat{a}^\dagger\hat{\sigma}_- + \hat{a}\hat{\sigma}_+). \tag{1.91}$$

One notable property of the Jaynes-Cummings-Hamiltonian is that it commutes with the operator of the total number of excitations, $M = \hat{a}^\dagger\hat{a} + \hat{\sigma}_+\hat{\sigma}_-$. As a consequence, the total number of excitations is conserved.

Next, we discuss the eigenstates of the Jaynes-Cummings-Hamiltonian. We write the eigenstates of an uncoupled qubit-resonator system, i.e. $g = 0$, as $|q,n\rangle$ where $q = \{g,e\}$ denotes the qubit ground and excited state, respectively, and $n \in \mathbb{N}$ denotes the photon occupation of the resonator. We note that the eigenstates of the Jaynes-Cummings-Hamiltonian are not pure resonator or qubit eigenstates, but superpositions of resonator and qubit states. The ground state is given by $|g,0\rangle$ and the excited states, referred to as dressed states, by [1]

$$|-,n\rangle = \cos\Theta|g,n\rangle - \sin\Theta|e,n-1\rangle, \tag{1.92}$$

$$|+,n\rangle = \sin\Theta|g,n\rangle + \cos\Theta|e,n-1\rangle. \tag{1.93}$$

The photon number dependent mixing angle is defined by $2\Theta = \arctan(2g\sqrt{n}/\delta)$ with the qubit-resonator detuning $\delta = \omega_\mathrm{Q} - \omega_\mathrm{R}$. The corresponding eigenenergies are given by

$$E_{\pm,n} = n\hbar\omega_\mathrm{R} \pm \frac{\hbar}{2}\sqrt{4g^2\sin^2\theta + \delta^2}. \tag{1.94}$$

1.4.2.1 The resonant regime

In the resonant regime, the qubit transition frequency matches the resonator frequency, i.e. the detuning $\delta = 0$, yielding $\sin\Theta = \cos\Theta = 1/\sqrt{2}$. In this situation, the eigenstates of the Jaynes-Cummings-Hamiltonian reduce to

$$|\pm, n\rangle = \frac{|g,n\rangle \pm |e,n-1\rangle}{\sqrt{2}}. \tag{1.95}$$

From Fig. 1.13(a) it can be seen that degeneracy of the states with equal total numbers of excitations is lifted and a photon number dependent energy splitting of $2g\sqrt{n}$ is formed. We note that the states of Eq. (1.95) represent maximally entangled qubit-resonator states [1]. An initial state $|e,0\rangle$, where the qubit is excited and zero photons are stored in the resonator, will flop into the state $|g,1\rangle$ and back at the vacuum Rabi frequency g/π.

1.4.2.2 The dispersive regime

Next, we discuss the regime where the qubit is far detuned from the resonator, i.e. $\delta \gg g\sin\theta$. Insight into this regime is gained by performing the unitary transformation

$$\hat{\mathcal{U}} = \exp\left[\frac{g}{\delta}(\hat{a}\hat{\sigma}_+ - \hat{a}^\dagger\hat{\sigma}_-)\right] \tag{1.96}$$

on the Jaynes-Cummings Hamiltonian of Eq. (1.91). Expanding $\hat{\mathcal{U}}\hat{H}_{\mathrm{JC}}\hat{\mathcal{U}}^\dagger$ to second order in g yields

$$\hat{H}_{\mathrm{JC}}^{\mathrm{disp}} = \hat{\mathcal{U}}\hat{H}_{\mathrm{JC}}\hat{\mathcal{U}}^\dagger \approx \hbar\left(\omega_{\mathrm{R}} + \frac{g^2\sin^2\theta}{\delta}\hat{\sigma}_z\right)\left(\hat{a}^\dagger\hat{a} + \frac{1}{2}\right) + \frac{\hbar}{2}\omega_{\mathrm{Q}}\hat{\sigma}_z. \tag{1.97}$$

The resulting Hamiltonian resembles the Jaynes-Cummings Hamiltonian of Eq. (1.91), however, the resonator frequency is shifted to

$$\tilde{\omega}_{\mathrm{R}} = \omega_{\mathrm{R}} \pm \frac{g^2\sin^2\theta}{\delta}\langle\hat{\sigma}_z\rangle. \tag{1.98}$$

We note that this qubit-state dependent shift can be utilized to read out the qubit state without destroying it [118]. The effective Hamiltonian of Eq. (1.97) can be rearranged to

$$\hat{H}_{\mathrm{JC}}^{\mathrm{disp}} \approx \hbar\omega_{\mathrm{R}}\left(\hat{a}^\dagger\hat{a} + \frac{1}{2}\right) + \frac{\hbar}{2}\left[\omega_{\mathrm{Q}} + \frac{2g^2\sin^2\theta}{\delta}\hat{a}^\dagger\hat{a} + \frac{g^2\sin^2\theta}{\delta}\right]\hat{\sigma}_z. \tag{1.99}$$

As can be seen, two shifts are imposed on the bare qubit frequency ω_{Q}. The ac Zeeman shift $(2g^2\sin^2\theta/\delta)\hat{a}^\dagger\hat{a}$ is proportional to the photon number in the resonator. We will see in Sec. 2.1.4 how this effect can be used to calibrate the photon number in the resonator.

The Lamb shift $g^2 \sin^2\theta/\delta$ is independent of the photon number and thus represents an energy offset which is not accessible experimentally. The energy level diagram of the Jaynes-Cummings Hamiltonian in the dispersive regime is shown in Fig. 1.13(b).

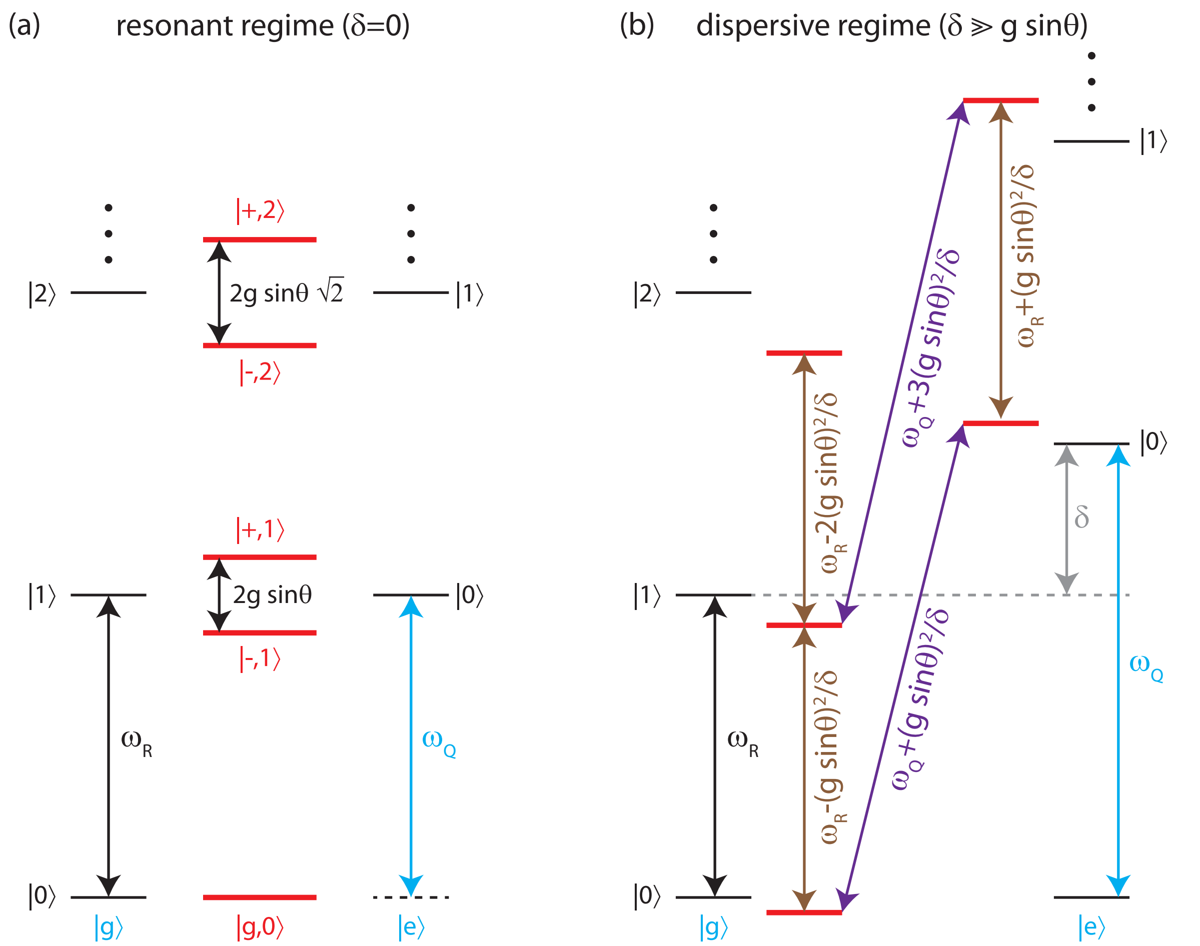

Figure 1.13: Schematic energy level diagram of the Jaynes-Cummings Hamiltonian. Black lines: Eigenenergies of the uncoupled system for the qubit in the ground state (left side) and excited state (right side), respectively. Red lines: Eigenenergies of the coupled system. The number of photons n in the resonator is denoted by $|n\rangle$. (a) Resonant regime. The splitting of the energy levels is given by $2g\sin\theta\times\sqrt{n}$. (b) Dispersive regime. The resonator mode frequency is shifted by $\overset{(+)}{-}(g\sin\theta)^2$ (brown arrows) for the qubit in the ground (excited) state. The dressed qubit transition frequency is shifted to $\tilde{\omega_{\mathrm{Q}}} = \omega_{\mathrm{Q}} + (2n+1)(g\sin\theta)^2/\delta$ (purple arrows).

1.4.3 The multimode Rabi and Jaynes-Cummings model

The high flexibility of the circuit QED architecture allows to couple a quantum bit to multiple modes of a single resonator or even to multiple resonators. We therefore expand the Rabi Hamiltonian of Eq. (1.74) to multiple modes ω_n coupling to the qubit with the coupling strengths g_n. The multimode Rabi Hamiltonian reads

$$\begin{aligned}\hat{H} &= H_{\mathrm{Q}} + \sum_n \hat{H}_{\mathrm{LC},n} + \sum_n \hat{H}_{\mathrm{int},n} = \\ &= \frac{\epsilon}{2}\hat{\sigma}_z + \frac{\Delta}{2}\hat{\sigma}_x + \sum_n \left[\hbar\omega_n \left(\hat{a}_n^\dagger \hat{a}_n + \frac{1}{2}\right) + \hbar g_n \hat{\sigma}_z (\hat{a}_n^\dagger + \hat{a}_n)\right]. \end{aligned} \tag{1.100}$$

If the criteria for applying the Jaynes-Cummings model are fulfilled for all modes, i.e. $g \ll \omega_n, (\omega_n - \omega_{\mathrm{Q}})$ holds and $|\omega_n - \omega_{\mathrm{Q}}| \ll \omega_n, (\omega_n - \omega_{\mathrm{Q}})$ for all n, the multimode Rabi Hamiltonian can be approximated by the multimode Jaynes-Cummings Hamiltonian. In the qubit eigenbasis, it reads

$$\hat{H}_{\mathrm{JC}} = \frac{\hbar\omega_{\mathrm{Q}}}{2}\hat{\sigma}_z + \sum_n \left[\hbar\omega_n \left(\hat{a}_n^\dagger \hat{a}_n + \frac{1}{2}\right) - g_n \sin\theta (\hat{a}_n^\dagger \hat{\sigma}_- + \hat{a}_n \hat{\sigma}_+)\right]. \tag{1.101}$$

1.4.4 Ultrastrong coupling

Another notable feature of the circuit QED architecture is that the coupling strength between qubit and resonator can be engineered to the desired value within several orders of magnitude. Due to the small mode volumes of the quasi-one-dimensional transmission line resonators and the large dipole moments of the qubits, even the regime of ultrastrong coupling can be reached where the coupling strength reaches a significant fraction of the resonant frequency and the Jaynes-Cummings model breaks down [37–39]. Therefore, counterrotating terms of the form $\hat{a}^\dagger\hat{\sigma}_+$ and $\hat{a}\hat{\sigma}_-$, which have been neglected in the Jaynes-Cummings-Hamiltonian of Eq. (1.91), have to be taken into account. If we again consider coupling of the qubit to multiple modes, the ultrastrongly coupled qubit-resonator system has to be described by the multimode Rabi Hamiltonian of Eq. (1.100). The operator of the total number of excitations $M = \hat{a}^\dagger\hat{a} + \hat{\sigma}_+\hat{\sigma}_-$ does not commute with the Rabi Hamiltonian. As a consequence, the total number of excitations is no longer conserved which has been demonstrated experimentally in Ref. [37].

We consider a qubit coupled ultrastrongly to one or multiple resonant modes at frequency ω_n. In the dispersive regime, the Hamiltonian can again be expanded to second order in the coupling strength g_n [109], yielding a dispersive shift given by

$$2(g_n \sin\theta)^2 \left(\frac{1}{\omega_{\mathrm{Q}} - \omega_n} + \frac{1}{\omega_{\mathrm{Q}} + \omega_n}\right). \tag{1.102}$$

The second term is referred to as the Bloch-Siegert shift [119] and has been demonstrated experimentally in a circuit QED setup in Ref. [38].

1.5 Two-resonator circuit quantum electrodynamics

Even though the prototypical circuit QED architecture has already proven to give deep insight into the physics of light-matter interaction and fundamental quantum mechanics, the realization of complex quantum gates and quantum information and simulation protocols require more complex setups consisting of a multitude of quantum bits and resonators. To ensure the controlled transfer of quantum information between the individual circuit elements, the coupling between the latter needs to be tunable *in situ*.
In this section we present an architecture allowing for tunable and switchable coupling between two transmission line resonators.

1.5.1 The quantum switch

The quantum switch architecture is comprised of a flux quantum bit with energy gap Δ and flux-dependent energy bias ϵ coupled to two transmission line resonators A and B with resonant frequencies ω_A and ω_B. The corresponding qubit-resonator coupling strengths are denoted by g_A and g_B. In addition, the mutual coupling strength g_AB between the two resonators is taken into account. A possible setup is sketched in Fig. 1.14(a). The theoretical treatment of this architecture is presented below and follows mainly Refs. [120, 121]. The quantum switch Hamiltonian is a two-mode Rabi Hamiltonian extended by the resonator-resonator coupling and reads

$$\begin{aligned}\hat{H}_\mathrm{QS} =& \frac{\epsilon}{2}\hat{\sigma}_z + \frac{\Delta}{2}\hat{\sigma}_x + \hbar\omega_\mathrm{A}\left(\hat{a}^\dagger\hat{a} + \frac{1}{2}\right) + \hbar\omega_\mathrm{B}\left(\hat{b}^\dagger\hat{b} + \frac{1}{2}\right) + \\ &+ \hbar g_\mathrm{A}(\hat{a}^\dagger + \hat{a})\hat{\sigma}_z + \hbar g_\mathrm{B}(\hat{b}^\dagger + \hat{b})\hat{\sigma}_z + \\ &+ \hbar g_\mathrm{AB}(\hat{a}^\dagger + \hat{a})(\hat{b}^\dagger + \hat{b}).\end{aligned} \tag{1.103}$$

To demonstrate the relevant physical effects, we restrict ourselves to the simplified case of frequency degenerate resonators ($\omega_\mathrm{R} = \omega_\mathrm{A} = \omega_\mathrm{B}$) and equal qubit-resonator coupling strengths ($g = g_\mathrm{A} = g_\mathrm{B}$). Neglecting global energy offsets and rotating the qubit into its eigenbasis (cf. Eqs. (1.76) and (1.77)) yields

$$\begin{aligned}\hat{\hat{H}}_\mathrm{QS} =& \frac{\hbar\omega_\mathrm{Q}}{2}\hat{\sigma}_z + \hbar\omega_\mathrm{R}(\hat{a}^\dagger\hat{a} + \hat{b}^\dagger\hat{b}) + \\ &+ \hbar g\left(\cos\theta\hat{\sigma}_z - \sin\theta\hat{\sigma}_x\right)\left[\left(\hat{a}^\dagger + \hat{a}\right) + \left(\hat{b}^\dagger + \hat{b}\right)\right] \\ &+ \hbar g_\mathrm{AB}\left(\hat{a}^\dagger + \hat{a}\right)\left(\hat{b}^\dagger + \hat{b}\right)\end{aligned} \tag{1.104}$$

with the qubit transition frequency $\omega_\mathrm{Q} = \sqrt{\Delta^2 + \epsilon^2}$ and the mixing angle $\theta = \arctan(\Delta/\epsilon)$. The Hamiltonian in the interaction picture can be obtained by means of the unitary transformation

$$\hat{\mathcal{U}} = \exp(-\lambda_\delta \mathcal{D} - \lambda_\Sigma \mathcal{S} - \lambda_\Omega \mathcal{W}) \tag{1.105}$$

with the parameters

$$\lambda_\delta = \frac{g \sin\theta}{\delta}, \qquad \delta = \omega_{\mathrm{Q}} - \omega_{\mathrm{R}}, \tag{1.106}$$

$$\lambda_\Sigma = \frac{g \sin\theta}{\Sigma}, \qquad \Sigma = \omega_{\mathrm{Q}} + \omega_{\mathrm{R}}, \tag{1.107}$$

$$\lambda_\Omega = \frac{g \cos\theta}{\omega_{\mathrm{R}}} \tag{1.108}$$

and the operators

$$\hat{\mathcal{D}} = \hat{\sigma}_- \hat{a}^\dagger - \hat{\sigma}_+ \hat{a} + \hat{\sigma}_- \hat{b}^\dagger - \hat{\sigma}_+ \hat{b}, \tag{1.109}$$

$$\hat{\mathcal{S}} = \hat{\sigma}_- \hat{a} - \hat{\sigma}_+ \hat{a}^\dagger + \hat{\sigma}_- \hat{b} - \hat{\sigma}_+ \hat{b}^\dagger, \tag{1.110}$$

$$\hat{\mathcal{W}} = \hat{\sigma}_z (\hat{a} - \hat{a}^\dagger) + \hat{\sigma}_z (\hat{b} - \hat{b}^\dagger). \tag{1.111}$$

In the dispersive limit, where $|\lambda_\delta|,|\lambda_\Sigma|,|\lambda_\Omega| \ll 1$, the effective Hamiltonian $\hat{H}_{\mathrm{QS,int}} = \hat{\mathcal{U}}^\dagger \hat{H}_{\mathrm{QS}} \hat{\mathcal{U}}$ can be expanded to second order in λ_δ, λ_Σ and λ_Ω, yielding

$$\begin{aligned} \hat{H}_{\mathrm{QS,eff}} =& \hbar \frac{\omega_{\mathrm{Q}}}{2} \hat{\sigma}_z + \hbar \omega_{\mathrm{R}} \left(\hat{a}^\dagger \hat{a} + \hat{b}^\dagger \hat{b} \right) + \\ &+ \hbar \hat{\sigma}_z g_{\mathrm{dyn}} \left(\hat{a}^\dagger \hat{a} + \hat{b}^\dagger \hat{b} \right) + \\ &+ \hbar (g_{\mathrm{AB}} + g_{\mathrm{dyn}} \hat{\sigma}_z) \left(\hat{a}^\dagger \hat{b} + \hat{a} \hat{b}^\dagger \right). \end{aligned} \tag{1.112}$$

The *dynamic coupling* is given by

$$g_{\mathrm{dyn}} = \frac{(g \sin\theta)^2}{\omega_{\mathrm{Q}} - \omega_{\mathrm{R}}} + \frac{(g \sin\theta)^2}{\omega_{\mathrm{Q}} + \omega_{\mathrm{R}}}. \tag{1.113}$$

The effective Hamiltonian is comprised of the qubit and the two resonators. The resonant frequencies of the latter differ from the resonant frequencies of the bare resonators by dispersive shifts. The last term describes the coupling between the two resonators. The total resonator-resonator coupling

$$g_{\mathrm{res}} = g_{\mathrm{AB}} + g_{\mathrm{dyn}} \hat{\sigma}_z \tag{1.114}$$

is mediated by two mechanisms. The first is the constant geometric coupling g_{AB} which is determined solely by the sample layout. The second contribution depends on the qubit state and, via ω_{Q} and $\sin\theta$, on the external magnetic flux, cf. Fig. 1.14(b).

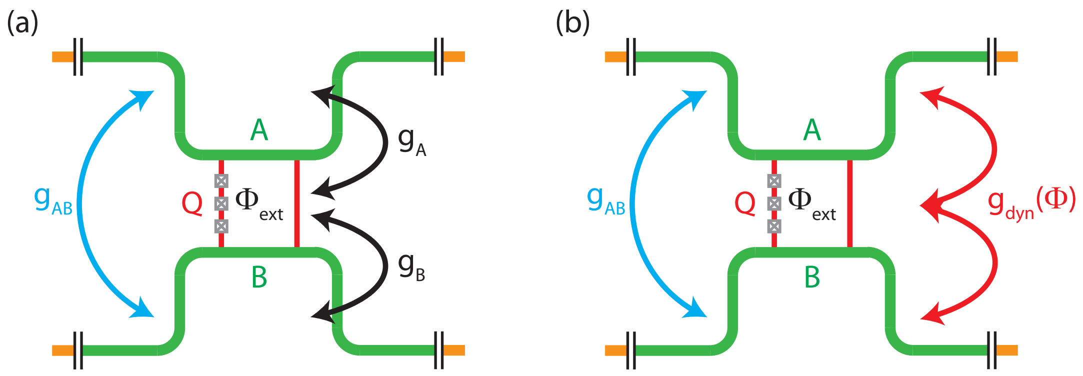

Figure 1.14: Layout of the quantum switch. (a) Two resonators A and B are coupled to a flux qubit Q with coupling strengths g_{A} and g_{B} (black arrows). The grey boxed crosses denote the Josephson junctions of the qubit. The geometric coupling strength between the two resonators is g_{AB} (blue arrow). The flux qubit can be tuned by varying the magnetic flux applied to the qubit loop. (b) The total resonator-resonator coupling strength is determined by the constant, geometry-dependent coupling and the second-order, flux-dependent dynamic coupling g_{dyn} (red arrows).

1.5.2 Flux qubit as tunable coupler

In this section we theoretically investigate two ways of controlling the coupling between the two resonators A and B: first, via the external magnetic field and, second, via the qubit population.

1.5.2.1 Tuning the coupling via the external field

Using $\sin\theta = \Delta/\hbar\omega_{\mathrm{Q}}$ and $\hbar\omega_{\mathrm{Q}} = \sqrt{\Delta^2+\epsilon^2}$, an analytical expression for the flux dependence of the dynamic coupling is

$$g_{\mathrm{dyn}} = \frac{2g^2\Delta^2}{\sqrt{\Delta^2+\epsilon^2}(\Delta^2-\omega_{\mathrm{R}}^2+\epsilon^2)}, \tag{1.115}$$

where $\epsilon = 2I_{\mathrm{p}}\delta\Phi_{\mathrm{ext}}$, cf. Eq. (1.70). If the qubit is kept in the ground state, i.e. $\langle\hat{\sigma}_z\rangle = -1$ and the parameters $g, g_{\mathrm{AB}}, \Delta$ and ω_{R} are designed to suitable values, there exist certain flux values where

$$g_{\mathrm{dyn}} = g_{\mathrm{AB}}. \tag{1.116}$$

We refer to this condition as the *switch setting condition*, where the coupling between the resonators is switched off. Further insight is gained by considering the normal modes of the coupled resonators

$$\hat{c}_{\pm} = \frac{1}{\sqrt{2}}(\hat{a}\pm\hat{b}), \quad \text{and} \quad \hat{c}_{\pm}^{\dagger} = \frac{1}{\sqrt{2}}(\hat{a}^{\dagger}\pm\hat{b}^{\dagger}), \tag{1.117}$$

which allows to rewrite the Hamiltonian of Eq. (1.112) to

$$\hat{H}_{\text{QS,eff}} = \hbar\frac{\omega_{\text{Q}}}{2}\hat{\sigma}_z + \hbar\omega_{\text{R}}(\hat{c}_+^\dagger\hat{c}_+ + \hat{c}_-^\dagger\hat{c}_-) + \hbar g_{\text{AB}}(\hat{c}_+^\dagger\hat{c}_+ - \hat{c}_-^\dagger\hat{c}_-) + 2\hbar g_{\text{dyn}}\hat{\sigma}_z\hat{c}_+^\dagger\hat{c}_+ = \tag{1.118}$$

$$= \hbar\frac{\omega_{\text{Q}}}{2}\hat{\sigma}_z + \hbar\omega_-\hat{c}_-^\dagger\hat{c}_- + \hbar(\omega_+ + 2g_{\text{dyn}}\hat{\sigma}_z)\hat{c}_+^\dagger\hat{c}_+, \tag{1.119}$$

with $\omega_- = \omega_{\text{R}} - g_{\text{AB}}$ and $\omega_+ = \omega_{\text{R}} + g_{\text{AB}}$. The modes $\hat{c}_-$ and $\hat{c}_+$ correspond to in-phase and out-of-phase oscillating currents in the two resonators, respectively. As only the out-of-phase oscillating mode generates a magnetic field at the position of the qubit, only this mode couples to the qubit. Figure 1.15 shows the flux dependence of the quantum switch modes for frequency-degenerate resonators and $\Delta > \omega_{\text{R}}$.

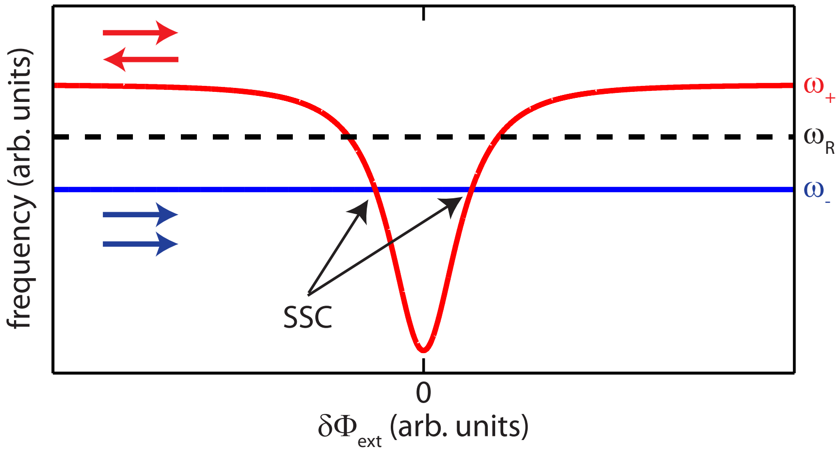

Figure 1.15: Numerical simulation of the mode spectrum of the quantum switch with the qubit in the ground state. The quantum switch modes ω_+ and ω_- are shown in red and blue, respectively. While the in-phase mode ω_- does not couple to the qubit, the out-of-phase mode ω_+ is shifted downwards by the dynamic coupling when the external magnetic flux is tuned towards the degeneracy point. At the switch setting conditions (SSC), the coupling between the two resonators is switched off. Black dashed line: Mode corresponding to a single uncoupled resonator.

1.5.2.2 Tuning the coupling via the qubit population

Next, we consider the case where the qubit is driven by a strong excitation signal. This results in equal probabilities to find the qubit in the ground and excited states, yielding the density matrix

$$\rho_{\text{M}} = \frac{1}{2}(|g\rangle\langle g| + |e\rangle\langle e|). \tag{1.120}$$

Consequently, the expectation value $\langle\hat{\sigma}_z\rangle = \text{Tr}[\rho_{\text{M}}\hat{\sigma}_z] = 0$. From Eq. (1.112) and Eq. (1.118), we find that in this scenario the coupling between the two resonators is given by g_{AB} independently of the external magnetic flux applied to the qubit loop.

For weak qubit drive signals, the probability $P_{|g\rangle}$ of finding the qubit in the ground state is higher than finding the qubit in the excited state as a consequence of the qubit decay rate. The corresponding density matrix is thus given by

$$\rho_{\mathrm{M,weak}} = P_{|g\rangle}|g\rangle\langle g| + (1 - P_{|g\rangle})|e\rangle\langle e|. \tag{1.121}$$

Hence, the expectation value $\langle\hat{\sigma}_z\rangle_{\mathrm{weak}} = \mathrm{Tr}[\rho_{\mathrm{M,weak}}\hat{\sigma}_z] = P_{|g\rangle} - \frac{1}{2}$ and therefore the total coupling between the resonators can be adjusted to arbitrary values between $(g_{\mathrm{AB}} - g_{\mathrm{dyn}})$ and g_{AB} by adjusting the qubit drive power [122].

1.5.2.3 Nonclassical states and entanglement

The quantum nature of the coupling element, the flux qubit, can be utilized to create nonclassical states and entanglement. For a detailed description of the protocols presented below we refer to Ref. [120]. The two resonators A and B can be entangled by preparing resonator A in Fock state $|1\rangle_{\mathrm{A}}$ and resonator B in $|0\rangle_{\mathrm{B}}$ with the switch turned off, i.e. the coupling between the resonators is off. Subsequently, we turn on the switch such that the coupling between the resonators is given by a finite coupling strength g^{on}. After a time t, a coherent linear superposition of bipartite states is created,

$$\cos(g^{\mathrm{on}}t)|1\rangle_{\mathrm{A}}|0\rangle_{\mathrm{B}} + \sin(g^{\mathrm{on}}t)|0\rangle_{\mathrm{A}}|1\rangle_{\mathrm{B}}. \tag{1.122}$$

Choosing $t = \pi/4g^{\mathrm{on}}$ yields the maximally entangled state

$$\frac{|1\rangle_{\mathrm{A}}|0\rangle_{\mathrm{B}} + |0\rangle_{\mathrm{A}}|1\rangle_{\mathrm{B}}}{\sqrt{2}}. \tag{1.123}$$

Starting from the same initial condition as above allows to create tripartite entangled states. To this end, the qubit is brought into the state $(|g\rangle + |e\rangle)/\sqrt{2}$ before the switch is turned on for a time $t = \pi/2g^{\mathrm{on}}$, yielding the Greenberger-Horne-Zeilinger [123] state

$$\frac{|g\rangle|1\rangle_{\mathrm{A}}|0\rangle_{\mathrm{B}} + \mathrm{e}^{\imath\pi/2}|e\rangle|0\rangle_{\mathrm{A}}|1\rangle_{\mathrm{B}}}{\sqrt{2}}. \tag{1.124}$$

Finally, the quantum switch architecture also allows to generate entangled coherent states. Again, resonator B is prepared in the vacuum state and the qubit in $(|g\rangle + |e\rangle)/\sqrt{2}$, however, in contrast to the previous initial conditions, resonator A is populated with a coherent state $|\alpha\rangle$. After switching on the coupling and waiting for a time $t = \pi/2g^{\mathrm{on}}$, the Schrödinger cat state [124]

$$\frac{|g\rangle|\alpha\rangle_{\mathrm{A}}|0\rangle_{\mathrm{B}} + \mathrm{e}^{\imath\pi/2}|e\rangle|0\rangle_{\mathrm{A}}|\alpha\rangle_{\mathrm{B}}}{\sqrt{2}} \tag{1.125}$$

is generated. All these examples reveal the quantum nature of the switch and open the door to applications not feasible with coupling circuits composed of SQUIDs or tunable inductances [54, 56, 58, 125].

Chapter 2

Experimental techniques

In the course of this thesis, two circuit QED samples were investigated. The first one consists of a flux qubit coupled galvanically to a transmission line resonator and therefore comes close to the prototypical circuit QED architecture. We refer to this sample as the *flux qubit sample*. The second sample, referred to as the *flux qubit coupler*, consists of a flux qubit coupled galvanically to two coplanar stripline resonators and is described theoretically in Sec. 1.5.

In this chapter, we discuss the experimental setup and the measurement techniques required to characterize our samples. In order to perform measurements at the single microwave photon level, experiments with superconducting samples have to be performed at millikelvin temperatures. We therefore provide a description of the cryostat and show how microwave and dc signals are delivered to and received from our circuit QED samples.

Subsequently, we describe the two most important microwave spectroscopy protocols needed to infer relevant resonator and qubit parameters. Finally, we discuss the technological aspects of time-domain spectroscopy which provides experimental access to the coherence properties of a quantum bit.

2.1 Continuous-wave spectroscopy

Continuous-wave spectroscopy measurements represent the most important technique to characterize circuit QED setups as they provide experimental access to characteristic resonator and qubit properties such as resonant frequencies or line widths. In this section we discuss the cryogenic and room-temperature equipment required to perform such measurements.

2.1.1 Setup

Both samples investigated in the course of this thesis are mounted inside gold-plated copper boxes onto the base temperature stage of a dilution refrigerator. Equipping the refrigerator with microwave and dc lines was performed by the author and three other PhD students. The cryostat is notable for its large sample space where at least four circuit QED samples can be cooled down in parallel. Despite featuring seven microwave input lines, four microwave output lines and 64 dc wires, the cryostat still reaches a base temperature below 30 mK. The cryogenic setup for one of the samples characterized in the course of this thesis, the flux qubit sample, is shown in Fig. 2.1.

2.1.1.1 Spectroscopy setup for the flux qubit sample

The spectroscopy setup for the flux qubit sample is shown schematically in Fig. 2.2. Both resonator ports are connected to microwave lines. One of these lines, denoted as the input line, allows to apply a probe signal to the resonator. The probe signal is generated at room temperature by a vector network analyzer (Rohde & Schwarz ZVA24). For typical transmission measurements, the mean resonator population is around one photon on average (poa), corresponding to powers on the order of attowatts (10^{-18} W). To ensure a sufficient signal-to-noise ratio even for these small powers, the output signal of the VNA has to be several orders of magnitude larger than the room temperature thermal noise power which inevitably adds to the wanted input signal. The signal applied to the input microwave line, consisting of the wanted signal and thermal noise, is attenuated at the different temperature stages of the cryostat. Since each attenuator also adds thermal noise corresponding to the temperature stage at which it is mounted, an optimal signal-to-noise ratio would be achieved if attenuation would only be done at the base temperature stage of the cryostat. However, the dissipated power would by far exceed the cooling power of the cryostat at the base temperature stage. Thus, the attenuators are distributed over the various temperature stages of the cryostat in a way that the signal-to-noise ratio at the sample input is optimal and the dissipated power at each attenuator does not exceed the cooling power of the respective temperature stage. For a detailed description of the attenuator configuration, we refer to Ref. [126].

The signal transmitted through the resonator passes two cryogenic circulators before it is amplified by a cryogenic HEMT[1] amplifier (Low Noise Factory LNC4_8A) and, after passing a room temperature circulator, by a second amplifier (Miteq JS2) at room temperature. The circulators isolate the HEMT amplifier and the sample from thermal noise and reflected signal components propagating down via the output line. The amplified signal is eventually detected by the input port of the VNA. In this way, the transmission

[1]high electron mobility transistor

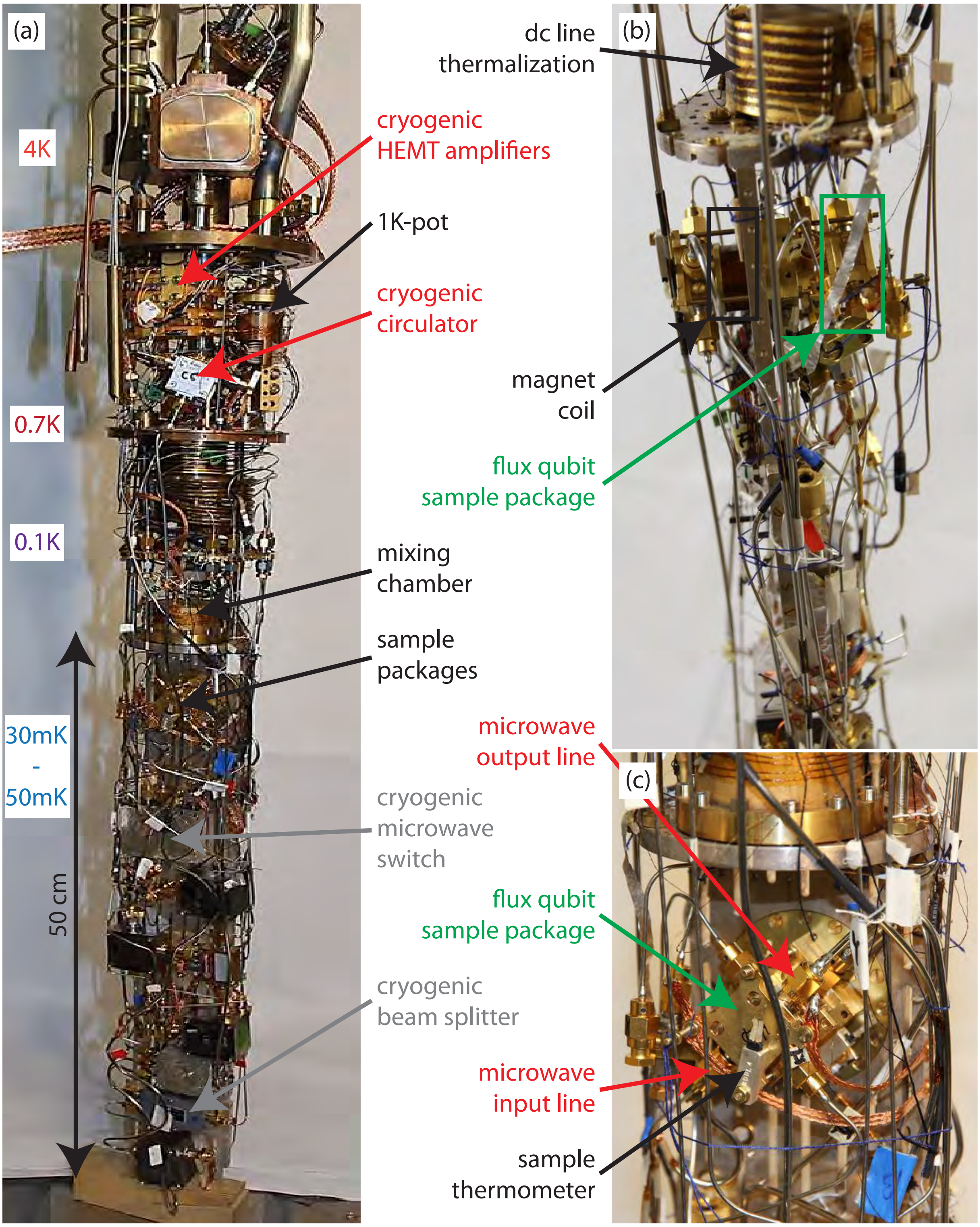

Figure 2.1: The dilution refrigerator. Green labels: Flux qubit sample package. Red labels: Important microwave components used for measurements on the samples discussed in this thesis. Grey labels: Cryogenic microwave switches and beam splitters allow us to use one input line for multiple experiments. Black labels: Technical components of the cryostat and the experimental setup. (a) Temperature stages of the cryostat from 4 K to base temperature. The base temperature stage is 50 cm long. (b) Side view of the sample rod. (c) Front view of the sample rod.

through the resonator can be measured.
In addition, the qubit can be excited using an on-chip antenna connected to an additional input line referred to as the antenna line. Similar to the resonator input line, attenuators are installed at the different temperature stages of the cryostat to ensure good signal-to-noise ratio at base temperature. The signal applied to the qubit via the antenna is generated by a microwave source (Rohde & Schwarz SMF 100A). The latter and the VNA are synchronized using a 10 MHz rubidium reference source (Stanford Research FS 725). The magnetic field applied to the flux qubit is controlled by a superconducting solenoid mounted close to the sample box.

2.1.1.2 Spectroscopy setup for the flux qubit coupler

The flux qubit coupler sample features a flux qubit coupled galvanically to two superconducting resonators, cf. Sec. 1.5. One port of each resonator is connected to a highly attenuated input line and the other port to an output line containing cryogenic and room temperature circulators and amplifiers. This configuration allows us to measure the transmission through both individual resonators and also allows us to measure the transmission from the input port of one resonator to the output port of the other resonator. Transmission measurements are performed using a 4-port vector network analyzer (Rohde & Schwarz ZVA24). The flux qubit coupler does not feature an antenna to drive or excite the qubit. Instead, qubit drive or excitation signals are fed down to the sample via one of the resonator input lines. To this end, a beam splitter is installed at room temperature allowing to combine the output signals of the VNA and an additional microwave source (Rohde & Schwarz SMF 100A). The latter and the VNA are synchronized using a 10 MHz reference source. The magnetic flux applied to the qubit loop is again controlled by a superconducting coil mounted in the vicinity the sample box.

2.1.2 Transmission spectroscopy

In circuit QED architectures comprised of quantum bits coupled to resonators, transmission spectroscopy provides the most straightforward experimental access to determine the resonator mode frequencies. In measurement setups such as the ones depicted in Fig. 2.2 and Fig. 2.3, transmission is measured by a VNA with the qubit kept in the ground state, i.e. $\langle\hat{\sigma}_z\rangle = -1$. Provided that the qubit is far detuned from the resonator, the detected resonant frequency is given by $\tilde{\omega}_\mathrm{R} = \omega_\mathrm{R} - g^2 \sin^2\theta/\delta$, cf. Eq. (1.98). For very large detunings $\delta \gg g^2 \sin^2\theta$, the dispersive shift is negligible and the bare resonator mode frequencies are observed. The frequency response of such transmission spectroscopy measurements is given by a Lorentzian line shape, cf. Sec. 1.2.2, allowing to extract the line width, and therefore the quality factor, of the resonator under test.

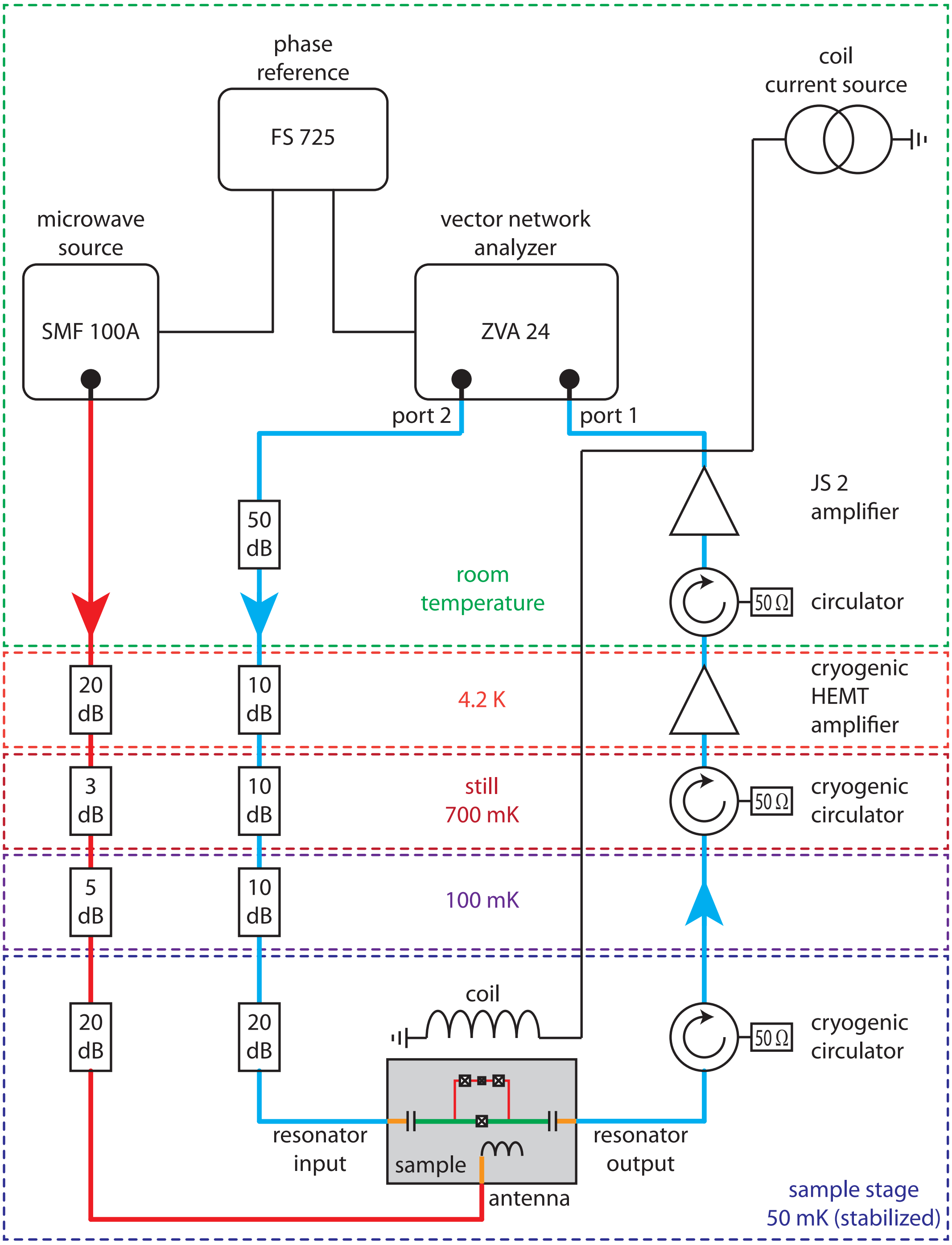

Figure 2.2: Spectroscopy setup for the flux qubit sample. A vector network analyzer is connected to resonator input and output lines (blue). The resonator input signal is attenuated passing through the different temperature stages. The output port of the resonator is isolated from noise propagating down via the output line by cryogenic circulators. The resonator output signal is amplified at the 4.2 K stage by a low-noise HEMT amplifier and at room temperature by an additional amplifier. An excitation signal generated by an additional microwave source can be applied to the qubit by means of an antenna (red line). The magnetic field applied to the flux qubit can be controlled via a superconducting coil mounted on top of the sample package.

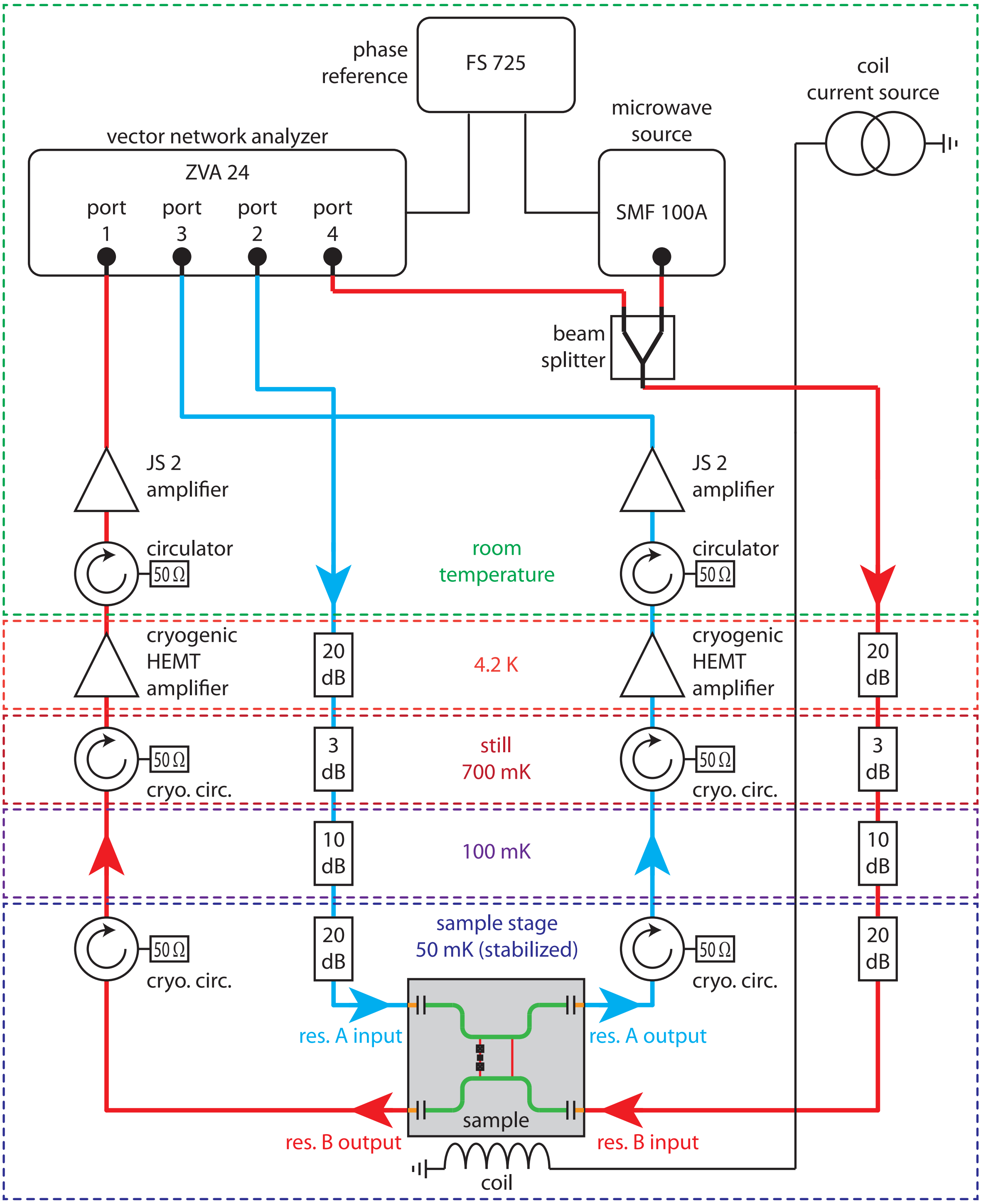

Figure 2.3: Spectroscopy setup for the flux qubit coupler. Both resonators are connected to one input and one output line each, allowing to measure the transmission through individual resonators and also the transmission from the input of one resonator to the output of the other resonator. In addition, a qubit excitation signal can be applied through resonator B.

Transmission spectroscopy can also be used to calibrate the magnetic flux applied to the flux qubit. As discussed in Sec. 1.3.4 and Sec. 1.3.5, the flux qubit transition frequency is Φ_0-periodic. As a consequence, the dispersively shifted mode frequency is also Φ_0-periodic, allowing to relate electric currents applied to a superconducting solenoid mounted in the vicinity of a coupled qubit-resonator-system to the magnetic flux penetrating the qubit loop.

2.1.3 Two-tone spectroscopy of the qubit

Even though the presence of a flux qubit manifests itself in magnetic field dependent shifts of the resonant frequencies, transmission spectroscopy does not provide direct access to the qubit transition frequency. The latter can be detected using two-tone spectroscopy. From a theoretical point of view, this measurement technique is based on the qubit state dependence of the dispersively shifted resonant frequency,

$$\tilde{\omega}_{\mathrm{R}} = \omega_{\mathrm{R}} \pm \frac{g^2 \sin^2\theta}{\delta}\langle\hat{\sigma}_z\rangle. \tag{1.98}$$

If the qubit is in the ground state, i.e. $\langle\hat{\sigma}_z\rangle = -1$, resonance occurs at $\omega_{\mathrm{R}} - \chi$, where $\chi = g^2\sin^2\theta/\delta$ denotes the dispersive shift. If the qubit is driven, i.e. it is put in a classical superposition with equal probabilities of finding the qubit in the ground or excited state as described by the density matrix $\rho_{\mathrm{M}} = \frac{1}{2}(|g\rangle\langle g| + |e\rangle\langle e|)$, the expectation value $\langle\hat{\sigma}_z\rangle = \mathrm{Tr}[\rho_{\mathrm{M}}\hat{\sigma}_z] = 0$. Consequently, resonance occurs at the bare resonator frequency ω_{R}, cf. Fig. 2.4. In a two-tone spectroscopy measurement, one frequency is chosen as the so-called *probe tone frequency*. To ensure good measurement contrast, typically either the bare resonator frequency ω_{R} or the dispersively shifted resonant frequency for the qubit being in the ground state, $\omega_{\mathrm{R}} - \chi$, is chosen.

Using a second microwave source, the so-called *spectroscopy tone* is applied to the qubit. This can be done via an antenna as shown in Fig. 2.2 or directly via the resonator as indicated in Fig. 2.3. In the latter case, the spectroscopy tone power has to be increased in order to overcome the filtering effect of the resonator since the spectroscopy tone typically is off-resonant with the cavity. If the spectroscopy tone frequency matches the qubit transition frequency, the expectation value $\langle\hat{\sigma}_z\rangle$ changes and takes the value of $\langle\hat{\sigma}_z\rangle = 0$ if the spectroscopy tone power is strong enough to saturate the qubit. Consequently, the resonant frequency of the coupled qubit-resonator system shifts to the bare resonator frequency ω_{R}. As indicated in Fig. 2.4(a), transmission at the probe tone frequency decreases if the latter is chosen as the dispersively shifted cavity frequency $\tilde{\omega}_{\mathrm{R}}$. Contrarily, if the bare resonator frequency ω_{R} is chosen as the probe tone frequency, transmission increases if the qubit is saturated by the spectroscopy tone. Alternatively, also the phase of the transmitted probe tone can be monitored in order to detect the qubit frequency as shown in Fig. 2.4(b). The strong dependence on the frequency makes the transmitted phase a precise meter for determining whether the resonator is dispersively shifted or not, i.e. whether the qubit is in the ground state or driven. This is especially useful if the dispersive shift χ is smaller than the resonator linewidth and the difference in the probe tone transmission magnitude between the qubit in the ground state and the driven qubit is small. An advantage of choosing the dispersively shifted resonant frequency as the

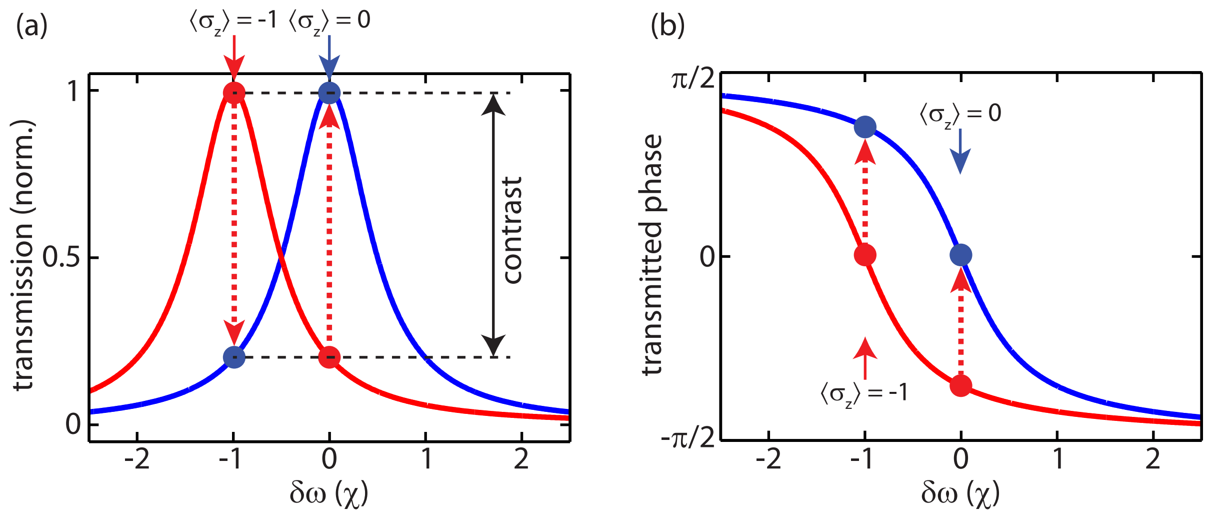

Figure 2.4: Working principle of two-tone spectroscopy. (a) Readout using the transmission magnitude. Red line: Lorentzian transmission amplitude of the resonator. The resonant frequency is dispersively shifted due to the presence of the qubit in the ground state. Blue line: If the qubit is saturated by a strong spectroscopy tone, the resonant frequency is shifted to the bare resonator frequency. Saturating the qubit manifests itself in decreased transmission at the probe tone frequency if the latter matches the dispersively shifted resonant frequency or in increased transmission if the bare resonator frequency is chosen as probe tone frequency. (b) Readout using the transmission phase[65]. Especially if the dispersive shift χ is small, the phase represents a more precise meter for the qubit state than the transmission magnitude.

probe tone frequency is that it can be measured directly using transmission spectroscopy, see Sec. 2.1.2. However, the dispersive shift depends on the qubit transition frequency and therefore on the magnetic flux applied to the qubit loop. This implies that the probe tone frequency has to be redetermined every time the magnetic flux is changed. If known, it is advantageous to set the probe tone frequency to the bare resonator frequency ω_R since the latter does not depend on the magnetic flux applied to the qubit loop.

To map out the hyperbolic dependence of the qubit transition frequency on the external magnetic flux [cf. Eq. (1.72)], the qubit transition frequency is determined depending on the external magnetic flux applied to the qubit.

2.1.4 Power calibration

The mean number of photons in the resonator is not accessible directly in most circuit QED setups. Even though the output power of microwave sources can be set to a well defined value, the signal loss of microwave cables, attenuators and other microwave components is afflicted with large uncertainties, one reason being the strong dependence of the transmission properties of the latter on the temperature. In addition, also the resonator's insertion loss is not directly accessible. However, the two-tone spectroscopy protocol described in the previous section provides a very precise method to calibrate the mean number of photons in the resonator. To this end, we again consider the Jaynes-Cummings Hamiltonian in the dispersive regime,

$$\hat{H}_{\mathrm{JC}}^{\mathrm{disp}} \approx \hbar\omega_{\mathrm{R}} \left(\hat{a}^\dagger \hat{a} + \frac{1}{2} \right) + \frac{\hbar}{2} \left[\omega_{\mathrm{Q}} + \frac{2g^2 \sin^2\theta}{\delta} \hat{a}^\dagger \hat{a} + \frac{g^2 \sin^2\theta}{\delta} \right] \hat{\sigma}_z. \qquad (1.99)$$

Introducing the number of photons in the resonator $n = \hat{a}^\dagger \hat{a}$, we can see that the qubit transition frequency is shifted to $\tilde{\omega}_{\mathrm{Q}} = \omega_{\mathrm{Q}} + (2n+1)\chi$ if the resonator is populated with n photons on average.

To calibrate the number of photons in the cavity, two-tone spectroscopy is performed at a fixed magnetic flux for varying probe tone powers. Assuming that the signal loss between microwave source and sample is independent of the power, the frequency shift of the qubit is proportional to the mean number of photons n in the resonator[2]. For weak drive powers, i.e. $n \approx 0$, the bare qubit transition frequency, shifted only by the constant Lamb shift, $\omega_{\mathrm{Q}} + \chi$ is detected by the two-tone spectroscopy protocol. If the dispersive shift χ is known, the mean number of photons in the resonator can be derived from the probe tone power dependence of the qubit transition frequency.

In many experiments, the qubit does couple to more than one mode, cf. Sec. 1.4.3. In this scenario, power calibration should be performed for all relevant resonator modes. The reason for this is that cable losses and also the resonator's insertion loss strongly depend on the frequency.

2.2 Time domain spectroscopy

For practical applications in the fields of quantum information processing, the required protocols can only be executed successfully if quantum information can be stored in the constituents of circuit QED architectures for time spans long enough to complete the respective protocols. To this end, knowledge of the coherence times (cf. Sec. 1.3.6) of quantum bits is essential. In this section, we discuss the measurement technique allowing

[2]We note that proportionality only holds for small n.

us to measure the energy relaxation time T_1 of a flux qubit coupled to a transmission line resonator.

2.2.1 Setup

The measurement protocol allowing us to determine whether a qubit is in the excited or ground state is based on the principles of two-tone spectroscopy. The main extension to the protocol discussed in Sec. 2.1.3 is that the transmission through the resonator, i.e. the probe tone, is recorded in a time-resolved way. In our experiments, the probe tone frequency matches the dispersively shifted resonant frequency. Eventually, we infer the probability of finding the qubit in the excited state as a function of time from reading magnitude and phase of the transmitted spectroscopy tone in a time-resolved way.

2.2.1.1 Time-domain detection setup

The detector used in our measurements is an FPGA[3]-enhanced A/D-converter with a sampling rate of 150 MHz. As a consequence, the probe tone has to be converted from the GHz-regime down to the MHz-regime before detection using a technique referred to as *heterodyne detection*. Down-conversion is performed by an IQ-mixer, the central building block of the measurement setup shown in Fig. 2.4.

A (single-ended) mixer is a nonlinear electrical device multiplying the *input signal* at frequency ω_p, which in our case is the spectroscopy tone, with an additional microwave signal called *local oscillator* at frequency ω_LO. Following trigonometric identities, the resulting output signal consists of two components, one at the difference frequency $\omega_\mathrm{p} - \omega_\mathrm{LO}$ and one at the sum frequency $\omega_\mathrm{p} + \omega_\mathrm{LO}$. The difference frequency is referred to as *intermediate frequency* ω_IF and in our case set to 10 MHz. The sum frequency therefore is in the GHz-regime and can thus be filtered out using a low-pass filter.

An IQ-mixer is a parallel connection of two identical single-ended mixers where the local oscillator is shifted by 90° between both mixers. Considering an input signal of the form

$$P(t) = \tilde{A}(t)\sin(\omega_\mathrm{p} t + \phi(t)) \tag{2.1}$$

and a local oscillator of the form $LO(t) = B\sin(\omega_\mathrm{LO} t) = B\sin((\omega_\mathrm{p} + \omega_\mathrm{IF})t)$, an ideal IQ-mixer yields the *quadratures*

$$I_\mathrm{IF}(t) = A(t)\cos(\omega_\mathrm{IF} t + \phi(t)) \tag{2.2}$$

$$Q_\mathrm{IF}(t) = A(t)\sin(\omega_\mathrm{IF} t + \phi(t)). \tag{2.3}$$

[3]field-programmable gate array, Innovative Integration Virtex-5, X5-RX

From these equations it can be seen why using an IQ-mixer is advantageous compared to a single-ended mixer. If one tries to infer amplitude and phase from, e.g., $I_{\mathrm{IF}}(t)$ alone, there are points in time where the cosine, and therefore $I_{\mathrm{IF}}(t)$, is zero. At these points, all information about $A(t)$ is lost. However, the absolute value of the sine in $Q_{\mathrm{IF}}(t)$ is maximum when the cosine in $I_{\mathrm{IF}}(t)$ is zero. In this way, information about the amplitude $A(t)$ is accessible at all times.

As indicated in Fig. 2.5, I and Q are subsequently amplified such that their amplitude is slightly below the maximum input amplitude of the A/D-converter. In this way, the resolution of 16 bits of the latter can be fully used. In addition, the signal is filtered by band pass filters to avoid higher harmonics of the IF signal. At a sampling rate

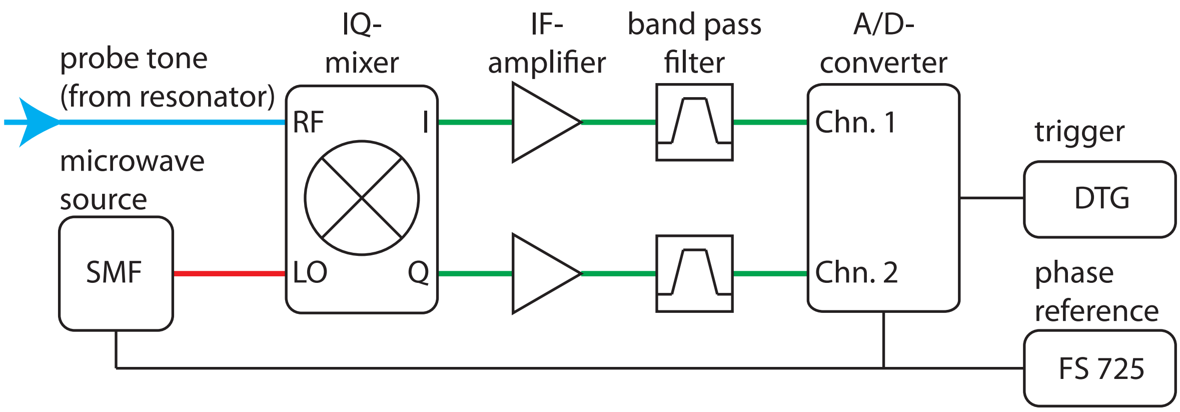

Figure 2.5: Schematic of the time-domain detection setup. The probe tone is converter down to the intermediate frequency by means of an IQ-mixer and subsequently amplified and filtered. An FPGA-enhanced A/D-converter is used to digitize the signal. The microwave source generating the local oscillator and the A/D-converter are connected to a 10 MHz reference source.

of 150 MHz and an IF-frequency of 10 MHz, 15 data points are recorded by the A/D-converter per oscillation, allowing for a precise reconstruction of the quadratures $I_{\mathrm{IF}}(t)$ and $Q_{\mathrm{IF}}(t)$. From a mathematical point of view, also $\omega_{\mathrm{IF}} = 0$ could be chosen, referred to as *homodyne detection*. However, the latter is disadvantageous since the resulting DC-signal is susceptible to $1/f$-noise and drifts [69].

Since the wanted component of the transmitted probe tone is overlain by noise, a large number of traces (typically 10^5 to 10^8) has to be recorded and averaged. The averaging process is very sensitive to phase fluctuations, thus, the microwave sources generating the probe tone and the local oscillator, the A/D-converter and also the pulse generator providing the trigger for the A/D-converter have to be synchronized by a 10 MHz reference source.

Amplitude and phase of the probe tone are extracted from the trace-averaged I_{IF} and Q_{IF} by applying a transformation rotating the quadratures at the frequency ω_{IF} [69], which corresponds to applying the matrix

$$R(t) = \begin{pmatrix} \cos\omega_{\mathrm{IF}}t & \sin\omega_{\mathrm{IF}}t \\ -\sin\omega_{\mathrm{IF}}t & \cos\omega_{\mathrm{IF}}t \end{pmatrix} \tag{2.4}$$

to the vector $(I(t), Q(t))^{\top}$, yielding the quadratures of the wanted component of the probe tone,

$$I(t) = A(t)\cos(\phi(t)), \tag{2.5}$$

$$Q(t) = A(t)\sin(\phi(t)). \tag{2.6}$$

This method is referred to as *digital homodyning*. However, due to technical imperfections, the amplitudes of the I_{IF} and Q_{IF} signals may not be the same. Furthermore, also the phase difference between the two quadratures may differ from 90°. As a result, the averaged quadratures of the IF signal have to be corrected for these imperfections. To this end, a microwave test signal with good signal-to-noise ratio is generated by a microwave source and applied to the input of the IQ-mixer. Following Ref. [69], we assume that the imperfect quadratures of the IF-signal can be written as

$$I_{\mathrm{IF}}^{\mathrm{imp}}(t) = (A(t) + \epsilon_{\mathrm{A1}})\cos(\omega_{\mathrm{IF}}t + \phi(t)), \tag{2.7}$$

$$Q_{\mathrm{IF}}^{\mathrm{imp}}(t) = (A(t) + \epsilon_{\mathrm{A2}})\sin(\omega_{\mathrm{IF}}t + \phi(t) + \epsilon_{\phi}). \tag{2.8}$$

Amplitude imbalances in the two channels can be corrected by a matrix of the form

$$E_{\mathrm{A}} = \begin{pmatrix} (1+\epsilon_{\mathrm{a1}})^{-1} & 0 \\ 0 & (1+\epsilon_{\mathrm{a2}})^{-1} \end{pmatrix}. \tag{2.9}$$

As shown in Ref. [69], imperfections in the phase difference between $I_{\mathrm{IF}}^{\mathrm{imp}}(t)$ and $Q_{\mathrm{IF}}^{\mathrm{imp}}(t)$ can be corrected by means of the matrix

$$E_{\phi} = \frac{1}{\cos(\epsilon_{\phi})} \begin{pmatrix} \cos\omega_{\mathrm{IF}}t + \epsilon_{\phi} & \sin\omega_{\mathrm{IF}}t \\ \sin\omega_{\mathrm{IF}}t + \epsilon_{\phi} & \cos\omega_{\mathrm{IF}}t \end{pmatrix}. \tag{2.10}$$

The quadratures $I(t)$ and $Q(t)$ are than obtained by calculating

$$\begin{pmatrix} I(t) \\ Q(t) \end{pmatrix} = E_{\phi}E_{\mathrm{A}} \begin{pmatrix} I_{\mathrm{IF}}^{\mathrm{imp}}(t) \\ Q_{\mathrm{IF}}^{\mathrm{imp}}(t) \end{pmatrix}. \tag{2.11}$$

We note that this correction method only works for $\epsilon_{\phi} \ll \pi/2$. For a signal correction method working also for larger phase errors, we refer to Ref. [126].

2.2.1.2 Pulse generation

In order to manipulate the qubit state in a controlled way, microwave pulses of a well defined duration τ, corresponding to a well defined amount of energy, have to be applied to the qubit. In our case, these pulses are generated by means of a mixer. The latter multiplies a sinusoidal microwave tone at frequency ω_s (generated by a microwave source[4]) with a rectangular pulse, in our case generated by the Tectronix DTG 5334 pulse generator. The corresponding setup is sketched in Fig. 2.6. Again, microwave source and pulse generator are connected to the same phase reference as the one shown in Fig. 2.5. The pulse generator also provides the trigger pulse for the A/D-converter discussed in the previous section, synchronizing pulse generation and signal detection. Technically, two

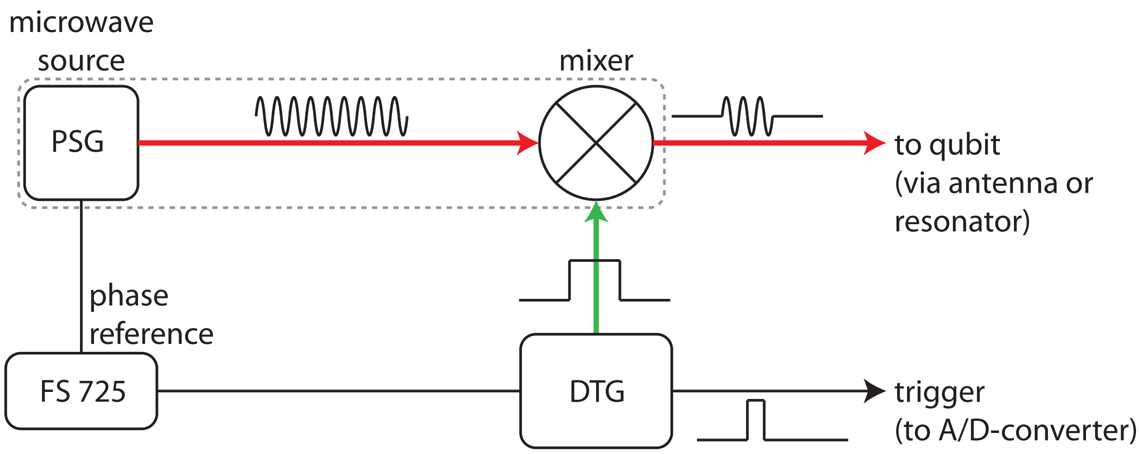

Figure 2.6: Pulse generation setup. A sinusoidal continuous-wave signal generated by a microwave source is mixed with a rectangular pulse to create a microwave pulse. As indicated by the grey dashed line, the mixer may be integrated in the microwave source. The pulse generator also creates the trigger pulse for the A/D-converter discussed in Sec. 2.2.1.1. Microwave source and pulse generator are synchronized by a 10 MHz reference source.

alternatives are available for the mixer. One is to use the internal mixer of the microwave source. However, this method is not suitable for short pulses (< 5 ns) and closely spaced pulse sequences. If one of the latter is required, pulses can also be created by external mixers. A serial combination of two single-ended mixers as sketched in Fig. 2.7 ensures a sufficient on/off-ratio of the microwave pulse. We note that the cables connecting the outputs of the beam splitter to the inputs of the mixers should be identical and the connection between the two mixers should be as short as possible to keep signal propagation delays, which may distort the pulse shape, as small as possible.

[4]Agilent E8267D PSG

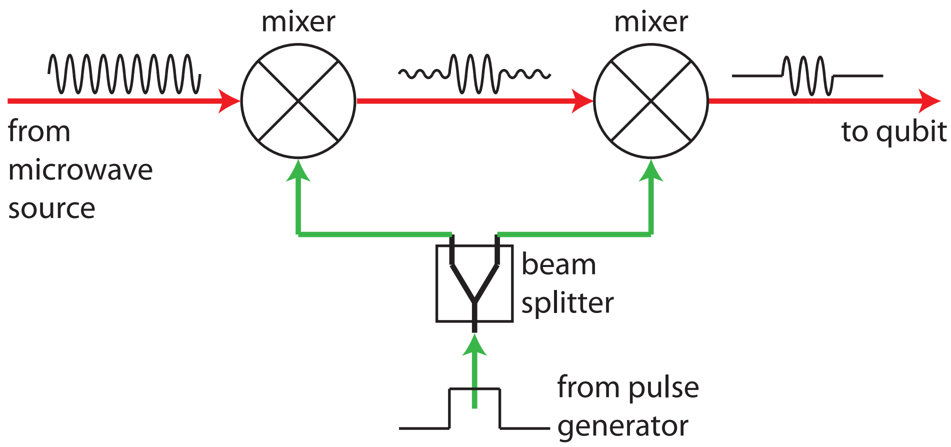

Figure 2.7: Pulse generation by external mixers. To ensure sufficient on/off ratio of the microwave pulse, a serial combination of two single-ended mixers is used.

2.2.2 Rabi measurements

The measurement of Rabi oscillations represents one of the most important measurement techniques providing experimental access to the energy relaxation time T_1. Applying a short microwave pulse with duration τ to the qubit changes the polar angle of its state on the Bloch sphere depending on the energy transferred to the qubit, see Fig. 2.8. The final state on the Bloch sphere can be described by

$$|\Psi\rangle = \alpha|g\rangle + \beta|e\rangle, \tag{2.12}$$

where $\alpha,\beta \in \mathbb{C}$ and $|\alpha|^2 + |\beta|^2 = 1$. After state preparation, the qubit state is read out by means of the time-domain detection technique described in Sec. 2.2.1.1. The ground state will be detected with probability $|\alpha|^2$ and the excited state with probability $|\beta|^2$. Typically, between 10^5 and 10^8 traces are recorded and averaged for each pulse length applied to the qubit, allowing for a precise determination of $|\alpha|$ and $|\beta|$. Due to the finite interaction of the qubit with its environment, cf. Sec. 1.3.6, the qubit will only maintain its state for a finite time before it decays to the ground state. This energy relaxation process occurs with a probability proportional to $[1 - \exp(-t/T_1)]$. Thus, independently of the qubit state after applying the pulse, after a time $t \gg T_1$ it will always be back in state $|g\rangle$.

For certain combinations of pulse duration and power, the qubit is brought from the ground state $|g\rangle$ to the excited state $|e\rangle$, cf. Fig. 2.8. Such a pulse is referred to as π-pulse as it changes the polar angle of the qubit state by 180°. Interestingly, a qubit can also be brought from the excited state to the ground state by the same π-pulse. It is worth mentioning that the latter also is the most important difference between a quantum two-level system and a quantum harmonic oscillator, where an arbitrary number of photons

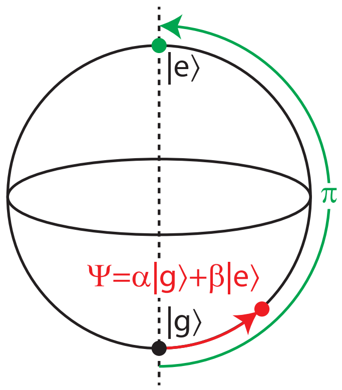

Figure 2.8: Bloch sphere representation of the qubit state. The south pole is identified with the qubit ground state and the north pole with the excited state. A π-pulse (green arrow) applied to the qubit in the ground state changes its state to the excited state. Pulses of arbitrary duration (red arrow) displace the polar angle of the qubit state such that the final state is described by $|\Psi\rangle = \alpha|g\rangle + \beta|e\rangle$.

can be stored in any resonant mode. This effect also gives rise to the so-called *driven Rabi oscillations*. For a given pulse energy, the expectation values for $|\alpha|$ and $|\beta|$ are periodic with respect to the pulse duration. This is best understood considering that a $(2n-1)\,\pi$-pulse, drives the transition $|g\rangle \rightarrow |e\rangle$ for all $n \in \mathbb{N}$ as long as the pulse duration $\tau \ll T_1$. The corresponding periodicity is referred to as *Rabi frequency*. Since the pulse energy depends linearly on the pulse amplitude, the duration of, for example, a π-pulse is inversely proportional to the pulse amplitude. As a consequence, the Rabi frequency scales linearly with pulse amplitude.

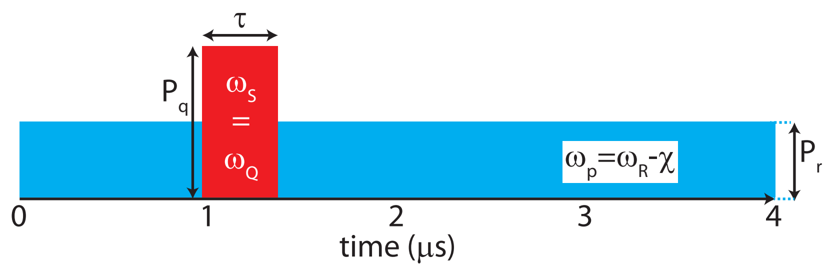

Figure 2.9: Pulse scheme for Rabi measurements. The resonator is probed by means of a weak continuous sinusoidal signal at the dispersively shifted resonant frequency. A microwave pulse with the qubit transition frequency and length τ is used to excite the qubit. The time $t = 0$ corresponds to the point in time where the A/D-converter is triggered.

The pulse scheme used to measure these Rabi oscillations is sketched in Fig. 2.9. The resonator is probed with a continuous probe tone at the frequency of the dispersively shifted resonator. The probe tone power is chosen as low as possible in order not to impose a power-dependent shift on the qubit frequency. Typical mean resonator populations are around one photons on average or less. Microwave excitation pulses at the qubit transition frequency with variable duration are applied to the qubit at a repetition rate low enough to ensure the qubit relaxes back to the ground state between subsequent pulses. In our case, the time between the rising edges of two pulses was set to 4 µs.

Next, we show in detail how the time-dependent probability of finding the qubit in the excited state is measured after a π-pulse has been applied to the qubit. The transmitted resonator probe tone is recorded in a time-resolved way using the setup discussed above. Figure 2.10 shows the raw, uncorrected I and Q quadratures averaged over 2.3×10^7 traces as detected by the A/D-converter. The π-pulse has been applied to the qubit 1 µs after recording of the A/D-converter is started as shown in Fig. 2.9. At approximately 1.2 µs, a clear decrease in the magnitudes of I and Q is observed in agreement with decreased resonator probe tone transmission which is expected when the qubit is excited. The reason that the response of the probe tone to the qubit excitation pulse is visible with an additional delay of approx. 200 ns is that the internal mixer of the PSG microwave source, which is used to create the qubit excitation pulse, imposes a delay on the pulse. The phase and amplitude errors in the raw I and Q time traces are subsequently corrected

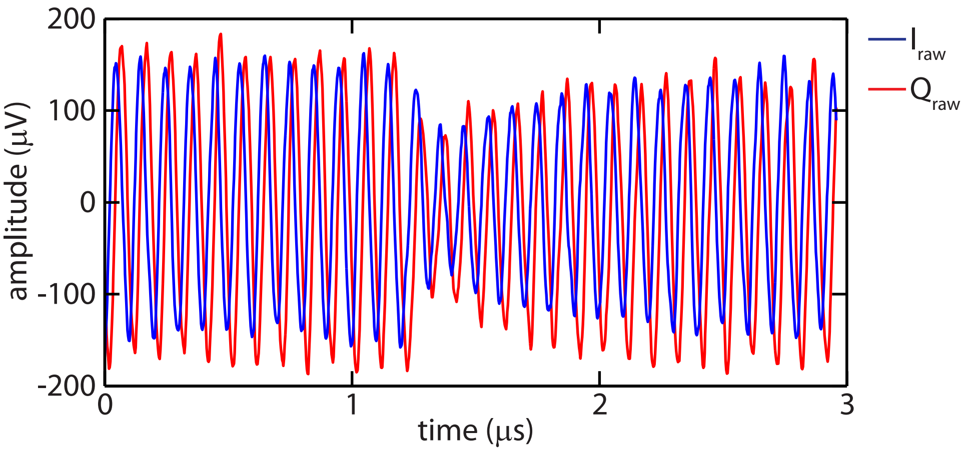

Figure 2.10: $2.3 \cdot 10^7$ averages over the uncorrected, down-converted I and Q traces recorded by the A/D-converter. At approx. 1.2 µs, the response of the resonator probe tone to a π-pulse sent to the qubit is observed. For this measurement, $\omega_{\mathrm{IF}}/2\pi = 10\,\mathrm{MHz}$ is chosen.

as described in Sec.2.2.1.1. The corrected, but not digitally homodyned, down-converted probe tone signal is shown in Fig. 2.11 in comparison to the ideal sinusoidal probe tone signal one would expect if the qubit would be left in the ground state. For the data shown in the figure, the ideal probe tone signal is determined by making a sinusoidal fit to the measured transmitted probe tone signal in the time span prior to the qubit excitation pulse. As compared to the ideal signal, the measured signal deviates both in phase and amplitude from the unperturbed probe tone, indicating that a change of the qubit state changes the resonator transmission properties as discussed in Sec. 2.1.3. Due to its finite coherence time, the qubit will decay to the ground state. The probability of qubit relaxation increases with time. This can be seen from the convergence of the measured probe tone towards the ideal probe tone for $t > 1.3\,\mu s$.

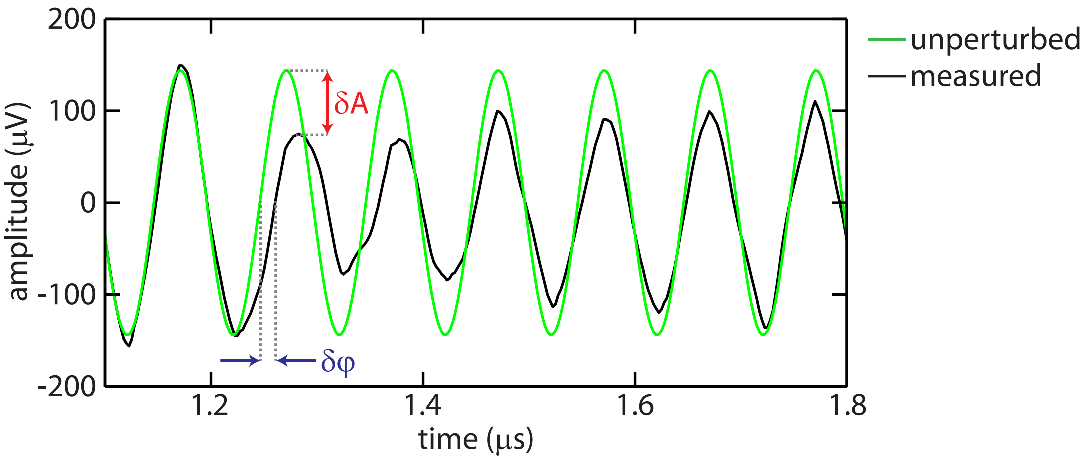

Figure 2.11: Green line: Ideal, unperturbed probe tone one would expect without qubit state change. The green line is obtained by a sinusoidal fit to the measured probe tone between $t = 0\,\mu s$ and $t = 1\,\mu s$, i.e. before the qubit excitation pulse. Black line: Down-converted measured probe tone after amplitude and phase correction. When the qubit is excited, the measured probe tone deviates in amplitude and phase from the ideal, unperturbed probe tone.

In order to make the deviation in amplitude and phase better visible, digital homodyning is performed on the measured probe tone data as discussed in Sec. 2.2.1.1. The resulting time dependent amplitude and phase are shown in Fig. 2.12. For times prior to the qubit excitation pulse, amplitude and phase are at an almost constant value. When the qubit is excited, amplitude and phase change. When the qubit relaxes back to the ground state, also amplitude and phase converge towards the original values before the pulse. As discussed in Sec. 2.1.3, the phase information may be more precise than the amplitude information. We therefore infer the relaxation time of the qubit from the time-dependent phase as indicated in Fig. 2.12. In Sec. 3.3, we provide a detailed analysis of the qubit relaxation times inferred from such measurements performed for different pulse durations and amplitudes.

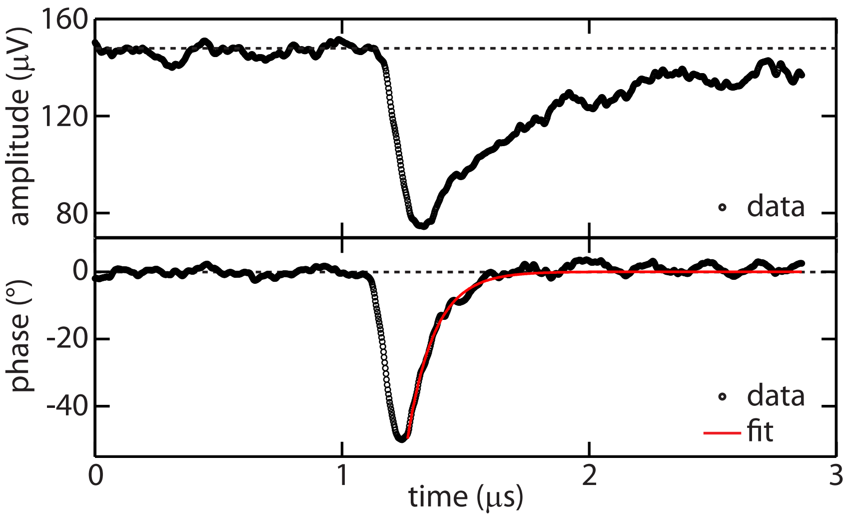

Figure 2.12: Amplitude and phase inferred from digitally homodyning the corrected probe tone signal. The effect of the π-pulse applied to the qubit is clearly visible. As described in the main text, the energy relaxation rate of the qubit is inferred from the phase information (red line). Dashed black lines: Amplitude and phase of the unperturbed probe tone.

Chapter 3

Circuit QED with a flux qubit

Over the last decade, the circuit quantum electrodynamics (QED) architecture has become a well-established platform for the investigation of light-matter-interaction [37, 38], quantum information processing [26, 27, 29, 127] and fundamental quantum mechanics [36, 128–130]. However, a successful implementation of these applications make high demands on the coherence times of the various circuit QED components such as quantum bits or resonators. In order to be able to fulfill these requirements, measurement techniques allowing to determine coherence properties of qubits and resonators have to be developed. These measurement techniques also represent the fundamental prerequisite for a controlled optimization of coherence times. Another key advantage of the circuit QED architecture is that coupling strengths between qubits and resonators can be designed to the desired value over several orders of magnitude [37]. In order to be able to match the required coupling strength for a specific application, a profound understanding of the coupling mechanisms between the circuit QED building blocks is essential.

The flux qubit sample discussed in this section is comprised of a persistent current flux qubit coupled galvanically to the signal line of a transmission line resonator. Inserting a coupling Josephson junction in the shared arm between qubit and resonator signal line in the spirit of Ref. [37] serves the purpose of getting deeper insight into galvanically coupled qubit-resonator systems and the corresponding coupling strengths. Furthermore, our sample is used to set up and put into operation the measurement technique for time domain measurements.

3.1 Single resonator sample layout

The flux qubit sample, fabricated by M. Häberlein, consists of a coplanar waveguide resonator coupled galvanically to a flux quantum bit. The latter is placed at one of the current antinodes of the third harmonic mode of the resonator. In this way, the qubit couples inductively to the three lowest resonator modes as the currents corresponding to these modes are nonzero at the qubit position, see Fig. 3.1. An antenna, also designed as coplanar waveguide, can be used to apply drive or excitation microwave signals to the qubit. The sample layout is shown in Figs. 3.2(a)-3.2(e). The coplanar waveguide resonator and the antenna are fabricated in Nb technology on a thermally oxidized Si substrate. The flux qubit is comprised of a superconducting Al loop intersected by three Josephson junctions where one of the junctions is smaller by a factor $\alpha \approx 0.7$. The Al/AlO$_x$/Al Josephson junctions are produced using shadow evaporation. For details on the fabrication process we refer to Refs. [52, 97, 131].

A fourth Josephson junction is placed in the branch shared by the flux qubit loop and the resonator signal line. This is done in the spirit of Refs. [37, 51, 52] where the inductance of the Josephson junction contributes to the mutual inductance between resonator and qubit. In doing so, the regime of ultrastrong coupling can be reached and a relative qubit-resonator coupling strength as high as 12 % of the respective resonator mode frequency has been achieved with a coupling junction seven times larger than a regular qubit junction. In our sample, the coupling junction, here and in what follows denoted as the *β-junction*, is designed to the same size as a regular Josephson junction.

A schematic drawing of the sample and the measurement principle is provided in Fig. 3.2(f). All measurements discussed in this chapter are based on measuring transmission through the resonator with and without applying drive or excitation signals to the qubit using the on-chip antenna. The magnetic flux threading the qubit loop can be tuned by means of a superconducting coil mounted in the vicinity of the sample. For a detailed description of the measurement setup, we refer to Sec. 2.1.1.1.

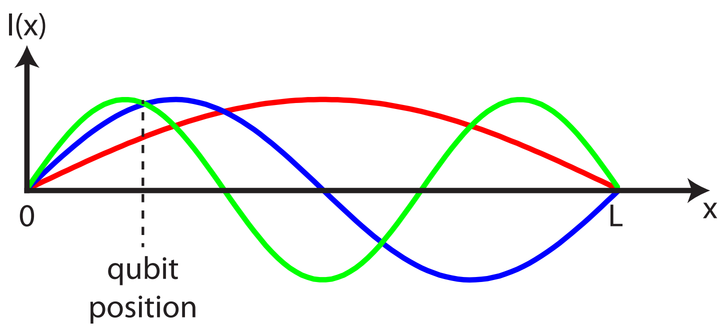

Figure 3.1: Current distribution of the three lowest resonant modes in a half-wavelength resonator of length L. Placing the qubit at one of the current antinodes of the third harmonic allows to couple the qubit to the three lowest resonant modes. Red: First harmonic. Blue: Second harmonic. Green: Third harmonic.

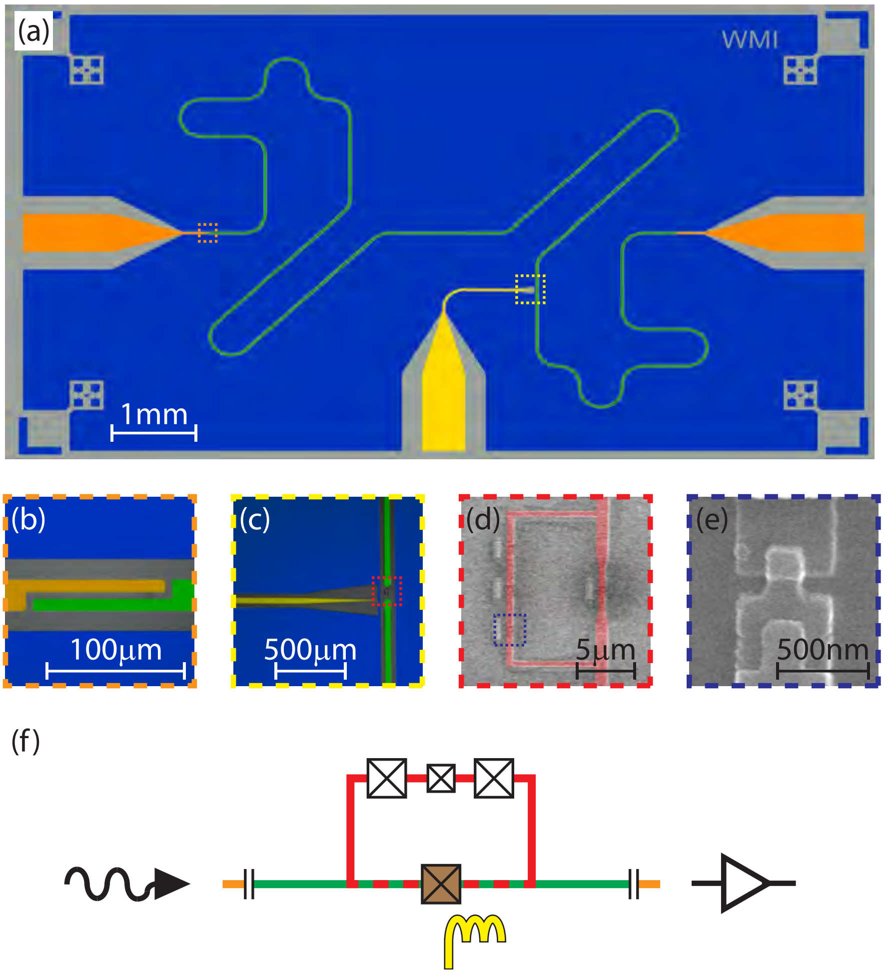

Figure 3.2: (a) Layout of the flux qubit sample. Nb ground planes are shown in blue, feed lines in orange, the signal line in green and the antenna in yellow. (b) Coupling capacitor defining the resonator. (c) Antenna (yellow) in CPW geometry. (d) SEM image of the flux qubit (red) coupled galvanically to the signal line of the resonator. (e) SEM image of a regular Josephson junction. (f) Schematic of the sample layout. A three Josephson junction flux qubit (red) is coupled galvanically to the signal line of the resonator (green). To enhance the coupling, an additional Josephson junction (brown) is placed in the shared arm between qubit and resonator (green/red dashed). Excitation signals can be applied to the qubit by means of the antenna (yellow).

3.2 Continuous wave spectroscopy

For a first characterization of our sample, we perform continuous-wave transmission spectroscopy. These measurements allow us to determine the resonator mode frequencies and the flux-dependent qubit transition frequency. The measurement setup used for this purpose is discussed in Sec. 2.1.1.1.

3.2.1 High-power continuous-wave spectroscopy

We measure transmission through the resonator with the qubit kept in the ground state as a function of the magnetic flux applied to the qubit loop. We note that the measurements presented in this section are limited by a damaged HEMT amplifier [cf. Fig. 2.2] worsening the signal-to-noise ratio of the transmitted signal. Using a vector network analyzer, we first measure the transmission spectra of the first three resonator modes at slightly increased powers corresponding to approx. 2 poa calibrated for the third harmonic, cf. Sec. 3.2.3. The results are shown in Fig. 3.3. Pronounced avoided crossings are observed for the third and second harmonics and also, less pronounced, for the first harmonic. Far away from the degeneracy point $\delta\Phi_{\mathrm{ext}} = \Phi_{\mathrm{ext}} - \Phi_0/2 = 0$, the bare resonant mode frequencies are obtained. Analyzing the linewidths allows to extract the quality factors of the respective modes. However, the first mode is located outside the amplifier bandwidth which leads to a significantly reduced signal-to-noise ratio of less than 3 dB, making it impossible to determine the quality factor. For the second harmonic, we find a decay rate of $\kappa_2/2\pi = 1.3\,\mathrm{MHz}$, corresponding to a quality factor of $Q_2 = 4.1 \times 10^3$. For the third harmonic, we find $\kappa_3/2\pi = 0.8\,\mathrm{MHz}$ and $Q_3 = 8.5 \times 10^3$.

3.2.2 Two-tone spectroscopy

In order to get access to the qubit energy gap Δ and the persistent current I_{p}, we perform two-tone spectroscopy as described in Sec. 2.1.3. The spectroscopy tone is applied to the qubit via the on-chip antenna, cf. Fig. 3.2. We choose the dispersively shifted frequency of the third harmonic as the flux-dependent probe tone frequency. In order to ensure negligible shifts of the qubit transition frequency due to the mean resonator photon population, the probe tone power is set to approx. 0.3 poa. The probe tone transmission is shown in Fig. 3.4 as a function of the spectroscopy tone frequency and the magnetic flux applied to the qubit. As expected, transmission is maximum if the qubit is in the ground state. If the qubit is saturated by the spectroscopy tone, the mode frequency is shifted and decreased transmission is observed. Since the qubit energy gap appears to be close to the second harmonic mode frequency, an anticrossing between the latter and the qubit hyperbola is observed, corresponding to the dressed states $|+,1\rangle_2$ and $|-,1\rangle_2$, cf. Sec. 1.4.2. The subscript denotes the resonator's second harmonic. When the flux is tuned away from the degeneracy point, the qubit is far detuned from the second harmonic and the dressed states can be approximated as $|+,1\rangle_2 \approx |e,0\rangle_2$ and $|-,1\rangle_2 \approx |g,1\rangle_2$, cf. Fig. 3.4. This leads to decreasing spectroscopic response for the latter since the two-tone spectroscopy protocol is insensitive to states where the qubit is in the ground state.

We note that in the resonant regime it is impossible to read the qubit energy gap

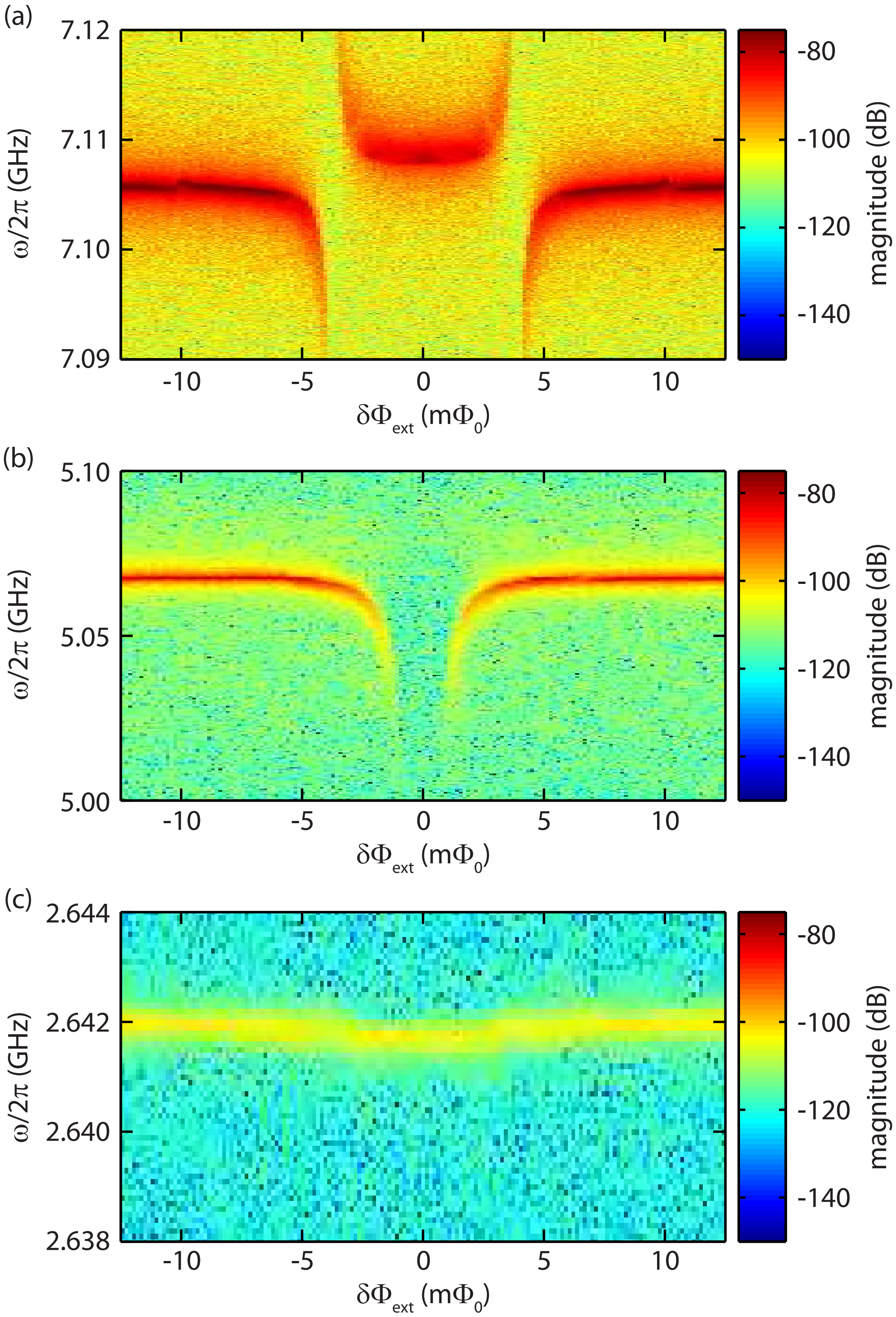

Figure 3.3: Single-tone spectroscopy of the first three harmonics of the resonator. Large input powers allow to clearly resolve the mode spectrum despite the damaged HEMT amplifier. (a) Third harmonic. The power calibration was performed for this mode and yields a resonator population of 2 poa, cf. Sec. 3.2.3. (b) Second harmonic. (c) First harmonic. This mode is located outside of the amplifier bandwidth which limits the signal-to-noise ratio.

directly from the spectroscopy data. However, as will be shown in Sec. 3.2.4, the combination of the two-tone spectroscopy data and single-tone continuous-wave spectroscopy data allows to extract the qubit parameters from a fit of the Hamiltonian to the data. For this purpose, first the mean photon number in the resonator has to be calibrated.

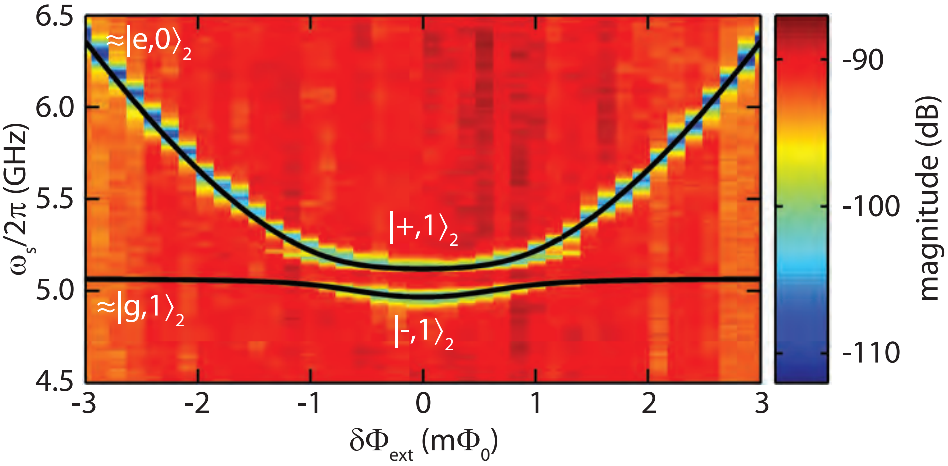

Figure 3.4: Two-tone spectroscopy of the qubit. Shown is the probe tone transmission as a function of the spectroscopy tone frequency ω_s and the magnetic flux. An anticrossing is observed between the second harmonic and the qubit hyperbola, resolving the dressed states $|\pm,1\rangle_2$ where the subscript denotes the second harmonic. Black lines: Fit to the Hamiltonian of Eq. (3.3).

3.2.3 Power calibration

Power calibration can be performed straightforwardly as described in Sec. 2.1.4 only if the qubit is dispersive with respect to all resonant modes. In our situation, the detuning between the qubit and the second harmonic at the degeneracy point is of the same order of magnitude as the qubit-mode coupling. Hence, one could perform power calibration away from the degeneracy point, however, this would be done at the cost of high sensitivity to fluctuations of the magnetic flux which shift the qubit transition frequency. Since power calibration is very sensitive to variations of the qubit frequency, it is advantageous to perform such measurements at the degeneracy point where the qubit hyperbola is flat and small flux deviations do not change the qubit transition frequency.

Our measurement data obtained in order to perform the power calibration are shown in Fig. 3.5(a). We perform two-tone spectroscopy with the flux set to $\delta\Phi_{\mathrm{ext}} = 0$ for probe tone powers ranging from $-25\,\mathrm{dBm}$ to $5\,\mathrm{dBm}$ (referenced to the VNA output). To take into account the fact that the qubit is not dispersive with respect to the second harmonic at frequency ω_2, we make a more general approach [126] to calibrate the average number of photons in the third harmonic, which is the mode used to read out the qubit. Following

Eq. (1.99), the bare qubit transition frequency ω_{Q} is shifted by the number of photons n_3 to

$$\tilde{\omega}_{\mathrm{Q}} = \omega_{\mathrm{Q}} + \frac{g_3^2}{\delta\omega_3}(2n_3+1) = \omega_{\mathrm{Q}} + \chi_3(2n+1) \tag{3.1}$$

in which the detuning $\delta\omega_3$ is approximated as $\delta\omega_3 = \omega_{\mathrm{Q}} - \omega_3 \approx \Delta - \omega_3$. This is justified since the dispersive shift per photon $\chi_3 \ll \delta\omega_3$. We then describe the coupling of the qubit to the second harmonic by the Hamiltonian

$$\hat{H}_{\mathrm{cal}} = \hbar \begin{pmatrix} \omega_2 & g_2 \\ g_2 & \tilde{\omega}_{\mathrm{Q}} \end{pmatrix}, \tag{3.2}$$

where g_2 denotes the coupling of the second harmonic to the qubit. Calculating the eigenenergies of the Hamiltonian of Eq. (3.2) yields the frequencies $\lambda_\pm$ of the two eigenstates corresponding to the dressed states $|\pm,1\rangle_2$ depending on the mean photon number n_3, see Fig. 3.5(b). For low powers, $n_3 \approx 0$ and the separation between the two eigenstates is given by $2g_2 \approx 2 \times 87\,\mathrm{MHz}$. We further take into account that the mean photon number n_3 is proportional to the (linear) output power of the VNA. This allows to gauge the mean number of photons n_3 using the frequencies of the two eigenstates, cf. Fig. 3.5(b). We find that a VNA output power of $-14\,\mathrm{dBm}$ results in a mean population of the third harmonic of approx. 1 poa.

3.2.4 Low-power continuous-wave spectroscopy

After power calibration, spectroscopic transmission measurements are performed for all three modes with negligible mean resonator population. To this end, the VNA output power is set corresponding to $n_3 \approx 0.2$ poa. The results are shown in Fig. 3.6. For the first harmonic, the phase of the transmitted signal is shown due to its better contrast instead of the magnitude, owing to the fact that this mode is located outside the amplifier bandwidth which worsens the signal-to-noise ratio. In order to get access to the qubit and resonator frequencies, we fit both the spectroscopy data and two-tone data shown in Fig. 3.4 to the Hamiltonian taking the coupling of the qubit to the three lowest modes into account. Following Eq. (1.100), the Hamiltonian reads

$$\hat{H} = \frac{\epsilon}{2}\hat{\sigma}_z + \frac{\Delta}{2}\hat{\sigma}_x + \sum_{n=1}^{3}\left[\hbar\omega_n\left(\hat{a}_n^\dagger\hat{a}_n + \frac{1}{2}\right) + \hbar g_n\hat{\sigma}_z(\hat{a}_n^\dagger + \hat{a}_n)\right]. \tag{3.3}$$

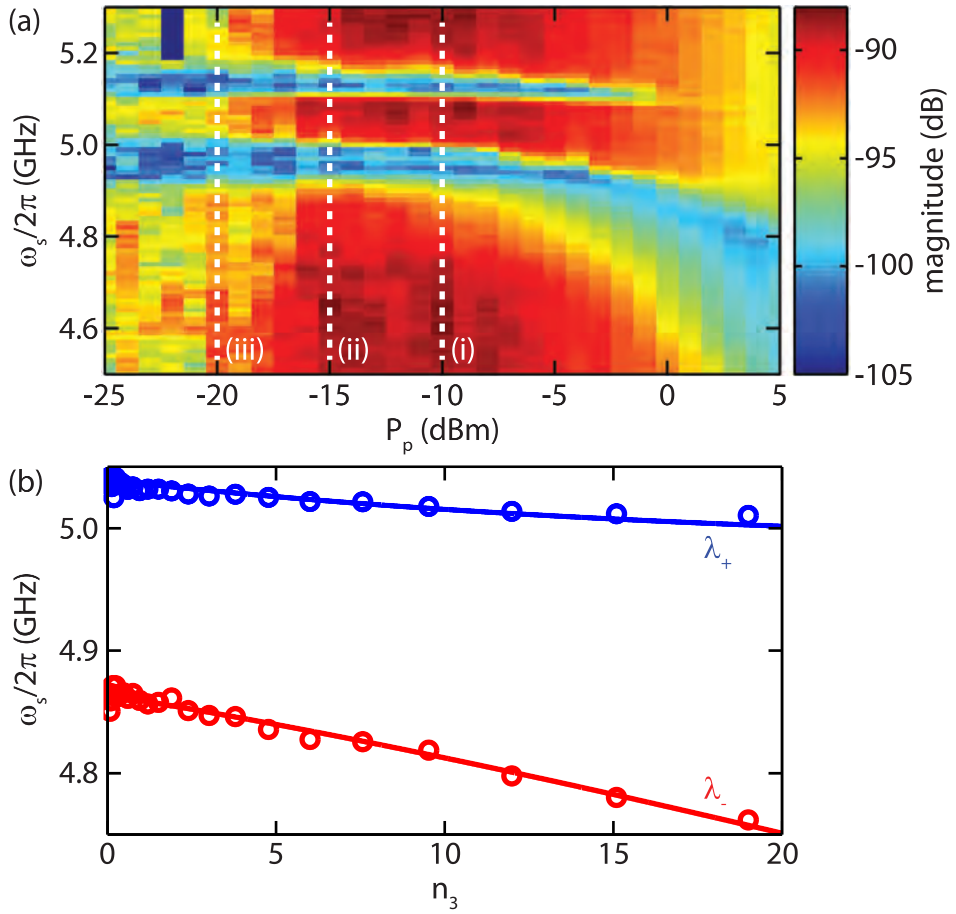

Figure 3.5: Power calibration for the flux qubit sample. (a) Two-tone spectroscopy at the degeneracy point performed for VNA output powers ranging over three orders of magnitude. Two dips, corresponding to the dressed states $|\pm,1\rangle_2$, are observed with frequencies depending on the probe tone power. White dashed lines correspond to the powers at which (i) high-power spectroscopy ($n_3 \approx 2$ poa, Fig. 3.3), (ii) two-tone spectroscopy ($n_3 \approx 0.6$ poa, Fig. 3.4) and (iii) low-power spectroscopy ($n_3 \approx 0.2$ poa, Fig. 3.6) are recorded. (b) Frequencies of the two eigenstates as a function of the mean photon number. Blue and red lines: Eigenvalues of the Hamiltonian of Eq. (3.2). Blue and red circles: Measured mode frequencies taken from (a), scaled to best fit the theoretical model. The scaling factor determines the relation between VNA output power and mean photon number n_3.

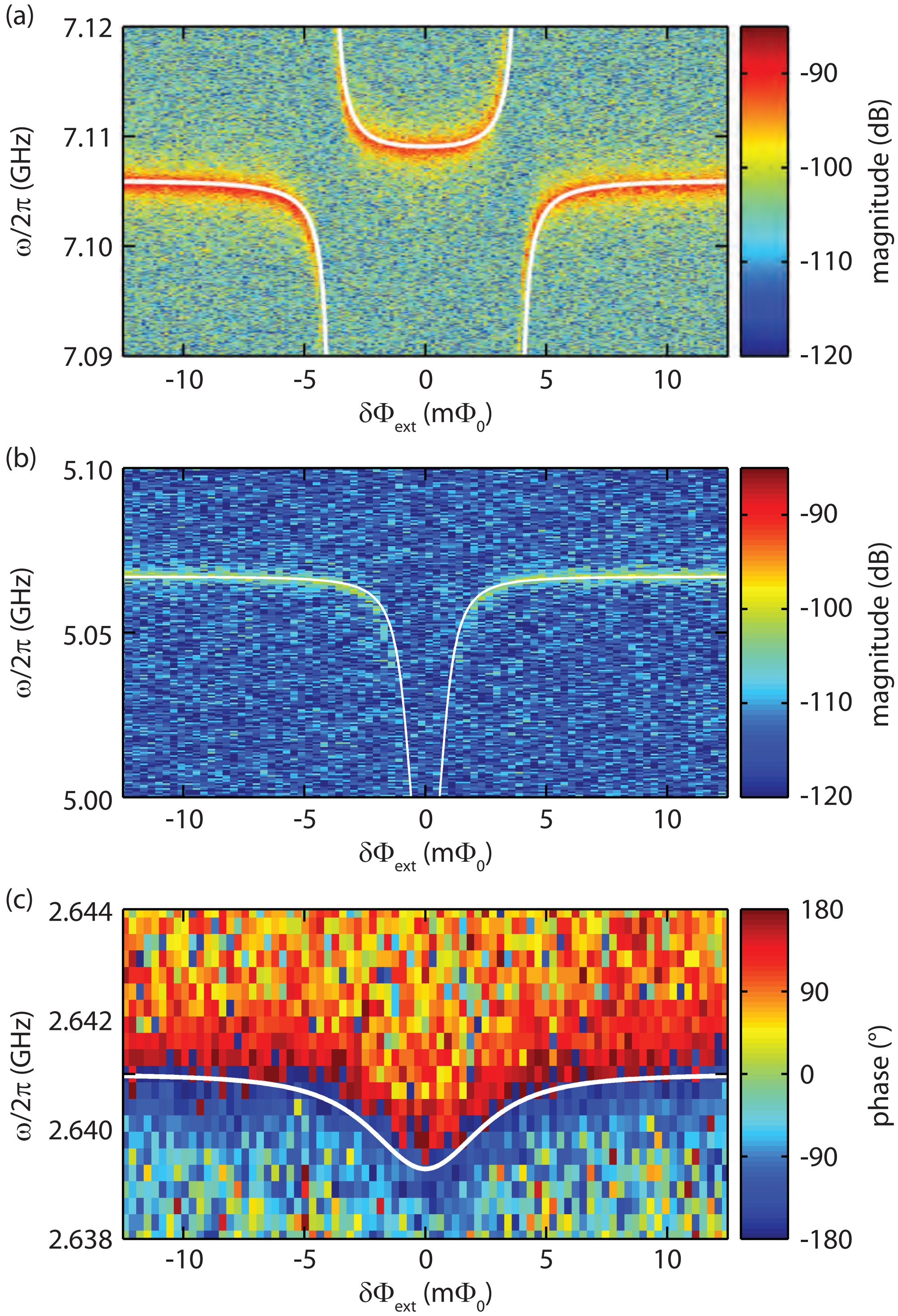

Figure 3.6: Low-power single-tone spectroscopy of the first three resonant modes. (a) Third harmonic. (b) Second harmonic. (c) The first harmonic is located outside the amplifier bandwidth, leading to a reduced signal-to-noise ratio. Therefore, the phase is shown for this mode instead of the magnitude. White lines: Fit to the Hamiltonian of Eq. (3.3).

From the fit, we get the following set of parameters:

$$\begin{aligned} \Delta/h &= 5.02\,\text{GHz}, & I_\text{p} &= 208\,\text{nA} \\ \omega_1/2\pi &= 2.642\,\text{GHz}, & g_1/2\pi &= 32\,\text{MHz} \\ \omega_2/2\pi &= 5.067\,\text{GHz}, & g_2/2\pi &= 72\,\text{MHz} \\ \omega_3/2\pi &= 7.106\,\text{GHz}, & g_3/2\pi &= 88\,\text{MHz} \end{aligned}$$

With relative coupling strengths $g_n/\omega_n \approx 0.01$, the interaction between qubit and resonator is far from the regime of ultrastrong coupling. Actually, the observed relative coupling strengths are on the same order of magnitude as the ones presented in Refs. [52, 132], where an identical flux qubit is coupled galvanically to the signal line of a coplanar waveguide resonator, but without an additional coupling Josephson junction. To qualitatively understand this behaviour, we consider the distribution of the resonator transport current to the qubit branch containing the three qubit Josephson junctions and to the shared branch between qubit and resonator signal line containing the β-junction, cf. Fig. 3.7. We assume that the inductance of the Al lines composing the qubit is negligible compared to the inductances of the Josephson junctions [52]. Following Kirchhoff's law, the res-

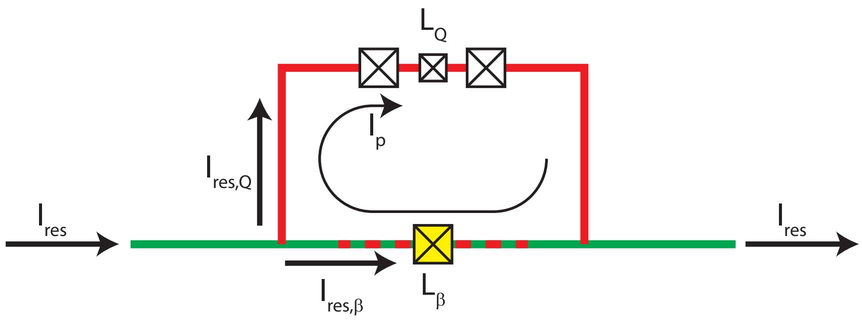

Figure 3.7: A coupling junction (yellow) with large inductance L_β is placed in the shared arm between qubit and resonator, causing the resonator mode current I_res to distribute among the qubit arm containing the three qubit junctions and the shared arm between qubit and resonator. Since the qubit persistent current has different sign with respect to $I_\text{res,Q}$ and $I_{\text{res},\beta}$, respectively, a β-junction with large inductance $L_\beta \approx L_Q$ results in comparably low qubit-resonator coupling strengths.

onator mode current $I_\text{res} = \omega_n\sqrt{\hbar/Z}$, where ω_n is the mode frequency and $Z = 50\,\Omega$ is the impedance, will distribute between the qubit branch containing the three qubit junctions with a total inductance of L_Q and the shared branch between qubit and resonator, see Fig. 3.7. For the case of a large β-junction [37], i.e. $L_\text{Q} \gg L_\beta$, the fraction of the resonator mode current flowing across L_Q will be negligible and the qubit-mode coupling strength g_n can be calculated via $\hbar g_n = L_\beta I_\text{p} I_\text{res}$ with the qubit persistent current I_p.
In our scenario, however, $\beta = 1$ and therefore the fraction of the resonator mode current flowing across L_Q is estimated to $I_\text{res,Q} = I_{\text{res},\beta} L_\beta / L_\text{Q}$ and can no longer be neglected.

In this scenario we can only make a qualitative statement about the expected coupling strength since the Josephson inductance is hard to compute due to its proportionality to $1/\cos\varphi$, cf. Eq. (1.50). Since the persistent current has a different sign when flowing across L_β and L_Q, respectively, the total qubit-mode coupling is given by

$$\hbar g_n = L_\beta I_\mathrm{p} I_{\mathrm{res},\beta} - L_\mathrm{Q} I_\mathrm{p} I_{\mathrm{res,Q}} \ll L_\beta I_\mathrm{p} I_\mathrm{res}. \tag{3.4}$$

Apparently, the regime of ultrastrong coupling cannot be reached with the configuration of this particular sample. We note that a very critical reader could argue that the β-junction could be short-connected due to a fabrication problem and therefore $L_\beta = 0$. However, as can be seen in Fig. 3.6, the spacing between the resonator modes is not uniform. Specifically, $\omega_2 \neq 2\omega_1$ and $\omega_3 \neq 3\omega_1$. This observation is in agreement with Ref. [37], where the mode spacing is also not uniform due to the presence of the β-junction. In turn, data presented in Refs. [52, 132] where an identical flux qubit is coupled galvanically to a similar resonator, but without a β-junction, show an almost perfectly uniform mode spacing. Furthermore, warming up our sample and cooling it down again caused all Josephson junctions to be short-connected. In this situation we also find evenly spaced resonator modes at $\omega_1^*/2\pi = 2.29\,\mathrm{GHz}$, $\omega_2^*/2\pi = 4.58\,\mathrm{GHz}$ and $\omega_3^*/2\pi = 6.90\,\mathrm{GHz}$. This also supports our assumption that a short-connected β-junction can not be blamed for the observed low relative coupling strengths.

Even though it has been shown that inserting a Josephson junction in the shared branch between qubit and resonator can enhance the coupling significantly [37], our findings on the sample investigated in the course of this thesis indicate that a coupling Josephson junction does not allow to reach arbitrarily large coupling strengths by increasing the Josephson inductance of this coupling junction. Since this scenario is hard to analyze theoretically, we propose to find the maximum coupling which can be reached with such a coupling junction by measuring a series of qubits coupled to resonators for a set of different coupling junction sizes. We are convinced that such a systematic study will in turn provide a basis for further theoretical studies of the influence of coupling junctions on the qubit-resonator coupling strength.

3.3 Driven Rabi oscillations

In this section we aim at characterizing the coupled qubit-resonator system in the time domain. To this end, we run the protocol allowing to observe driven Rabi oscillations as discussed in Sec. 2.2. We note that also the time-domain measurements are affected by the damaged cryogenic HEMT amplifier. However, the primary goal of putting into operation and testing the time-domain measurement setup could be reached despite this technical problem. In order to not being affected by flux instabilities, we first perform measurements at the degeneracy point $\delta\Phi_{\rm ext} = 0$. Excitation pulses are applied to the qubit using the on-chip antenna (cf. Fig. 3.2). At the degeneracy point, the qubit is not dispersive with respect to the second harmonic as shown in Fig. 3.4. We apply drive pulses of length τ at the frequency of the $|-,1\rangle_2$-state given by $\omega_{\rm s}/2\pi = 4.960\,\mathrm{GHz}$.

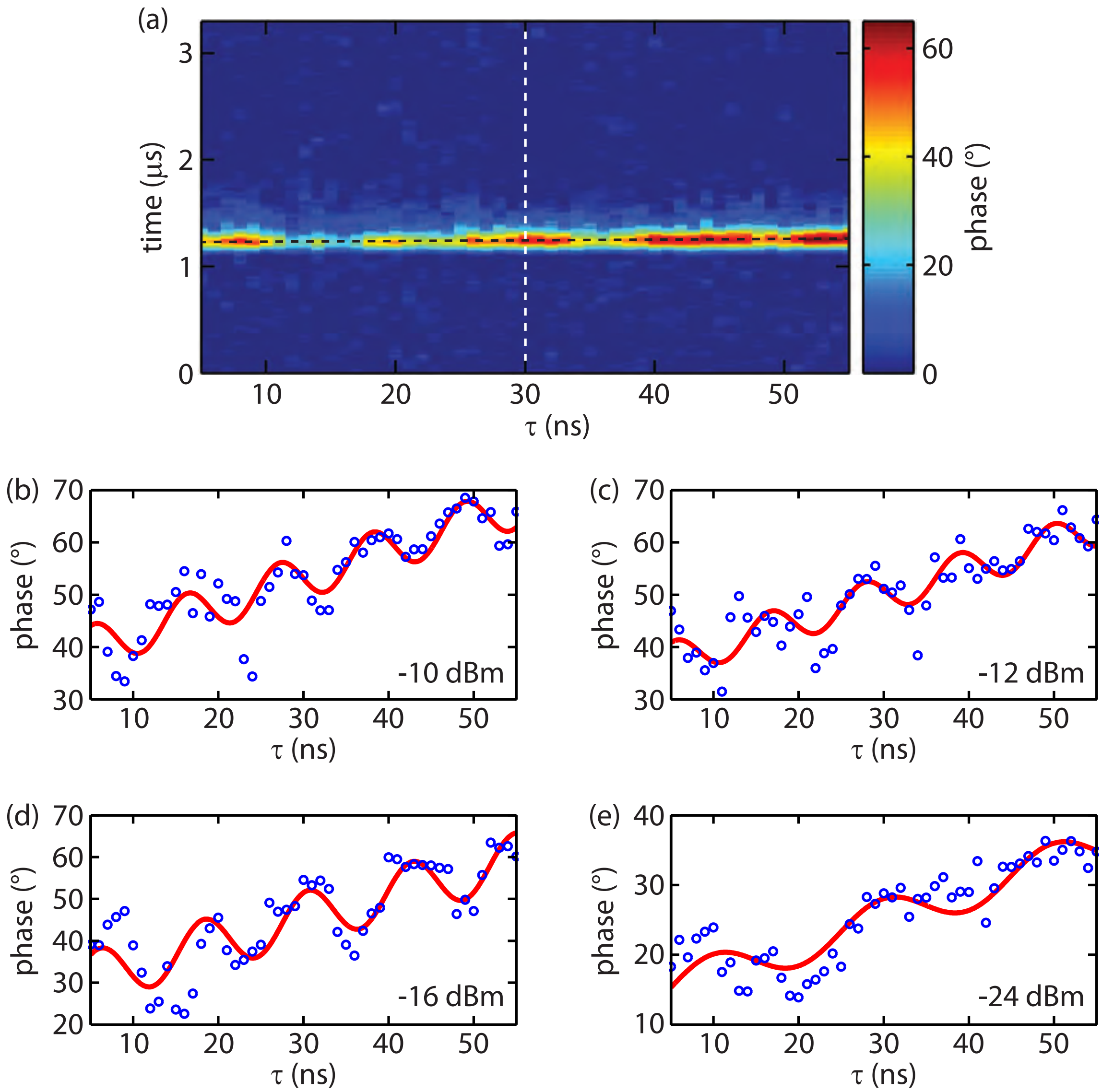

Figure 3.8: Driven Rabi oscillations measured at the degeneracy point. (a) Probe tone phase as a function of time and pulse length measured for an excitation pulse power of $-16\,\mathrm{dBm}$ (referenced to the signal generator output). Black dashed line: Points in time coinciding with the falling edge of the excitation pulse. White dashed line: Pulse length identified with maximum probability to prepare the qubit in the excited state. (b)-(e) Blue circles: Phase of the probe tone measured at the point in time coinciding with the falling edge of the excitation pulse. Red lines: Sinusoidal fits overlain by linear trend.

The qubit state is read out using a continuous-wave probe signal at the frequency of the dispersively shifted third harmonic at $\omega_\mathrm{p}/2\pi = 7.109\,\mathrm{GHz}$. The power of the latter is chosen such that the third harmonic is populated with approx. one photon on average. The transmitted probe signal is recorded in a time-resolved way using the setup and the error correction protocol presented in Sec. 2.2.1.1. For all pulse lengths τ, we average over 2.3×10^7 traces. Figure 3.8(a) shows the phase of the transmitted probe tone as a function of time and pulse length for $5\,\mathrm{ns} \leq \tau \leq 55\,\mathrm{ns}$. An oscillatory dependence of the phase response on the pulse length is observed as expected. To make the oscillatory behaviour better visible, we show the phase response at the time coinciding with the falling edge of the qubit excitation pulse as a function of pulse length measured for four different pulse amplitudes in Figs. 3.8(b)-(e). As can be seen, the expected oscillatory behaviour, identified with Rabi oscillations, is overlain by a linear trend of unknown origin.

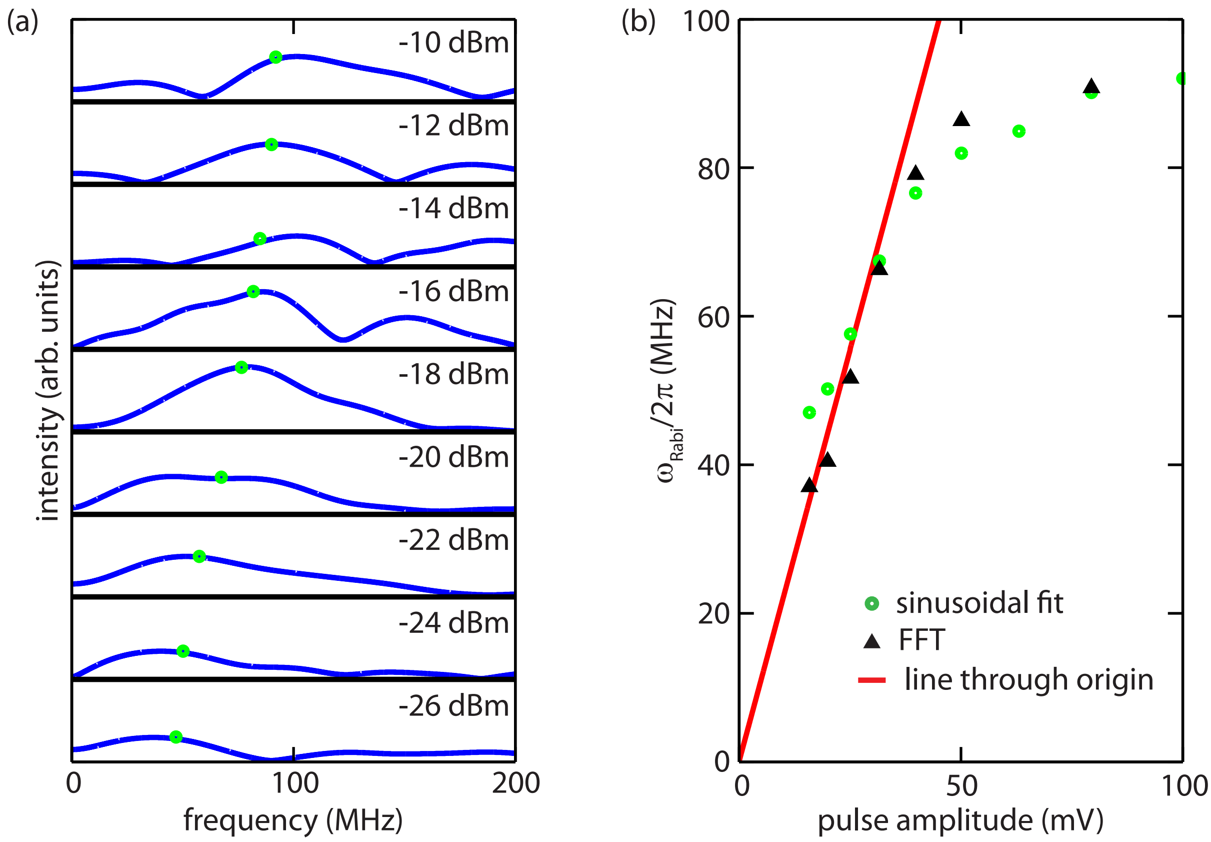

Figure 3.9: (a) Blue lines: Fast Fourier transforms of the probe tone phase (cf. Fig.3.8) measured for different excitation pulse powers (referenced to the signal generator output). Green circles: Frequency determined by a sinusoidal fit to the probe tone phase as a function of pulse length. The latter agree well with the results obtained by an FFT. (b) Rabi frequency as a function of pulse amplitude. Below approx. 50 mV (referenced to the signal generator output), the Rabi frequency follows the expected proportionality to the drive pulse amplitude.

An unambiguous characteristic of driven Rabi oscillations is the proportionality between the Rabi frequency and the pulse power, cf. Sec. 2.2.2. In order to verify the proportionality, we calculate the fast Fourier transforms (FFT) of the phase-time curves for nine different pulse amplitude. The results are shown in Fig. 3.9(a). As can be seen, the FFT maxima coincide well with the frequencies extracted from sinusoidal fits as shown in Figs. 3.8. In Fig. 3.9, we plot the power-dependent Rabi frequencies extracted from sinusoidal fits and from the FFT analysis versus the pulse amplitude. Fig. 3.9(b) shows that the dependence of the Rabi frequency on the pulse amplitude obeys the expected proportionality up to a pulse amplitude of approx. 50 mV (referenced to the signal generator output). For larger drive amplitudes, the Rabi frequency seems to saturate to a value coinciding with the coupling strength g_3. Such a phenomenon where the Rabi frequency converges towards characteristic system frequencies has also been observed in Ref. [19], but in a frequency range two orders of magnitude larger than in our case.

Next, we analyze the qubit energy relaxation time T_1. To this end, we again consider Fig. 3.8(a). We identify a pulse length of 30 ns with a $(2n-1)\pi$-pulse ($n \in \mathbb{N}$), i.e. we assume that the qubit is in the excited state after the pulse has been applied. We then consider the exponential decay of the phase as a function of time, cf. Fig. 3.10. From an exponential fit to the data, we find a decay time $T_{\mathrm{decay}} \approx 1.0 \times 10^2$ ns. However, in our situation we are not observing the decay of a pure qubit state, but a dressed state also containing a resonator contribution. To extract the qubit energy relaxation time T_1, we make the ansatz

$$T_{\mathrm{decay}}^{-1} = T_1^{-1} + \kappa_2/2\pi, \tag{3.5}$$

where $\kappa_2/2\pi = 1.3$ MHz is the decay rate of the second resonator harmonic. With this, we find a qubit energy relaxation time at the degeneracy point of $T_1 \approx 1.2 \times 10^2$ ns.

Thus far, we have investigated the response of the probe tone to pulses applied to the state $|-,1\rangle_2$ at the degeneracy point. Next, we detune the magnetic flux applied to the qubit away from the degeneracy point to $\delta\Phi_{\mathrm{ext}} \approx 1\,\mathrm{m}\Phi_0$ such that $\omega_{\mathrm{Q}} = 5.34$ GHz. Using the same protocol as above, we again record the phase response of the probe tone transmitted through the resonator at the frequency of the third harmonic as a function of time for different pulse lengths applied to the qubit. The results are shown in Fig. 3.11(a). Again, a pronounced oscillatory behaviour is observed. Plotting the phase response at the point in time coinciding with the falling edge of the qubit excitation pulse versus the pulse length, we find that the data can be well described by an exponentially decaying sinusoidal fit overlain by a linear trend. Also the FFT spectrum shows a clearly pronounced maximum in agreement with the observation of driven Rabi oscillations. Unfortunately,

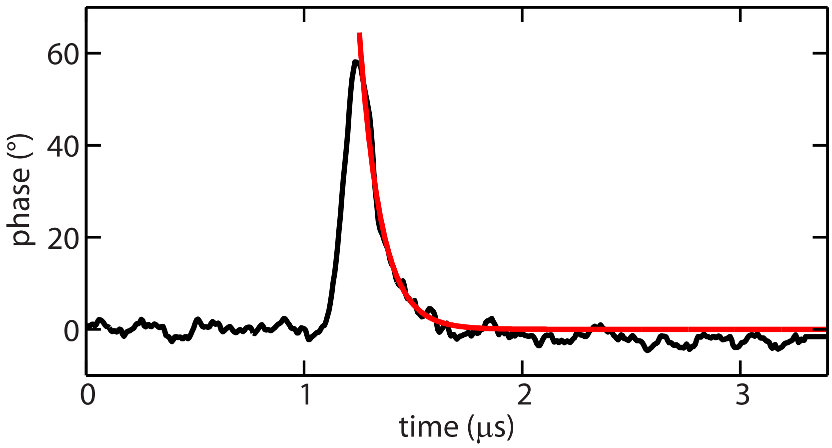

Figure 3.10: Black line: Probe tone phase as a function of time for an excitation pulse with $\tau = 30\,\mathrm{ns}$ and $P_\mathrm{s} = -16\,\mathrm{dBm}$. Red line: Exponential decay allowing to extract the energy relaxation time of $T_1 \approx 115\,\mathrm{ns}$.

instabilities of the magnetic flux[1] made subsequent measurements of the Rabi frequency for different drive pulse amplitudes impossible. Nevertheless, we can extract an estimate for the T_1-time. To this end, we identify a pulse length of $\tau = 24\,\mathrm{ns}$ with maximum probability of preparing the qubit in the excited state. For this pulse length, the phase is shown as function of time in Fig. 3.12. An exponential fit to the data yields an energy relaxation time of $T_1^{1\,\mathrm{m}\Phi_0} \approx 1.1 \times 10^2\,\mathrm{ns}$ which is on the same order as the T_1-time found at the degeneracy point.

In conclusion, we have successfully set up and tested the measurement setup for time-domain spectroscopy measurements. The measurement technique presented here has also been used for the measurements presented in Sec. 4.3.2. Furthermore, our setup also allows to perform time-domain measurements on more complex systems like gradiometric flux qubits with tunable gaps [133]. Furthermore, the sample provides insight into galvanically coupled qubit-resonator systems and suggests a systematic study of the influence of coupling Josephson junctions on the qubit-resonator coupling strengths.

[1] Caused by insufficiently shielded external sources of magnetic fields, e.g. strong magnets in neighbouring labs. Flux variations on the order of $0.1\,\mathrm{m}\Phi_0 - 1\,\mathrm{m}\Phi_0$ per hour were observed.

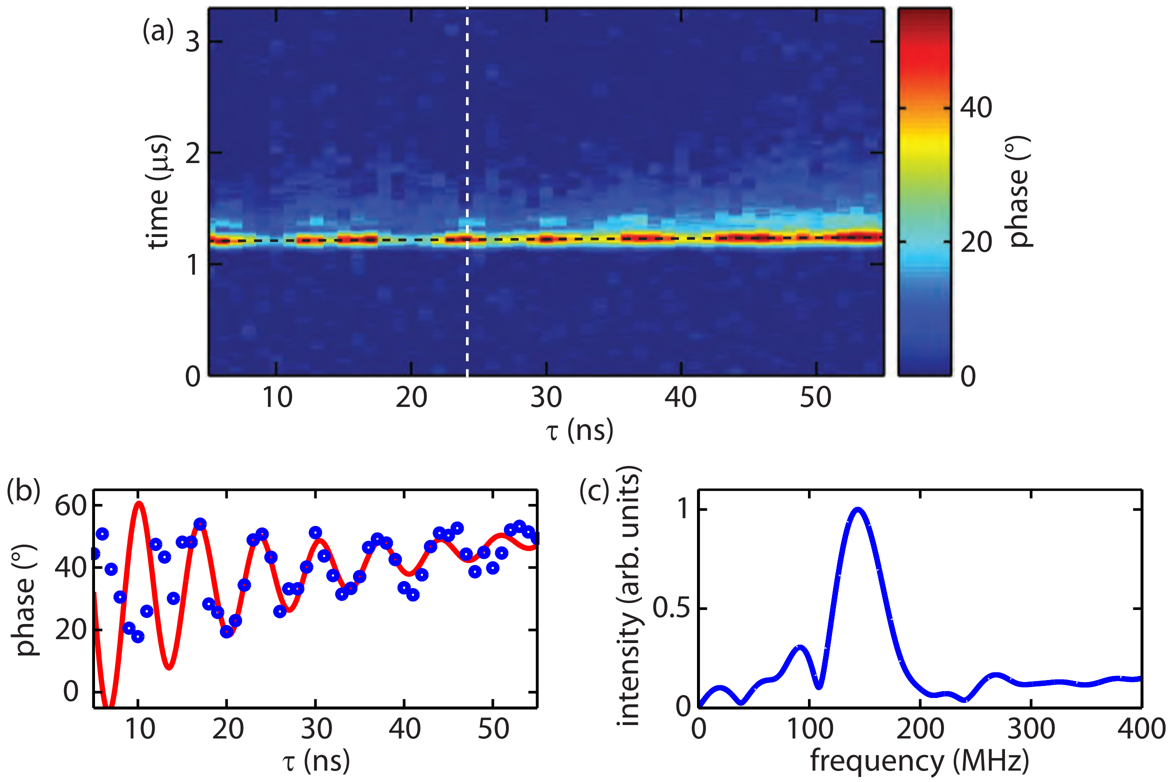

Figure 3.11: Driven Rabi oscillations measured at $\delta\Phi_{\rm ext} \approx 1\,{\rm m}\Phi_0$. (a) Probe tone phase as a function of time and pulse length τ. Black dashed line: Points in time coinciding with the falling edge of the excitation pulse. White dashed line: Pulse length identified with maximum probability to prepare the qubit in the excited state. (b) Blue circles: Phase of the probe tone measured at the point in time coinciding with the falling edge of the excitation pulse. Red lines: Exponentially decaying sinusoidal fit overlain by linear trend. (c) Fast fourier transform of the probe tone phase (as a function of τ). A single pronounced peak is observed.

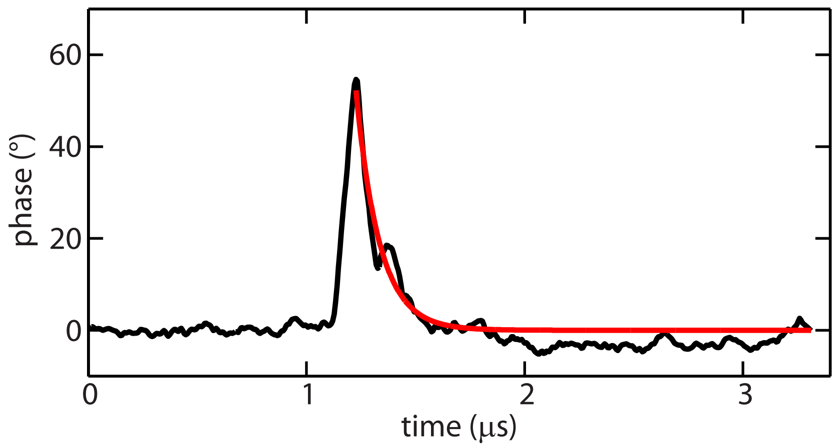

Figure 3.12: Black line: Probe tone phase as a function of time for an excitation pulse with $\tau = 24\,{\rm ns}$ and $P_{\rm s} = -10\,{\rm dBm}$. Red line: Exponential decay allowing to extract the energy relaxation time of $T_1 \approx 1.1 \times 10^2\,{\rm ns}$.

Chapter 4

Two-resonator circuit QED

One of the most important advantages in using superconducting circuits for the investigation of light-matter interaction [37], quantum information processing and, recently, quantum simulation [40, 45, 134] is the large coupling strength between the main building blocks of the circuit QED architecture, namely superconducting quantum bits and microwave resonators. Noticeably, the coupling strength remains considerable even for second-order mechanisms. However, to realize quantum gates and quantum information and simulation protocols, the coupling between the individual circuit elements needs to be tunable *in situ*. This can be realized in at least two ways. One way is to decouple two circuits by detuning them in frequency, for example by using the frequency tunability of superconducting qubits. With this technique, systems with up to nine qubits and up to ten microwave resonators were studied [24, 26, 29, 134], entangled quantum states were created [33, 34, 135] and quantum teleportation [36] and quantum computing protocols were demonstrated [25, 136, 137]. Alternatively, the coupling between two circuit QED building blocks can be mediated by additional coupling circuits. Examples for coupling circuits include single Josephson junctions [27, 55, 138], SQUIDs [53, 54, 56–58, 139] or qubits [140–142] which were used to realize tunable coupling between qubits, resonators and transmission lines. Furthermore, new types of qubits were introduced featuring intrinsic tunability of the coupling to microwave resonators [143–146]. In this chapter, we report on tunable and switchable coupling between two frequency-degenerate superconducting transmission line resonators mediated in a second-order process by a superconducting flux qubit [120, 121]. Our setup is in a way dual to the usage of a resonator as quantum bus between two qubits [147, 148].

After introducing the sample layout, we analyze the complex mode structure by means of transmission spectroscopy. We show that one resonant mode is coupled ultrastrongly to the qubit and present an unambiguous spectroscopic proof for the breakdown of the Jaynes-Cummings approximation. We find that ultrastrong coupling of a qubit to a distributed resonator structure can be reached solely by the geometrical configuration of the latter without making use of additional inductive elements realized for example by Josephson junctions.

Finally, we discuss tunable and switchable coupling between the two resonators. One particular property of our scheme is that the coupling between the two resonators can either be tuned via the magnetic flux applied to the qubit loop or switched by varying the qubit population via a microwave drive. We perform time domain measurements to find the parameter regimes for optimal sample performance. We point out that tunable coupling between frequency-degenerate resonators is of particular importance in the light of recent proposals for quantum simulations of many-body physics [40, 43–45, 48, 49]. All these proposals and experiments would obviously profit from a well-controlled tunable resonator-resonator coupling such as the one presented in this work.

4.1 Two-resonator sample layout

Our sample, designed and fabricated by E. Hoffmann [97], is composed of two coplanar stripline resonators, A and B (cf. Sec. 1.2.2.3), fabricated in Nb technology on a thermally oxidized Si substrate. A superconducting persistent current flux qubit is coupled galvanically to the signal lines of both resonators at the position of the current antinodes of the lowest frequency modes as shown in Fig. 4.1(a)-4.1(e). The flux qubit consists of a superconducting Al loop intersected by three Josephson junctions. Two of them, referred to as regular Josephson junctions, have the critical current I_c. The third one has a junction area smaller by a factor $\alpha \simeq 0.7$. The galvanic coupling of the qubit to the signal lines of both resonators gives reason for using the coplanar stripline architecture instead of the coplanar waveguide architecture. For the latter, one of the resonator ground planes would have to be interrupted around the position of the qubit, cf. Fig. 4.1(c). However, transitions from the CPW to the coplanar stripline (CSL) architecture require elements such as slotline radial stubs or baluns [66] which are both space consuming and nontrivial to design. Furthermore, bonding would be required in close proximity to the qubit. For these reasons, the transition from the CPW architecture, in which the resonator feed lines are fabricated, to the CSL resonator is done at the position of the coupling capacitor, cf. Fig. 4.1(b).

The sample is mounted inside a gold-plated copper box attached to the base temperature stage of a dilution refrigerator stabilized at 45 mK. The magnetic flux Φ_{ext} applied to the qubit can be adjusted by means of a superconducting solenoid mounted on top of the sample box.

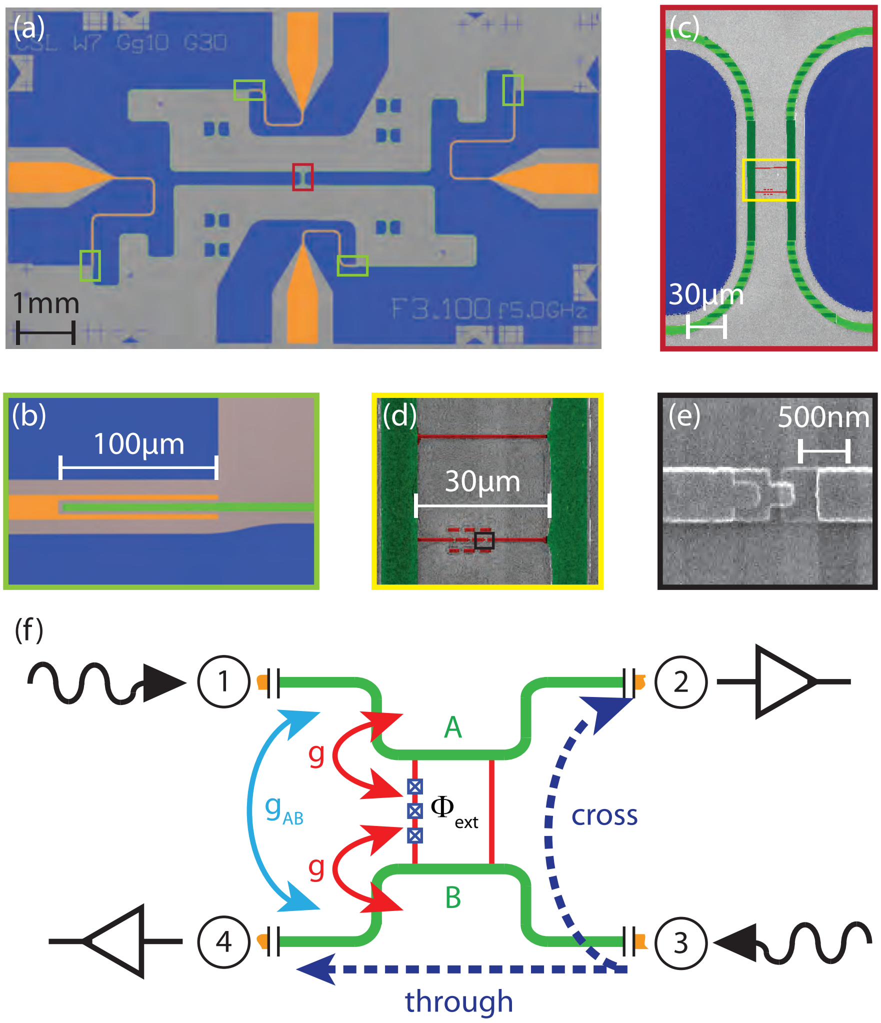

Figure 4.1: Sample and sketch of the coupling mechanisms. (a) False-color image of the sample chip. Nb ground planes are shown in blue and feed lines in orange. The resonator signal lines reside along the ground plane edges. The green and red rectangles mark the areas shown on an enlarged scale in (b) and (c), respectively. (b) Coupling capacitor defining the resonators. (c) Resonator coupling area with signal lines (green) and flux qubit (red). Light/dark green stripes highlight Nb-Al overlap areas. The yellow rectangle marks the area shown in (d). (d) Flux qubit galvanically coupled to both resonators. The black rectangle marks the area shown in (e). (e) $Al/AlO_x/Al$ Josephson junction fabricated using shadow evaporation. (f) Sketch of the coupling mechanisms. The wiggly arrows symbolize the input microwave lines connected to both resonators and the black triangles denote the corresponding output lines featuring microwave amplifiers. The crosses intersecting one qubit branch symbolize the three Josephson junctions. To characterize the mode structure of the sample, we first measure transmission through the two resonators. Encircled numbers denote the port identifiers. Sample images by courtesy of E. Hoffmann [97].

4.2 Ultrastrong coupling in two-resonator circuit QED

One characteristic feature of the circuit QED architecture is the large coupling strength that can be reached between qubits and resonators as a consequence of the large qubit dipole moments of the former and the small mode volumes of the latter. Remarkably, even the regime of ultrastrong coupling can be reached in superconducting circuits where the Jaynes-Cummings approximation breaks down. In this situation, the interaction between light and matter can only be described correctly by the quantum Rabi model [111, 112] which also takes into account the counterrotating terms describing processes where the number of excitations is no longer conserved, see Sec. 1.4. Reaching the regime of ultrastrong coupling paves the way for various applications and the study of interesting phenomena. For instance, it allows for the realization of ultrafast gates [149] and provides deeper insight into Zeno physics [150] or photon transfer through cavity arrays [50]. Furthermore, a protocol allowing to simulate the regime of ultrastrong coupling with a standard circuit QED setup has been suggested [151]. Such simulations can be used to interpret the results obtained in actual ultrastrong coupling experiments.

4.2.1 Mode structure

For coupled microwave resonators, we expect to observe two resonant modes corresponding to out-of-phase and in-phase oscillating currents in the two resonators, cf. Fig. 4.2(a) and Fig. 4.2(b). We refer to these modes as the antiparallel and parallel mode and assign to them the annihilation operators $\hat{c}_+$ and $\hat{c}_-$, respectively.

To determine the resonator properties, we measure the transmission through both resonators (referred to as a 'through' measurement) and the transmission from one to the respective other resonator ('cross' measurement) as a function of frequency, cf. Fig. 4.1(f). The flux is set far away from the qubit degeneracy point such that the qubit is far detuned and its influence is negligible. The results are shown in Fig. 4.3. First, we determine the fundamental mode frequencies of both resonators from the positions of the antiresonances as discussed in Sec. 1.2.4 and find $\omega_\mathrm{A}/2\pi = 4.8965\,\mathrm{GHz}$ and $\omega_\mathrm{B}/2\pi = 4.8955\,\mathrm{GHz}$. Subsequently, we fit the theoretical transmission of Eq. (1.43) derived from input-output theory to the transmission spectrum measured through resonator A, using the coupling and the resonator decay rates as fit parameters. We determine the geometric coupling between the resonators $g_\mathrm{AB}/2\pi = 8.4\,\mathrm{MHz}$. For the decay rates, we find $\kappa_\mathrm{A}/2\pi = 2.3\,\mathrm{MHz}$ and $\kappa_\mathrm{B}/2\pi = 0.5\,\mathrm{MHz}$. With this set of parameters, we calculate the theoretical transmission as a function of the frequency for the remaining S-parameters shown in Figs. 4.3(b)-4.3(d). As can be seen, all measured S-parameters are described very well by the resonator pa-

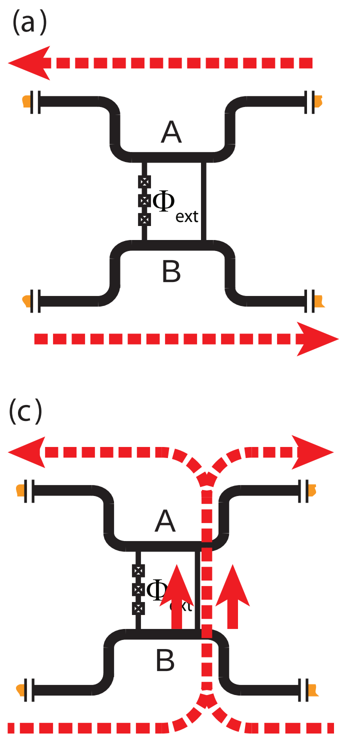

Figure 4.2: Resonant modes of the galvanically coupled qubit-resonator system. The arrows indicate in-phase and out-of-phase oscillating currents. (a) Antiparallel mode $\hat{c}_+$. (b) Parallel mode $\hat{c}_-$. (c) Transverse mode $\hat{c}_t$. (d) Hypothetical antiparallel transverse mode. As the mode currents cancel along the shared branch connecting both resonators, this mode is equivalent to the parallel mode $\hat{c}_-$.

rameters stated above.

Next, we measure the transmission S_{21} through resonator A as a function of frequency and magnetic flux. The input power is chosen such that the population of both resonators is approximately one photon on average[1] and the qubit is kept in the ground state. Far away from the qubit degeneracy point $\delta\Phi_{\mathrm{ext}} = \Phi_{\mathrm{ext}} - \Phi_0/2 = 0$, the antiparallel and parallel mode can be identified in the spectroscopy data presented in Fig. 4.4. Their resonant frequencies are found to be $\omega_+/2\pi = 4.904\,\mathrm{GHz}$ and $\omega_-/2\pi = 4.888\,\mathrm{GHz}$.

As discussed in Sec. 1.5, the qubit can be used to tune the coupling between the two resonators. In addition to the geometric coupling there is the qubit mediated second-order dynamic coupling which depends on the magnetic flux applied to the qubit loop and on the qubit state. If the qubit is in the ground state, there exist certain flux values which we refer to as *switch setting conditions* where the geometric coupling is (in the ideal case) fully compensated by the dynamic coupling such that the total coupling between the two resonators vanishes [120]. The influence of the dynamic coupling manifests

[1]For a detailed description of the power calibration we refer the reader to Ref. [97].

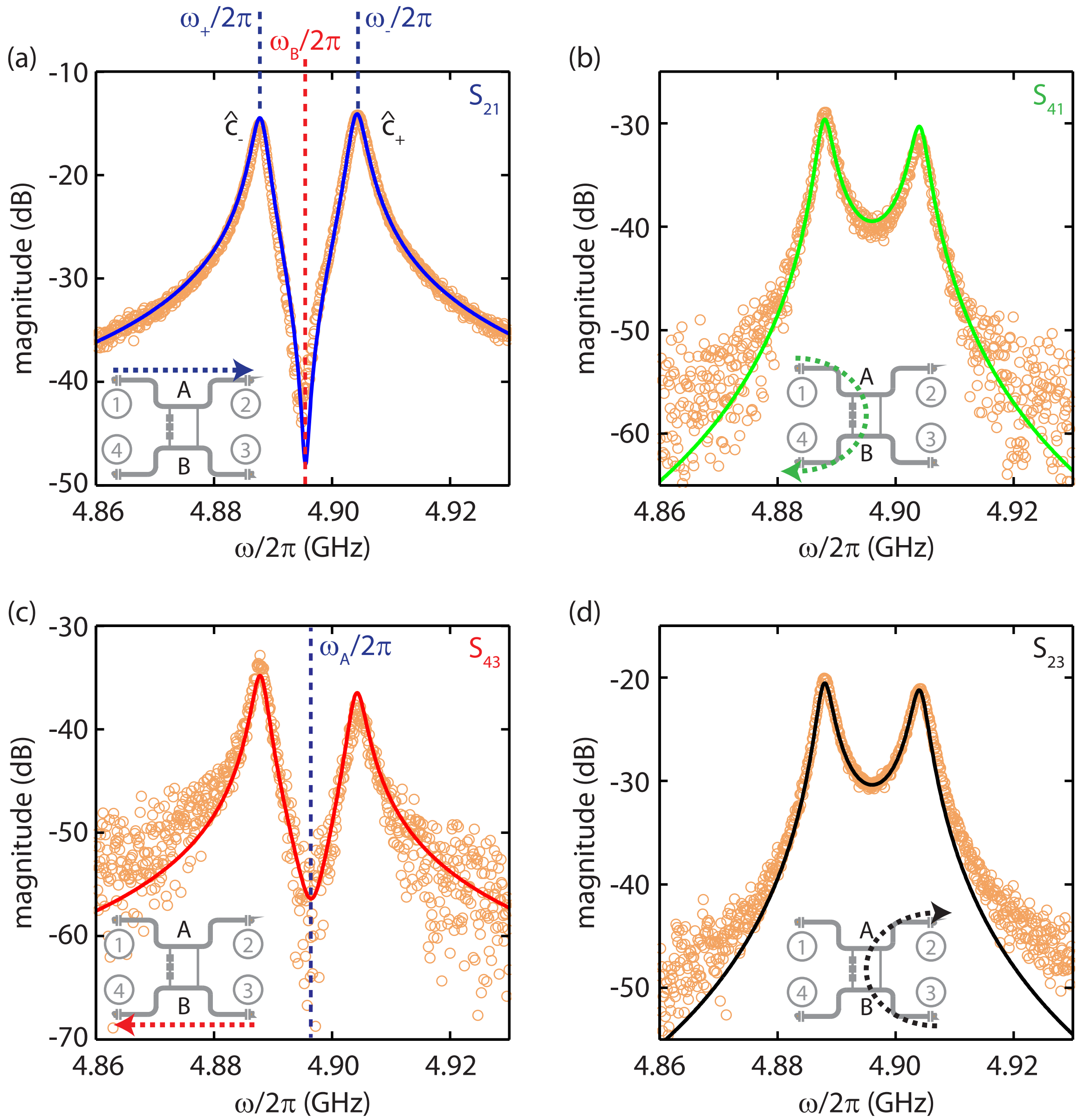

Figure 4.3: Through- and cross-transmission measured with a VNA as a function of frequency with the qubit far detuned ($\omega_q \approx 16\,\mathrm{GHz}$). Brown circles: measurement data. Solid lines: Theoretical description using input-output theory. (a) Transmission S_{21} through resonator A. The anticrossing is located at the resonant frequency of the bare resonator B. The blue line represents a fit of Eq. (1.43) to the data using the coupling and the resonator decay rates as fit parameters. (b) Cross transmission S_{41} measured from resonator A (input) to resonator B. (c) Transmission S_{43} through resonator B. The anticrossing is located at the resonant frequency of the bare resonator A. (d) Cross transmission S_{23} measured from resonator B (input) to resonator A.

itself in the spectroscopy data of Fig. 4.4 as a flux dependence of the antiparallel mode frequency and will be discussed in full detail in Sec. 4.3.

The galvanic coupling of the qubit to both resonators gives rise to a third mode $\hat{c}_{\mathrm{t}}$ which we refer to as the 'transverse mode'. It is identified as a parallel mode across the qubit as shown in Fig. 4.2(c). We note that a hypothetical antiparallel transverse mode as shown in Fig. 4.2(d) cannot be observed. Since the mode currents cancel along the branch connecting the resonators A and B, this mode is identical to the parallel mode $\hat{c}_{-}$.

However, additional resonant structures besides the coupler modes $\hat{c}_{+}$ and $\hat{c}_{-}$ and the (parallel) transverse mode $\hat{c}_{\mathrm{t}}$ can be observed in the spectroscopy data of Fig. 4.4. Near the degeneracy point, an additional resonant structure is visible at the frequency of 4.904 GHz coinciding with the transition between the eigenstates corresponding to the second and sixth lowest eigenenergies of the Hamiltonian of Eq. (4.3). In agreement with a similar resonant structure observed in Ref. [38], we attribute this resonance to a small thermal population of the qubit excited state due to the finite sample temperature of 45 mK. Furthermore, an additional resonant structure is observed around the degeneracy point at the frequency of 4.44 GHz, however, there is no transition between eigenstates of the Hamiltonian of Eq. (4.3) which can be associated with this frequency. An alternative explanation for this structure has yet to be found. We note that both resonant structures are not included in the data basis for the fits described below.

Far away from the qubit degeneracy point, the resonant frequency of the transverse mode $\hat{c}_{\mathrm{t}}$ is found to be $\omega_{\mathrm{t}}/2\pi = 4.508\,\mathrm{GHz}$. To explain the large frequency detuning between the transverse and the (anti)parallel mode, we assume that the inductance of the qubit has to be taken into account in order to correctly describe the frequency of the transverse mode. Following Refs. [152–154], we calculate the resonant frequency of the transverse mode to $\omega_{\mathrm{t}} = \omega_{\mathrm{R}}/(1 + L_{\mathrm{Q}}/L_{\mathrm{R}})$, where L_{Q} is the inductance of the flux qubit and L_{R} is the inductance of a single resonator. The latter is given by $L_{\mathrm{R}} = Z/2\omega_{\mathrm{R}} = 8.2\,\mathrm{nH}$, where $Z = 80\,\Omega$ is the characteristic impedance of the resonator [77]. For simplicity, we assume equal resonator frequencies $\omega_{\mathrm{R}}/2\pi = 4.896\,\mathrm{GHz} \approx \omega_{\mathrm{A,B}}/2\pi$. The inductance of the flux qubit is given by $L_{\mathrm{Q}} = (\partial^2 U_{\mathrm{Q}}/\partial\Phi_{\mathrm{ext}}^2)^{-1}$, where

$$U_{\mathrm{Q}} = E_{\mathrm{J}}[2 + \alpha - \cos\varphi_1 - \cos\varphi_2 - \alpha\cos(2\pi f + \varphi_1 - \varphi_2)] \tag{4.1}$$

is the flux qubit potential, cf. Sec. 1.3.4 and Ref. [16]. The phase drops across the regular qubit junctions are denoted by φ_1 and φ_2, $f = \Phi_{\mathrm{ext}}/\Phi_0$ is the frustration and $E_{\mathrm{J}} = \Phi_0 I_{\mathrm{c}}/2\pi$ is the Josephson energy. Introducing $\varphi_{-} = (\varphi_1 - \varphi_2)/2$, the inductance of the flux qubit reads as

$$L_{\mathrm{Q}} = \Phi_0/[2\pi\alpha I_{\mathrm{c}}\cos(2\pi f + 2\varphi_-)], \tag{4.2}$$

with a minimum value of $L_{\mathrm{Q}}(f=0,\varphi_-=0) = \Phi_0/2\pi\alpha I_{\mathrm{c}} = 719\,\mathrm{pH}$, yielding a resonant frequency of $\omega_{\mathrm{t,theo}}/2\pi = 4.501\,\mathrm{GHz}$. This value is in excellent agreement with the experimental value $\omega_{\mathrm{t}}/2\pi = 4.508\,\mathrm{GHz}$ measured far away from the degeneracy point. To keep the theoretical modelling simple, in the following we assume a constant transverse mode frequency ω_{t}. That is, we assume that the experimentally observed flux dependence is solely due to the interaction with the flux qubit.

To gain further insight, we consider the Hamiltonian describing the coupling of the qubit to all resonant modes:

$$\begin{aligned} \hat{H} = \hat{H}_{\mathrm{Q}} + \sum_{\substack{n= \\ \{+,-,t,3t,3+\}}} \hat{H}_n \\ + \hbar g\sqrt{2}\;\hat{\sigma}_z(\hat{c}_+^\dagger + \hat{c}_+) \\ + \hbar g_{\mathrm{t}}\;\hat{\sigma}_z(\hat{c}_{\mathrm{t}}^\dagger + \hat{c}_{\mathrm{t}}) \\ + \hbar g_{3\mathrm{t}}\;\hat{\sigma}_z(\hat{c}_{3\mathrm{t}}^\dagger + \hat{c}_{3\mathrm{t}}) \\ + \hbar g_{3+}\;\hat{\sigma}_z(\hat{c}_{3+}^\dagger + \hat{c}_{3+}). \end{aligned} \tag{4.3}$$

Here, $\hat{H}_{\mathrm{Q}} = (\varepsilon/2)\hat{\sigma}_z + (\Delta/2)\hat{\sigma}_x$ is the qubit Hamiltonian and $\hat{H}_n = \hbar\omega_n\hat{c}_n^\dagger\hat{c}_n$ is the Hamiltonian describing the resonant mode $\hat{c}_n$. Δ is the qubit energy gap, $\epsilon(\Phi_{\mathrm{ext}}) = 2I_{\mathrm{p}}\delta\Phi_{\mathrm{ext}}$ denotes the qubit energy bias, and $I_{\mathrm{p}} = I_{\mathrm{c}}\sqrt{1-(2\alpha)^{-2}}$ the qubit persistent current. $\hat{\sigma}_x$ and $\hat{\sigma}_z$ are the Pauli operators. As shown in Ref. [39], the coupling of the qubit to the antiparallel mode is given by $g_+ = \sqrt{2}g$ whereas there is virtually no coupling of the qubit to the parallel mode as the latter does not generate a magnetic field at the position of the qubit. To increase precision of our description, we also take into account the third harmonic of the $\hat{c}_{\mathrm{t}}$-mode (denoted by $\hat{c}_{3\mathrm{t}}$, located at $\omega_{3\mathrm{t}}/2\pi = 13.1\,\mathrm{GHz}$) and the third harmonic of the $\hat{c}_+$-mode (denoted by $\hat{c}_{3+}$, at $\omega_{3+}/2\pi = 14.3\,\mathrm{GHz}$). We do not consider the second harmonics since they exhibit current nodes at the qubit position and therefore do not couple to the qubit. The coupling strengths $g_{3\mathrm{t}}$ and g_{3+} are not considered as independent parameters, but are calculated via $g_{3\mathrm{t}}/2\pi = (g_{\mathrm{t}}/2\pi)\sqrt{\omega_{3\mathrm{t}}/\omega_{\mathrm{t}}}$ and $g_{3+}/2\pi = (g_+/2\pi)\sqrt{\omega_{3+}/\omega_+}$, taking into account the current distribution in the resonator. Fitting the Hamiltonian of Eq. (4.3) to our data (cf. Fig. 4.4), the qubit energy gap is determined to $\Delta/h = 3.55\,\mathrm{GHz}$ and the persistent current to $I_{\mathrm{p}} = 458\,\mathrm{nA}$. We find that the coupling strength between the qubit and each resonator is given by $g/2\pi = 96.7\,\mathrm{MHz}$ and the coupling strength of the mode $\hat{c}_{\mathrm{t}}$ to the qubit is $g_{\mathrm{t}}/2\pi = 775\,\mathrm{MHz}$ which is as high as 17.2 % of the respective mode frequency. Remarkably, the coupling strength even

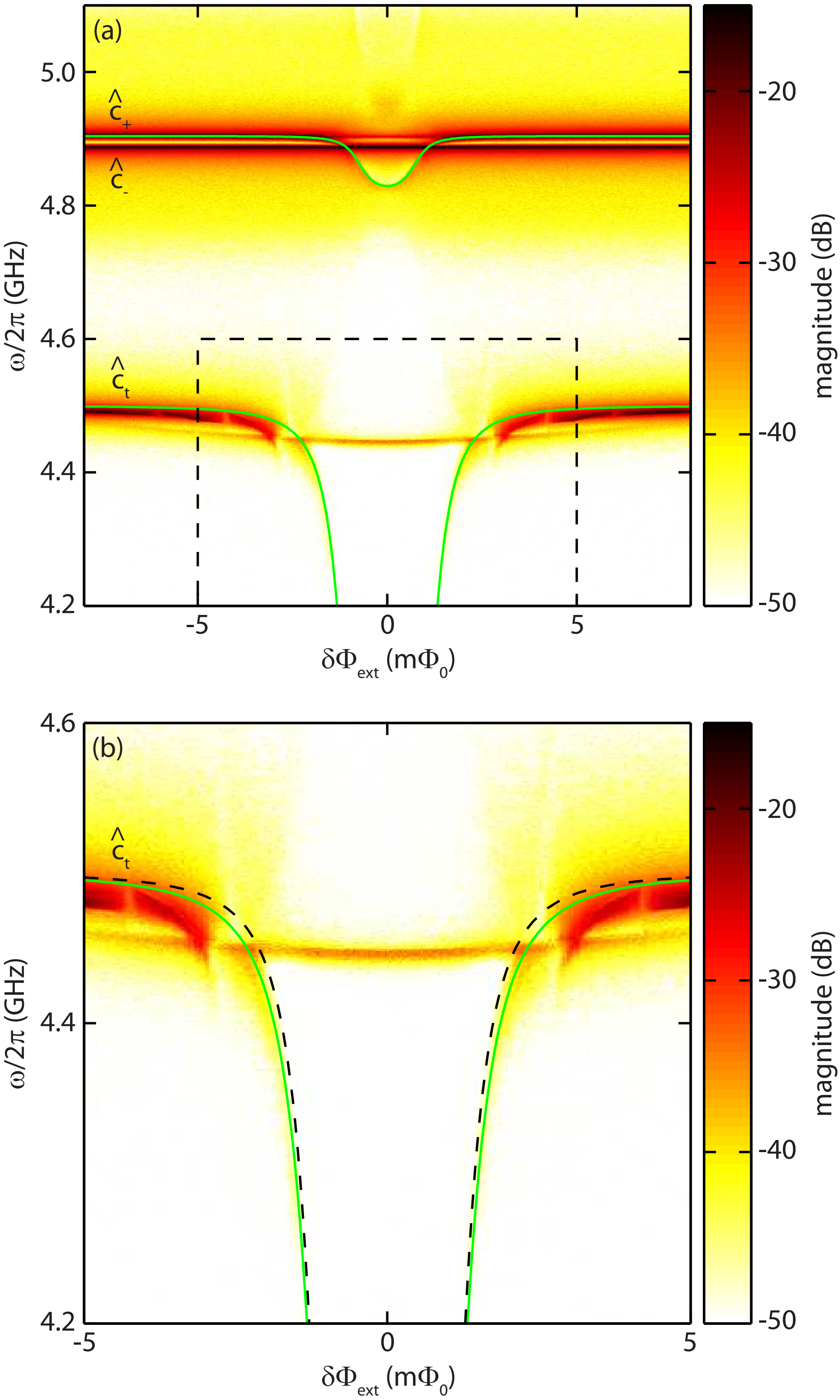

Figure 4.4: (a) Transmission measured through resonator A depending on the applied magnetic flux with the qubit in the ground state. Green line: Fit using the Hamiltonian of Eq. (4.3). The area shown in panel (b) is marked by the black rectangle. (b) Detail of (a). Solid green line: Fit using the Hamiltonian of Eq. (4.3). Dashed black line: Description within the Jaynes-Cummings model.

exceeds the relative coupling strengths observed in Ref. [37] although the coupling is determined solely by the geometrical properties of the qubit arm and not by an additional inductive element such as a Josephson junction introduced in Ref. [37] to enhance the coupling strength. To understand the origin of the exceptionally large coupling strength, we assume that the coupling strength of the qubit to resonator A and B, respectively, is determined by the shared arms between the qubit and the resonators A and B, respectively. We further assume that the transverse mode current is flowing predominantly through the qubit arm without Josephson junctions as shown in Fig. 4.2(c). This assumption is well justified since the geometric inductance of the qubit arm without Josephson junctions is much smaller than the total inductance of the branch containing the three Josephson junctions.

Following Ref. [155], we can estimate the geometric inductance of the qubit branch connecting the two resonators A and B (length 30 µm, width 0.5 µm, thickness 0.1 µm) to 31 pH which adds to the kinetic inductance [63] of approx. 27 pH, yielding a total inductance of the qubit branch $L_\mathrm{t} = 58\,\mathrm{pH}$. We further can estimate the inductance of the shared arms (length 20 µm) between the resonators (total length 11.55 mm) A and B and the qubit to $L_\mathrm{r} = L_\mathrm{R} \cdot 20\,\mu\mathrm{m}/11.55\,\mathrm{mm} = 14.2\,\mathrm{pH}$. The coupling strength g_+ between the antiparallel mode and the flux qubit is given by $\hbar g_+ = 2L_\mathrm{r} I_\mathrm{p} I_+$ where $I_+ = \sqrt{\hbar\omega_\mathrm{R}/2L_\mathrm{R}}$ is the vacuum current of the antiparallel mode [37]. The total coupling strength g_t of the mode $\hat{c}_\mathrm{t}$ to the qubit is comprised of two contributions. The first one is the coupling mediated by the shared branch between qubit and resonator and the second one is the coupling mediated by the qubit branch connecting the two resonators. Therefore, we can calculate the coupling strength $\hbar g_\mathrm{t} = 2L_\mathrm{r} I_\mathrm{p} I_\mathrm{t} + 2L_\mathrm{t} I_\mathrm{p} I_\mathrm{t}$, where I_t is the vacuum current of the mode $\hat{c}_\mathrm{t}$. With these results, we estimate a ratio $g_\mathrm{t}/g_+ = (\omega_\mathrm{t}/\omega_\mathrm{R}) \cdot (2L_\mathrm{t} + 2L_\mathrm{r})/2L_\mathrm{r} \approx 4.7$ in good agreement with the experimentally found ratio of 5.7.

4.2.2 Ultrastrong coupling

In what follows, we briefly reiterate the theoretical framework needed to describe the interaction between the qubit and the multimode structure arising from our two-resonator circuit QED architecture, cf. Sec. 1.4.3. First, we rotate the Hamiltonian of Eq. (4.3) into the qubit eigenbasis using the transformations

$$\hat{\sigma}_\mathrm{z} \rightarrow \cos\theta\hat{\sigma}_\mathrm{z} - \sin\theta\hat{\sigma}_\mathrm{x}, \tag{4.4}$$

$$\hat{\sigma}_\mathrm{x} \rightarrow \sin\theta\hat{\sigma}_\mathrm{z} + \cos\theta\hat{\sigma}_\mathrm{x}, \tag{4.5}$$

where $\sin\theta = \Delta/\hbar\omega_\mathrm{q}$ and $\cos\theta = \epsilon/\hbar\omega_\mathrm{q}$ and $\hbar\omega_\mathrm{q} = \sqrt{\Delta^2 + \epsilon^2}$ is the flux-dependent qubit transition energy. In the qubit eigenbasis, the Hamiltonian reads

$$\hat{H}^* = \hat{H}_\mathrm{Q}^* + \sum_{\substack{n= \\ \{t,+,3t,3+\}}} \left[\hat{H}_n + \hbar g_n \left(\hat{c}_n^\dagger + \hat{c}_n\right)\left(\cos\theta\hat{\sigma}_\mathrm{z} - \sin\theta\hat{\sigma}_\mathrm{x}\right)\right] \tag{4.6}$$

with $\hat{H}_\mathrm{Q}^* = \frac{\hbar\omega_\mathrm{q}}{2}\hat{\sigma}_\mathrm{z}$. At $\Phi_\mathrm{ext} = \Phi_0/2$, the Hamiltonian of Eq. (4.6) represents a multimode quantum Rabi model. We note that we drop the $\hat{c}_-$-mode since it does not couple to the qubit. Defining the qubit state raising and lowering operators $\hat{\sigma}_\pm = (\hat{\sigma}_x \pm i\hat{\sigma}_y)/2$, we find that the Hamiltonian of Eq. (4.6) explicitely contains counterrotating terms of the form $\hat{c}_n^\dagger\hat{\sigma}_+$ and $\hat{c}_n\hat{\sigma}_-$. For $g_n \ll \omega_n$, a rotating wave approximation reduces the Hamiltonian of Eq. (4.6) to the well known multimode Jaynes-Cummings Hamiltonian for arbitrary Φ_ext. Following Ref. [37], the regime of *ultrastrong coupling* is reached when the interaction between the qubit and one or multiple modes can only be described by the quantum Rabi model, but qualitative deviations from the Jaynes-Cummings model are observed. Despite these deviations, the system dynamics still reflects the intuition of several distinct, but coupled systems exchanging excitations. This intuition breaks down completely in the *deep strong coupling regime* [156], where $g \gtrsim \omega$ and the dynamics of the system is characterized by the emergence of two parity chains.

Next, we analyze whether our multipartite circuit QED setup comprised of a flux qubit and two galvanically coupled resonators is consistent with the Jaynes-Cummings model or whether it has to be treated within the more general Rabi model. First, we assume that the Rabi model represents a valid theoretical model for our setup and fit the Hamiltonian of Eq. (4.6) to our spectroscopy data. As shown by Fig. 4.5(a), theory and experimental data agree very well for the $\hat{c}_+$-mode. However, if we drop the counterrotating terms without making a new fit, we find a pronounced qualitative deviation between our experimental data and the Jaynes-Cummings model prediction. The observed deviations are in agreement with the observation of the Bloch-Siegert shift in a system comprised of a flux qubit coupled ultrastrongly to an *LC*-resonator [38]. Figure 4.4(b) shows the fit of the full Hamiltonian to our spectroscopy data for the transverse mode $\hat{c}_\mathrm{t}$ and the corresponding description within the Jaynes-Cummings model. Even if a small quantitative difference can be observed, there is no qualitative difference between the two models. This can be understood considering the fact that the Bloch-Siegert shift is proportional to $g^2\sin^2\theta/(\omega_\mathrm{Q} + \omega_\mathrm{R})$ and, hence, is most prominent near the qubit degeneracy point. However, the pronounced qualitative deviation between Rabi and Jaynes-Cummings model for the $\hat{c}_+$-mode (cf. Fig. 4.5(a)) indicates that the rotating wave approximation is no longer valid. This demonstrates that the full quantum Rabi model has to be used to

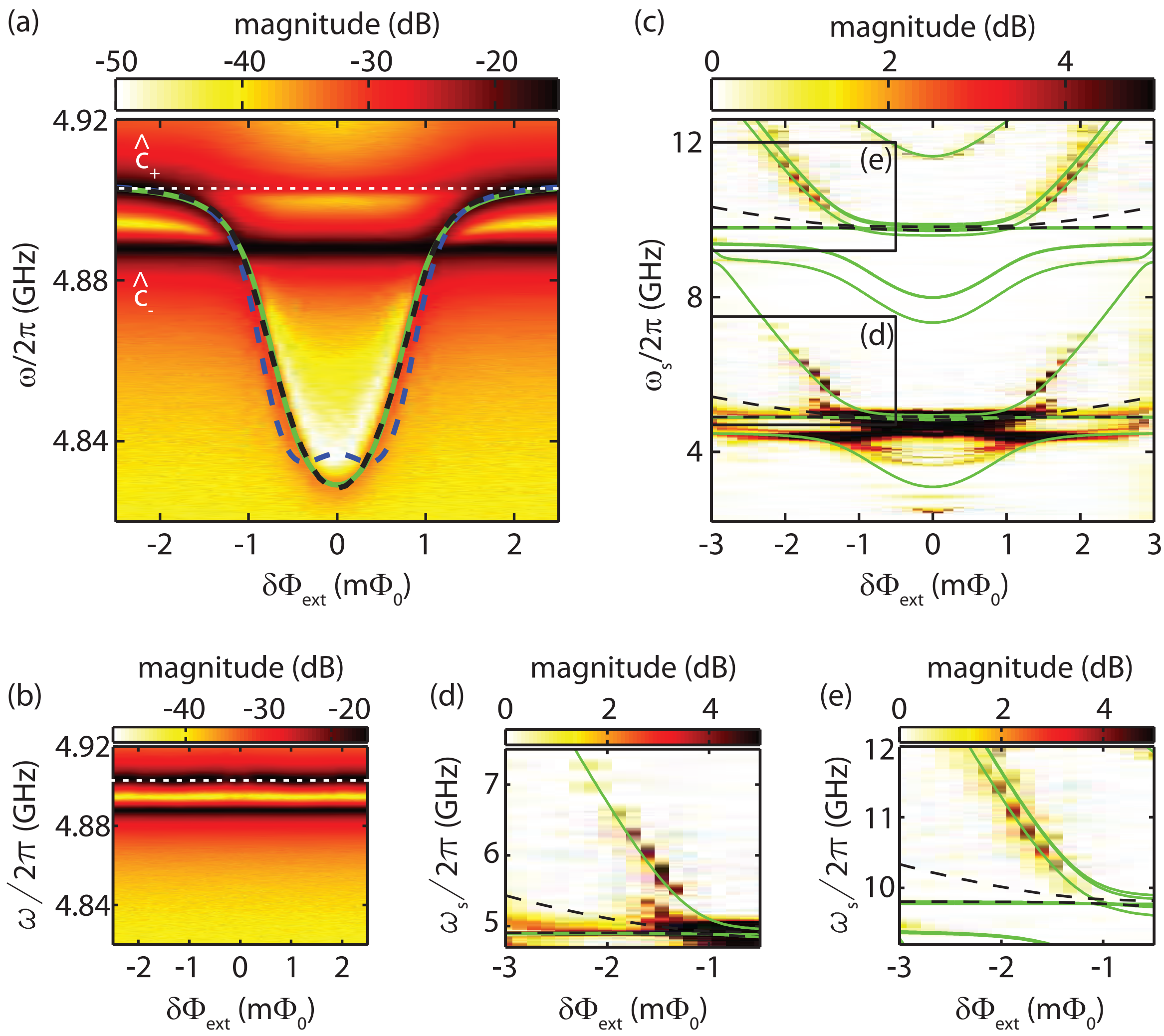

Figure 4.5: Breakdown of the Jaynes-Cummings model. (a) Transmission measured through resonator A depending on the magnetic flux applied to the flux qubit (detail from Fig. 4.4) with the qubit in the ground state. Green line: Fit of the full Hamiltonian of Eq. (4.3). Blue dashed line: Prediction by the Jaynes-Cummings model. Black dashed line: Fit to the Jaynes-Cummings model neglecting the transverse mode. White dashed line: Measurement frequency for two-tone spectroscopy. (b) Same as (a), qubit driven with strong excitation signal. (c) Two-tone spectroscopy. Green lines: Fit of the spectroscopy data to the full Hamiltonian (4.3). Black dashed lines: Description within the Jaynes-Cummings model. (d, e) Details from (c).

correctly describe our experimental findings.

However, one may doubt our interpretation of the transverse mode and argue that the latter is not originating from the galvanic coupling of the qubit to the resonators A and B. One could further assume that the mode $\hat{c}_t$ is an independent phenomenon in the sense that its flux dependence is not a manifestation of its coupling to the qubit. In other words, a very critical reader may suggest to omit the transverse mode from the

Hamiltonian of Eq. (4.6) and fit only the coupler modes to the Hamiltonian

$$\begin{aligned}\hat{H} = \hat{H}_{\mathrm{Q}}^{*} + \sum_{\mathrm{n}=\{+,3+\}} \hat{H}_n \\ + \hbar g_{+}(\hat{c}_{+}^{\dagger}\hat{\sigma}_{-} + \hat{c}_{+}\hat{\sigma}_{+}) \\ + \hbar g_{3+}(\hat{c}_{3+}^{\dagger}\hat{\sigma}_{-} + \hat{c}_{3+}\hat{\sigma}_{+})\end{aligned} \tag{4.7}$$

which contains no counterrotating terms anymore. As shown in Fig. 4.5(a), our transmission data are described well by this model. However, even if the fit looks nice, this ansatz yields qubit parameters deviating strongly from the qubit parameters given in Sec. 4.2.1, where we performed the fit using the Hamiltonian of Eq. (4.6). In order to verify which of the two parameter sets is incorrect, we make use of the fact that our measurement setup does not only provide access to the eigenmodes of the coupled qubit-resonator system, but also allows to perform spectroscopy of the qubit using a two-tone spectroscopy experiment. To this end, we record the transmission through resonator A at the frequency of $\omega_{+}/2\pi = 4.904\,\mathrm{GHz}$. When the qubit is far detuned, this corresponds to the resonant frequency of the $\hat{c}_{+}$-mode. In addition, a second microwave tone, the *spectroscopy tone*, with variable frequency ω_{s} is applied to the coupled qubit-resonator system via the input port of resonator B. When the qubit is in the ground state, the measured transmission as a function of the magnetic flux applied to the qubit loop corresponds to a cut through Fig. 4.5(a) along $\omega_{+}/2\pi$ as highlighted by the white dashed line. When the qubit is saturated by means of the spectroscopy tone, the qubit state is described by the density matrix $\rho_{\mathrm{M}} = \frac{1}{2}(|g\rangle\langle g| + |e\rangle\langle e|)$ and the transmission spectrum turns into the one shown in Fig. 4.5(b). Evidently, the transmission magnitude at $\omega_{+}/2\pi$ increases near the degeneracy point when the qubit is driven. Using this protocol, we record the change in resonator transmission as a function of the spectroscopy tone frequency ω_{s} and the applied magnetic flux, cf. Figs. 4.5(c)-(e). We compare the measured data to the energy level spectrum of the Hamiltonian of Eq. (4.6) by calculating the energy differences between the ground state and the 15 lowest energy levels. As can be seen, there is very good agreement between our two-tone spectroscopy data and their description within the full Hamiltonian of Eq. (4.6). However, the energy level spectrum calculated from the qubit parameters found by a fit of the $\hat{c}_{+}$-mode within the Jaynes-Cummings approximation clearly deviates from the two-tone spectroscopy data. In other words, treating the mode $\hat{c}_{\mathrm{t}}$ independently of the mode $\hat{c}_{+}$ clearly does not allow us to correctly describe our experimental data within the Jaynes-Cummings model. In turn, our findings also strengthen our interpretation of the transverse mode.

Finally, we compare our findings to previous work on ultrastrong coupling in superconducting circuits. In the present sample, the access to both resonator and qubit spectroscopy data allows us to rigorously rule out the validity of the Jaynes-Cummings model without having to assume the validity of the Rabi model. Hence, our analysis goes beyond the treatment presented in Ref. [38], where only quantitative, but no qualitative deviations between the quantum Rabi model and the Jaynes-Cummings model were observed in a system comprised of a flux qubit coupled to an LC-resonator. In addition, the present work is markedly different from the approach used in Ref. [37]. There, it was shown that in a multimode system the number of excitations is no longer preserved in the ultrastrong coupling regime. Despite this difference, it appears that physics beyond the Jaynes-Cummings model in circuit QED is favourably demonstrated by analyzing the complex mode structure of multipartite setups.

4.3 Tunable and switchable coupling between superconducting resonators

In this section we demonstrate tunable and switchable coupling between the two resonators A and B. Using transmission spectroscopy, we find that the coupling can be tuned via the external magnetic flux applied to the qubit loop. Finally, we perform a time-domain experiment making the switching process directly observable and show that the coupling can be switched by varying the qubit population.

In Sec. 4.2.1 we have found that the resonators A and B are not exactly frequency degenerate. However, the deviation of the fundamental mode frequencies is on the order of the resonator decay rates and therefore negligible. In what follows, we therefore round the fundamental mode frequencies of both resonators to $\omega_{\mathrm{R}}/2\pi = 4.896\,\mathrm{GHz}$. Furthermore, as shown in Ref. [120], the working principle for tunable and switchable coupling using the architecture described in this thesis also applies to detuned resonators.

4.3.1 Tuning the coupling via the external field

To demonstrate tunable coupling between the two resonators, we measure transmission through the latter with a vector network analyzer as shown in Fig. 4.6 as a function of the applied magnetic flux Φ_{ext}. Fig. 4.7(a) shows the results of the 'through'-measurement of resonator A whereas Fig. 4.7(b) represents a 'cross'-measurement from the input of resonator A to the output of resonator B. For both measurements, the qubit remains in the ground state. The input power is chosen such that the population of both resonators is approximately one photon on average. The splitting between the antiparallel and the parallel mode, cf. Sec. 4.2.1, far away from the qubit degeneracy point is $2g_{\mathrm{AB}}$. If the flux

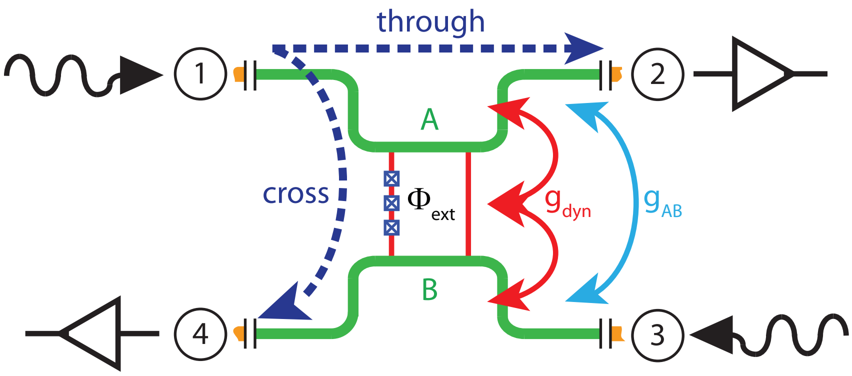

Figure 4.6: To demonstrate tunable coupling via the external magnetic field, we measure transmission through resonator A ('through'-measurement, S_{21}) and transmission from the input of resonator A to the output of resonator B ('cross'-measurement, S_{41}) as a function of external magnetic flux. The coupling between the resonators is mediated by the geometry-defined flux-independent geometric coupling and the flux- and qubit-state-dependent dynamic coupling.

is tuned towards the degeneracy point, the frequency of the lower mode stays constant while the frequency of the upper mode is shifted to lower frequencies as expected from Eq. (1.118).

In this way, the flux can be tuned such that the frequency of the upper mode matches the frequency of the lower mode. We refer to these points as the *switch setting conditions* where the geometric coupling is fully compensated by the dynamical coupling. Consequently, the two resonators are expected to be decoupled from each other if the switch setting condition is fulfilled. In order to find the minimum value of the coupling for our device, we fit the mode spectrum shown in Fig. 4.7(a) using input-output theory [80, 83] and analyze the coupling depending on the magnetic flux. Results are shown in Fig. 4.8. At the switch setting condition, the coupling is reduced to $|g_{\mathrm{res,min}}/2\pi| \lesssim 1.5\,\mathrm{MHz}$. Here, our analysis is limited by the decay rates of the resonators. Compared to the coupling far off the degeneracy point, the coupling at the switch setting condition is reduced by a factor of at least 5.5.

4.3.2 Tuning the coupling via the qubit population

So far, we have investigated how to tune the coupling via the magnetic flux applied to the qubit loop. Next, we show that the coupling is also controlled by the qubit population as expected from Eq. (1.118). To this end, we record the resonator transmission while driving the qubit with a strong excitation signal applied through the input port of the other resonator. This results in equal probabilities to find the qubit in the ground and excited state, yielding $\langle\hat{\sigma}_\mathrm{z}\rangle = \mathrm{Tr}\left[\rho_\mathrm{M}\hat{\sigma}_\mathrm{z}\right] = 0$ where $\rho_\mathrm{M} = \frac{1}{2}\left(|\mathrm{g}\rangle\langle\mathrm{g}| + |\mathrm{e}\rangle\langle\mathrm{e}|\right)$. As expected

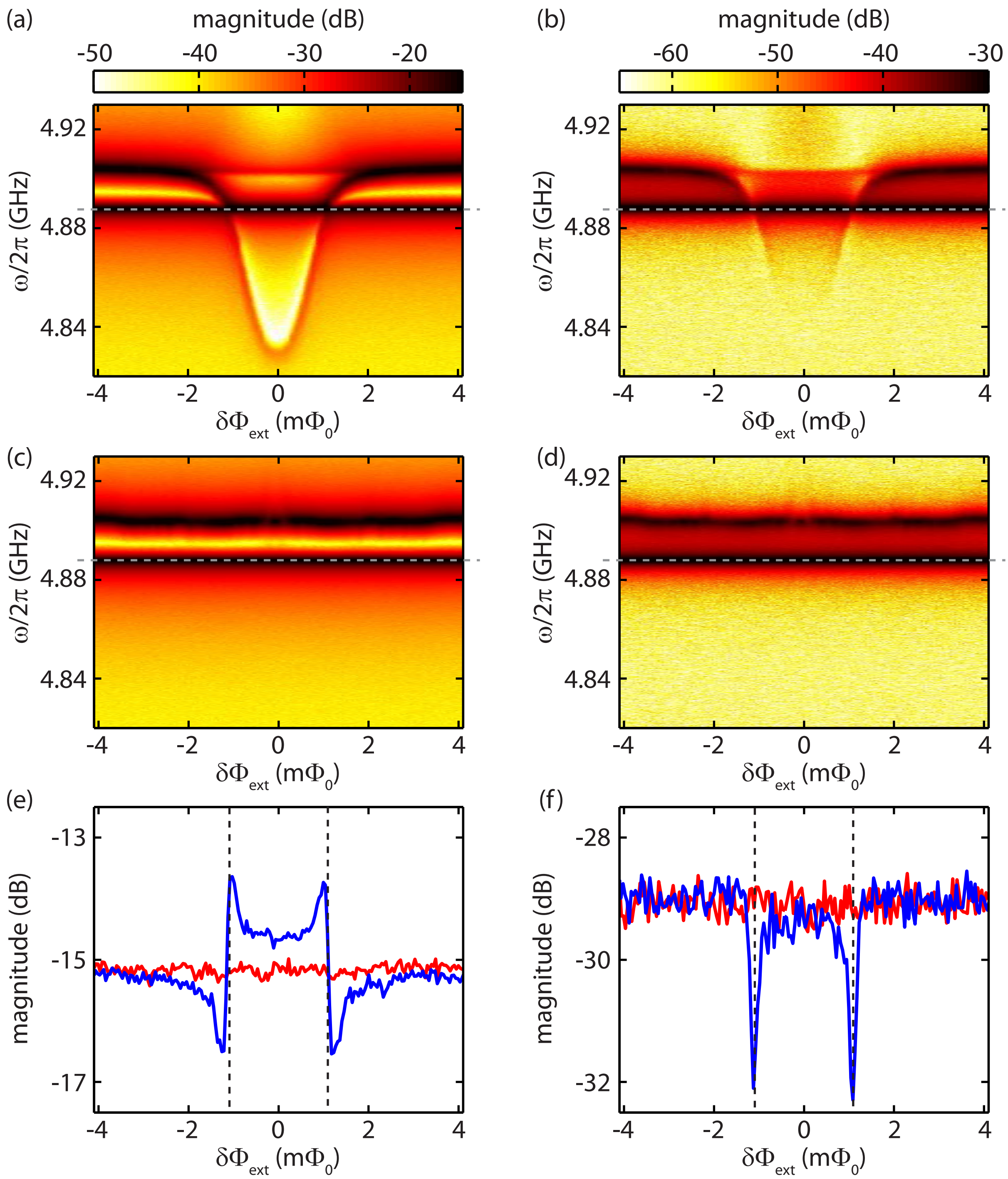

Figure 4.7: (a) Transmission through resonator A depending on the applied magnetic flux with the qubit in ground state. (b) 'Cross' measurement, qubit in ground state. (c) 'Through' measurement, qubit driven with strong excitation signal. (d) Same as (c) for the 'cross' measurement. (e) 'Through' measurement, transmission at the frequency of the lower mode at 4.888 GHz [dashed lines in (a) and (c)] with qubit in ground state (blue line) and saturated qubit (red line). Dashed black lines: Switch setting conditions. (f) Same as (e) for the 'cross' measurement.

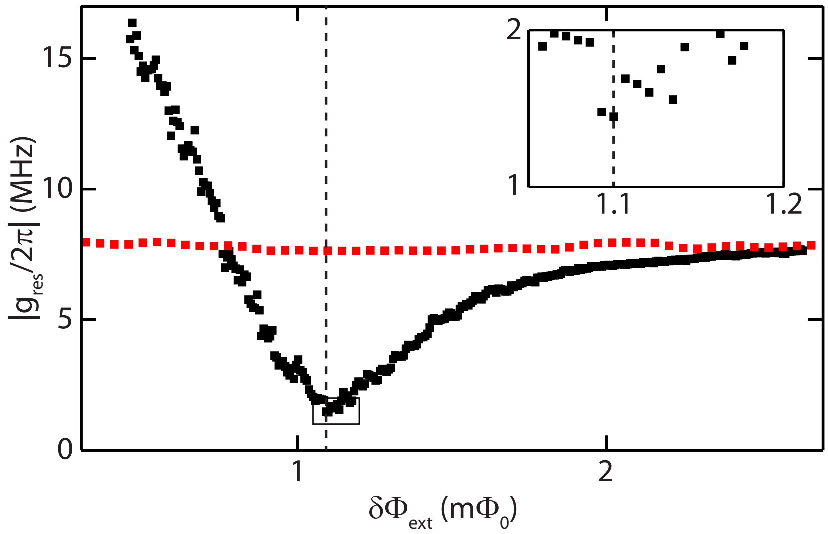

Figure 4.8: Magnitude of the total coupling between the resonators extracted from a 'through' measurement near the switch setting condition. Black: qubit in ground state. Red: saturated qubit. Inset: Measurement with increased flux resolution around switch setting condition.

from Eq. (1.112) we observe that the coupling between the two resonators is then given by g_{AB} independently of the applied flux, see Figs. 4.7(c), 4.7(d) and Fig. 4.8. To analyze the interplay of flux- and qubit state dependence in more detail, we show the transmission at the frequency of the lower mode at $\omega/2\pi = 4.888\,\mathrm{GHz}$ in Fig. 4.7(e) and Fig. 4.7(f). For the qubit in the ground state, we observe increased transmission for the 'through'-measurement at the switch setting conditions compared to flux values not matching a switch setting condition or compared to the qubit being driven. This is in agreement with our expectation that, when turning off the coupling, the signal incident on one resonator cannot cross over to the other one. Consistently, we observe reduced transmission at the switch setting condition in the 'cross' measurement shown in Fig. 4.7(f). Two dips are visible in the through transmission [Fig. 4.7(e)], when the qubit is in the ground state. They originate from the differences in the linewidths and also from the small detuning between the two resonators. The resonant structure close to the frequency of the out-of-phase mode [cf. Fig. 4.7(a) and Fig. 4.7(b)], is suppressed by approx. 15 dB and not relevant for the discussion presented here.

Next, we conduct time domain experiments making the switchable coupling directly observable. To this end, we set the flux bias corresponding to the switch setting condition and apply a microwave probe pulse (length $\tau_{\mathrm{res}} = 30\,\mu\mathrm{s}$) to one of the resonators at the frequency $\omega_{\mathrm{res}}/2\pi = 4.888\,\mathrm{GHz}$ of the lower ($\hat{c}_{-}$) mode. In addition, a $10\,\mu\mathrm{s}$ long microwave driving pulse switches on the coupling between the resonators for a period of $10\,\mu\mathrm{s}$ as shown in Fig. 4.9(a). The output signals of both resonators are detected in a time-resolved way using FPGA-enhanced A/D-converters. Typical pairs of time traces are shown in Figs. 4.9(b)-4.9(d). After switching on the qubit drive, the output signal level of the resonator where the probe pulse is applied decreases, whereas it increases for the other resonator. This result represents a direct experimental evidence for the expected switching behaviour because it implies that the transfer of energy from one into another resonator can be controlled via the qubit. However, for an ideal coupler, one would expect that at the switch setting condition the output signal level for the 'cross'-measurement is zero when the qubit is in the ground state, even if the probe pulse is on. Nevertheless, in our case a finite output power can be observed. We attribute this to the complex mode structure of our particular device, cf. Fig. 4.4 and Fig. 4.5. Specifically, the transverse mode $\hat{c}_{\mathrm{t}}$ might give rise to an additional coupling channel between the two resonators A and B which cannot be tuned by means of the external magnetic flux. To test this hypothesis, additional measurements on a non-galvanically coupled sample, where the mode structure simplifies to the two coupler modes, would have to be performed.

To quantify the coupler performance, we define the switching efficiency

$$\eta \equiv 1 - n_{\mathrm{B}}^{\mathrm{off}} / n_{\mathrm{A}}^{\mathrm{off}} = 1 - B_{\mathrm{off}} / A_{\mathrm{off}}. \tag{4.8}$$

Here and in the following, $n_{\mathrm{B}}^{\mathrm{on/off}}$ and $n_{\mathrm{A}}^{\mathrm{on/off}}$ denote the resonator populations when the coupling is switched on/off. Following input-output theory [80], the ratio $n_{\mathrm{B}}^{\mathrm{off}}/n_{\mathrm{A}}^{\mathrm{off}}$ is equal to that of the quantities B_{off} and A_{off} indicated in Fig. 4.9. The switching efficiency η is most intuitively understood by looking at its limiting cases. For a perfect coupler ($\eta = 1$), we find $n_{\mathrm{A}}^{\mathrm{on}} = n_{\mathrm{B}}^{\mathrm{on}}$ when the coupling is switched on and $n_{\mathrm{A}}^{\mathrm{off}} = n$, $n_{\mathrm{B}}^{\mathrm{off}} = 0$ when the coupling is switched off. Conversely, when the coupler is not tunable at all ($\eta = 0$), $n_{\mathrm{A}}^{\mathrm{on/off}} = n_{\mathrm{B}}^{\mathrm{on/off}}$ regardless of the coupler state. For intermediate values of η, a fraction of $(1-\eta)/(2-\eta)$ photons leaks into resonator B despite the coupler being in the 'off' state.

Next, we analyze η as a function of mean number of photons (calibrated via dispersive shift of the qubit, cf. Ref. [97]) in the $\hat{c}_{-}$-mode. The results are shown in Fig. 4.10(a). For low photon numbers we find a switching efficiency of $\eta \approx 0.62$. Above approximately 1 photon, η starts to decrease and vanishes for photon numbers exceeding 10^4. This behaviour is in agreement with the disappearance of the Jaynes-Cummings-doublet due to a quantum-to-classical transition observed in a transmon-resonator system.[157]

Finally, we demonstrate that the resonator-resonator coupling strength can also be controlled via the qubit drive power, cf. Fig. 4.10(b). This scenario is of particular importance for the simulation of, e.g., the Bose-Hubbard-Hamiltonian where it is favorable to be able to vary the coupling between adjacent resonators by an easily controllable external parameter such as the qubit drive power. For a given qubit drive pulse power

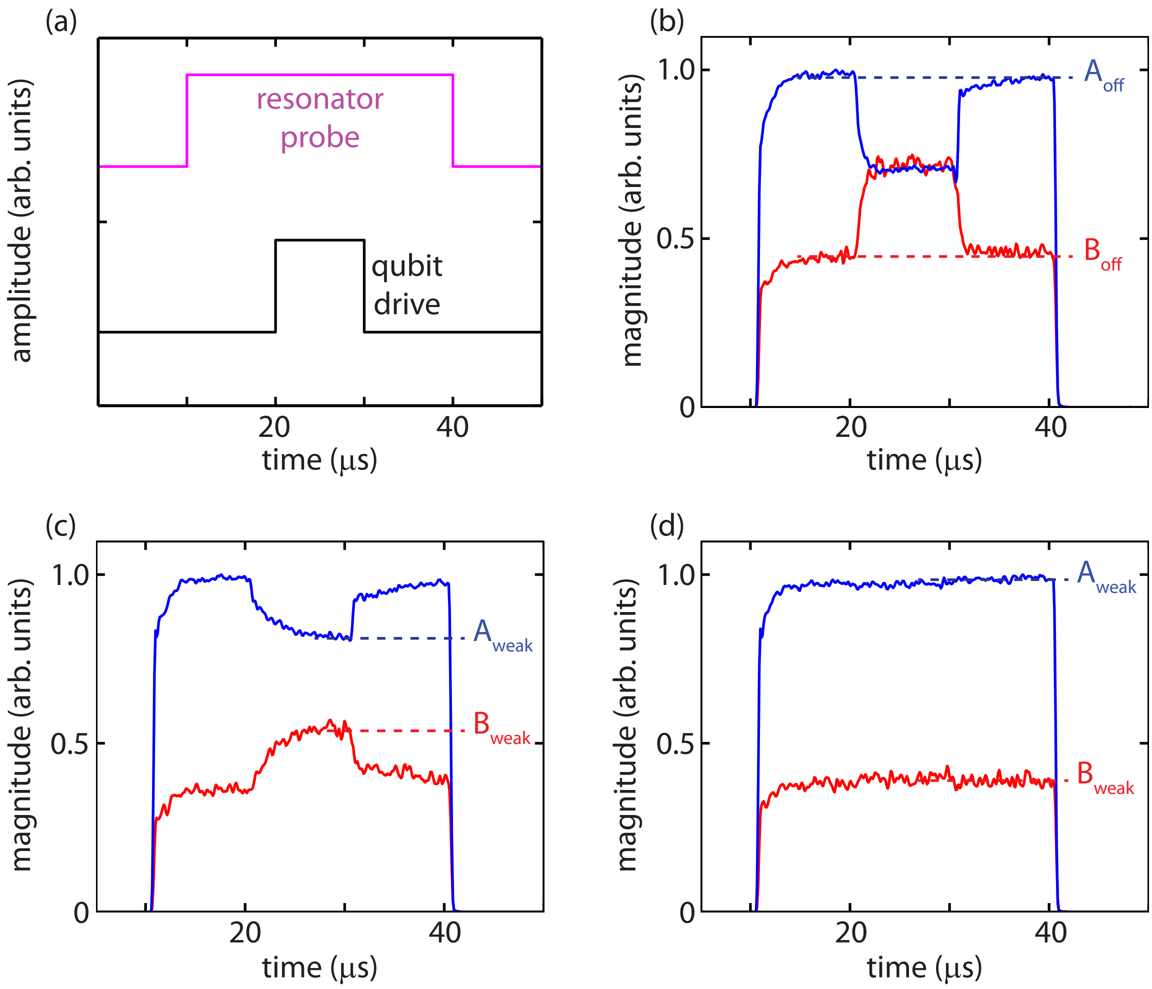

Figure 4.9: (a) Pulse pattern for the time-domain probe of the coupler. (b) Typical measured time traces of the output signals of the two resonators. The qubit drive pulse is strong enough to saturate the qubit. Blue: 'through' transmission measurement. red: 'cross' transmission measurement. The power levels are referred to those inside the resonators, i.e. they are scaled such that they are equal when the coupling is 'on'. This assumption is justified because $g_{AB} \gg \kappa_A, \kappa_B$. (c) Same as (b) for intermediate qubit drive pulse power. (d) Same as (b) for small drive pulse power.

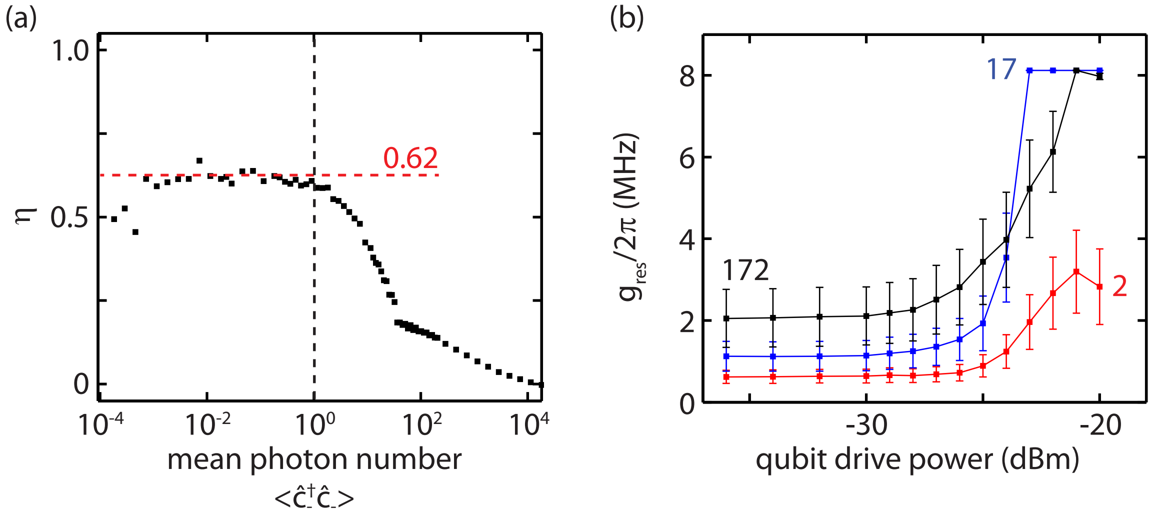

Figure 4.10: (a) Switching efficiency η as a function of the mean resonator drive. (b) Total resonator-resonator coupling as a function of the qubit drive power (referenced to signal generator output) measured for three different resonator populations (2, 17 and 172 poa). The points of the red curve at $-20\,$dBm, $-24\,$dBm, $-30\,$dBm are derived from the data of Figs. 4.9(b), 4.9(c), 4.9(d), respectively.

and mean resonator photon number, we measure the output powers of both resonators. The latter can also be calculated theoretically using input-output theory, cf. Sec. 1.2.4, as a function of the resonator-resonator coupling strength. Comparing our measurements to the theoretical calculations then allows us to determine the resonator-resonator coupling strength in dependence of qubit drive power and resonator population. For low resonator probe photon numbers and weak qubit drive, the residual coupling between the resonators is determined as 0.62(16) MHz, representing a reduction of the coupling strength by one order of magnitude as compared to the geometric coupling g_{AB}. The error bars in Fig. 4.10(b) account for small detunings between the resonator probe signal frequency and the frequency of the lower switch mode $\hat{c}_{-}$. For strong qubit driving, the resonator-resonator coupling increases and converges towards the geometric coupling g_{AB}. We note that for high qubit drive powers, the calculated coupling rates are very sensitive to small uncertainties in the quantities A_{weak} and B_{weak} [cf. Fig. 4.9(c) and Fig. 4.9(d)] since the mean resonator population becomes independent of the coupling rate g_{res} as soon as $g_{\mathrm{res}} \gg \kappa_{\mathrm{A}}, \kappa_{\mathrm{B}}$.

In conclusion, we present a device allowing to tune the coupling between two coplanar stripline resonators via a flux qubit coupled to both of them. We characterize the individual constituents and the switching behaviour by means of spectroscopy and perform a quantitative analysis of the coupler performance using a time domain experiment. From the latter experiments, we find a coupling range of $0.62\,\mathrm{MHz} \leq g_{\mathrm{res}}/2\pi \leq 8.4\,\mathrm{MHz}$. This corresponds to a maximum switching efficiency of 62%. Improved designs are promising candidates for applications in future quantum information processing setups where our coupler can be used for the controlled transfer of excitations between a fast bus resonator, to which additional qubits can be coupled, and a long-lived storage resonator serving as quantum memory. Furthermore, even with its current performance, our coupler may become a key element in quantum simulation architectures such as chains or networks of superconducting nonlinear resonators for the simulation of the Bose-Hubbard-Hamiltonian [40, 43–45, 48, 49].

Summary and Outlook

Circuit quantum electrodynamics (QED) provides a powerful platform for studies in one of the most fundamental research topics in physics, the interaction between light and matter. Over the last decade, the field has developed from proof-of-principle experiments such as the coupling of a single qubit to a single resonator and the demonstration of the strong coupling regime [5] to a powerful toolbox enabling researchers to execute complex measurement protocols [22, 24–26] in architectures comprised of multiple circuit QED building blocks. With increasing complexity of the experimental setups, controlled coupling between adjacent circuit QED building blocks becomes a key requirement. While some circuit QED components such as quantum bits feature intrinsic tunability of their coupling strength to resonators, from which they can be detuned in frequency, the coupling between two fixed-frequency devices such as resonators can only be tuned using dedicated coupler circuits. For future quantum simulation and quantum information protocols [48, 49], tunable and switchable coupling between frequency-degenerate resonators are an important prerequisite. In this work we successfully realize the flux qubit tunable coupler comprised of a three Josephson junction flux qubit coupled galvanically to two frequency-degenerate coplanar stripline resonators.

In the first chapter of this thesis, the theoretical foundations of circuit quantum electrodynamics are provided. Superconducting coplanar waveguide resonators are introduced as the fundamental linear building block of the circuit QED architecture. The input-output formalism provides a powerful method to infer the characteristic parameters of two coupled resonators. Subsequently, the three-Josephson-junction flux qubit is discussed as a non-linear building block of circuit QED coming close to an ideal quantum two-level system. The interaction between a quantized mode of the electromagnetic field and a two-level system is described theoretically by the quantum Rabi Hamiltonian. If the coupling strength is small compared to the mode frequency, the quantum Rabi Hamiltonian reduces to the Jaynes-Cummings-Hamiltonian which provides a valid description of the vast majority of the experiments conducted in the fields of both cavity and circuit quantum electrodynamics. We provide a detailed analysis of the boundaries of the Jaynes-Cummings model. Finally, we discuss the quantum switch, an architecture allowing for tunable and switchable coupling between two superconducting resonators mediated by a flux quantum bit which represents the main objective of this work.

In chapter two, the relevant experimental techniques are introduced. We show how single- and two-tone continuous wave spectroscopy provide insight into the characteristic resonator and qubit transition frequencies of circuit QED architectures and also allow one to calibrate the number of photons in a transmission line resonator. We also discuss the measurement setup and the technical requirements for measurements at millikelvin temperatures. Furthermore, we present the time-domain detection and the pulse generation setup enabling us to analyze the coherence properties of quantum bits.

The prototypical setup of circuit QED is studied experimentally in chapter three. We couple a flux qubit galvanically to a coplanar waveguide resonator where the additional inductance of a Josephson junction placed in the shared branch between qubit and resonator contributes to the qubit-resonator coupling strength. After a characterization in frequency domain by means of transmission spectroscopy, we infer the energy relaxation time of the flux qubit by conducting driven Rabi oscillation measurements. One main goal of this thesis is successfully reached, namely the implementation and test of a measurement setup for time-domain spectroscopy. The qubit-resonator coupling strength observed in our sample motivates a series of experiments where identical qubits and resonators are coupled galvanically and the coupling strength is measured as a function of the critical current of a coupling Josephson junction. We are confident that the latter can not only provide a basis for a thorough theoretical analysis of the influence of such coupling Josephson junctions on the coupling strength but will also pave the way for a systematic insight into the physics of circuit QED architectures with galvanic coupling.

In chapter four, we successfully demonstrate tunable and switchable coupling between two frequency-degenerate coplanar stripline resonators within the quantum switch architecture. The galvanic coupling of the flux qubit to both resonators gives rise to a complex mode structure which we analyze in detail. We observe the phenomenon of ultrastrong coupling and provide an unambiguous proof for the breakdown of the Jaynes-Cummings model. From a fundamental physics point of view, our sample in this way provides important insights into the physics of light-matter interaction beyond the Jaynes-Cummings model. Furthermore, we also study the technological aspects of our sample in the sense of a tool for future quantum information and quantum simulation architectures. Using transmission spectroscopy, we find that the coupling between the two resonators can be tuned by an external magnetic flux applied to the qubit loop. We perform a time-domain experiment to proof the theoretical prediction that the coupling can also be tuned and switched by means of the qubit population which we adjust by a drive pulse with variable amplitude. Our experiments show that the coupling between the resonators can be set to an arbitrary value in the range from $g_{\mathrm{min}}/2\pi = 0.62\,\mathrm{MHz}$ to $g_{\mathrm{AB}}/2\pi = 8.4\,\mathrm{MHz}$ and, in addition, make the switching process directly observable and demonstrate the dependence of the coupling on the interplay between external magnetic flux and qubit population.

Even though the successful realization of the flux qubit coupler adds an important device to the circuit QED toolbox, the coupling range spanning over more than one order of magnitude still leaves room for design improvements. The complex mode structure of our particular sample is of high relevance from a fundamental physics point of view, but a simpler mode structure without the complications of ultrastrong coupling is desirable for using the flux qubit coupler as a tool in future circuit QED setups. We therefore propose to build a flux qubit tunable coupler where the qubit is not coupled galvanically to the signal lines of both resonators. To be able to compensate the geometric coupling with the second-order qubit-mediated coupling, the qubit-resonator coupling strength needs to be sufficiently large. In Ref. [52], qubits were placed in the gap between the signal line and one ground plane of a coplanar waveguide resonator and coupling strengths up to approx. 1 % of the respective mode frequency were reported. We are confident that the coupling strength can be enhanced to sufficiently large values by reducing the distance between qubit and signal line. Furthermore, the geometric coupling between the resonators can be reduced significantly by modifying their geometric layout such that the sections in which the signal lines are in close vicinity are as short as possible. Such improved designs with a structure reduced to the two coupler modes also is a prerequisite for a systematic optimization of the coupler's on/off-ratio. Specifically, the question whether the ultrastrongly coupled transverse mode is limiting the coupler performance of the particular sample discussed in the course of this thesis can be answered.

We would like to stress that even with its current performance, the flux qubit tunable coupler is able to serve as the main building block of architectures for the quantum simulation of the Bose-Hubbard-Hamiltonian [40, 43–45, 48, 49]. For the latter, chains or networks of frequency-degenerate nonlinear microwave resonators are coupled by nearest-neighbor interaction. The corresponding Hamiltonian takes the form [49]

$$\hat{H}_{\mathrm{BH}} = \sum_n \left[\hbar\omega\hat{a}_n^\dagger\hat{a}_n + U\hat{a}_n^\dagger\hat{a}_n^\dagger\hat{a}_n\hat{a}_n + J\left(\hat{a}_n^\dagger\hat{a}_{n+1} + \hat{a}_n\hat{a}_{n+1}^\dagger\right)\right],$$

where ω is the resonator frequency, U is the Kerr nonlinearity and J is the nearest-neighbor coupling energy. In this scenario, two regimes are of particular interest, namely the Mott insulator regime where $U \gg J$, and the superfluid regime where $U \ll J$. While a fixed on-site nonlinearity U can for example be realized by inserting a Josephson junction into each resonator, which adds a current-dependent inductance as shown in Sec. 1.3.1, the flux qubit coupler is an ideal device to provide tunable coupling between adjacent resonators. For a suitable choice of U, the tunability of the flux qubit coupler presented in this thesis is already sufficient to grant access to both the Mott insulator and the superfluid regime *in situ*. The switchability of the coupling, demonstrated in this thesis using a time-domain experiment, even allows for fast transitions between both regimes by applying drive pulses to the coupler qubits.

In conclusion, we are confident that the flux qubit tunable coupler makes an important contribution to the circuit QED toolbox and will find various applications in future quantum simulation and quantum information processing setups. Furthermore, the complex mode structure of the flux tunable coupler and the observation of physics beyond the Jaynes-Cummings model also provide interesting insights into galvanically coupled qubit-resonator systems and motivate further studies on this subject.

List of publications

- A. Baust, E. Hoffmann, M. Haeberlein, M. J. Schwarz, P. Eder, J. Goetz, F. Wulschner, E. Xie, L. Zhong, F. Quijandria, D. Zueco, J.-J. Garcia Ripoll, L. Garcia-Alvarez, G. Romero, E. Solano, K. G. Fedorov, E. P. Menzel, F. Deppe, A. Marx, and R. Gross, *Ultrastrong coupling in two-resonator circuit QED*, arXiv:1501.7372, submitted for publication (2014)

- A. Baust, E. Hoffmann, M. Häberlein, M. J. Schwarz, P. Eder, E. P. Menzel, K. Fedorov, J. Goetz, F. Wulschner, E. Xie, L. Zhong, F. Quijandria, B. Peropadre, D. Zueco, J.-J. Garcia Ripoll, E. Solano, F. Deppe, A. Marx, and R. Gross, *Tunable and switchable coupling between two superconducting resonators*, Phys. Rev. B **91**, 014515 (2015)

- J. Goetz, F. Wulschner, P. Summer, S. Meier, M. Häberlein, C. Zollitsch, M. Fischer, A. Baust, P. Eder, E. Xie, L. Zhong, K. Fedorov, E. P. Menzel, H. Hübl, F. Deppe, A. Marx, and R. Gross, *Geometry-dependent losses in superconducting niobium thin film resonators*, in preparation for publication

- F. Wulschner, J. Goetz, F. R. Kössel, E. Hoffmann, A. Baust, P. Eder, M. Häberlein, M. J. Schwarz, M. Pernpeitner, E. Xie, L. Zhong, C. W. Zollitsch, B. Peropadre, J.-J. Garcia-Ripoll, E. Solano, K. Fedorov, E. P. Menzel, F. Deppe, A. Marx, and R. Gross, *Tunable coupling of transmission-line microwave resonators mediated by an RF-SQUID*, in preparation for publication

- L. Zhong, E. P. Menzel, R. Di Candia, P. Eder, M. Ihmig, A. Baust, M. Haeberlein, E. Hoffmann, K. Inomata, T. Yamamoto, Y. Nakamura, E. Solano, F. Deppe, A. Marx, and R. Gross, *Squeezing with a flux-driven Josephson parametric amplifier*, New. J. Phys. **15**, 125013 (2013)

- E. P. Menzel, R. Di Candia, F. Deppe, P. Eder, L. Zhong, M. Ihmig, M. Haeberlein, A. Baust, E. Hoffmann, D. Ballester, K. Inomata, T. Yamamoto, Y. Nakamura, E. Solano, A. Marx, and R. Gross, *Path entanglement of continuous-variable quantum microwaves*, Phys. Rev. Lett. **109**, 250502 (2012)

- T. Niemczyk, F. Deppe, E. P. Menzel, M. J. Schwarz, H. Huebl, F. Hocke, M. Häberlein, M. Danner, E. Hoffmann, A. Baust, E. Solano, J. J. Garcia-Ripoll, A. Marx, and R. Gross, *Selection rules in a strongly coupled qubit-resonator system*, arXiv:1107.0810

- M. Mariantoni, E. P. Menzel, F. Deppe, M. A. Araque Caballero, A. Baust, T. Niemczyk, E. Hoffmann, E. Solano, A. Marx, and R. Gross, *Planck spectroscopy and the quantum noise of microwave beam splitters*, Phys. Rev. Lett. **105**, 133601 (2010)

- E. P. Menzel, M. Mariantoni, F. Deppe, M. A. Araque Caballero, A. Baust, T. Niemczyk, E. Hoffmann, A. Marx, E. Solano, and R. Gross, *Dual-path state reconstruction scheme for propagating quantum microwaves and detector noise tomography*, Phys. Rev. Lett. **105**, 100401 (2010)

Bibliography

[1] A. Blais, R.-S. Huang, A. Wallraff, S. M. Girvin & R. J. Schoelkopf. Cavity quantum electrodynamics for superconducting electrical circuits: An architecture for quantum computation. *Phys. Rev. A* **69**, 062320 (2004).

[2] M. H. Devoret & R. J. Schoelkopf. Superconducting Circuits for Quantum Information: An Outlook. *Science* **339**, 1169–1174 (2013).

[3] Y. Nakamura, C. D. Chen & J. S. Tsai. Spectroscopy of Energy-Level Splitting between Two Macroscopic Quantum States of Charge Coherently Superposed by Josephson Coupling. *Phys. Rev. Lett.* **79**, 2328–2331 (1997).

[4] Y. Nakamura, Y. A. Pashkin & J. S. Tsai. Coherent control of macroscopic quantum states in a single-Cooper-pair box. *Nature* **398**, 786–788 (1999).

[5] A. Wallraff, D. I. Schuster, A. Blais, L. Frunzio, R.-S. Huang, J. Majer, S. Kumar, S. M. Girvin & R. J. Schoelkopf. Strong coupling of a single photon to a superconducting qubit using circuit quantum electrodynamics. *Nature* **431**, 162–167 (2004).

[6] V. Bouchiat, D. Vion, P. Joyez, D. Esteve & M. H. Devoret. Quantum coherence with a single Cooper pair. *Physica Scripta* **1998**, 165 (1998).

[7] D. J. Wineland. Superposition, entanglement, and raising Schrödinger's cat. Nobel Lecture (2012).

[8] R. G. Hulet, J. C. Bergquist, W. M. Itano, J. J. Bollinger, C. H. Manney & D. J. Wineland. Quantum optics experiments with a single ion. *AIP Conference Proceedings* **172**, 298–303 (1988).

[9] P. Goy, J. M. Raimond, M. Gross & S. Haroche. Observation of Cavity-Enhanced Single-Atom Spontaneous Emission. *Phys. Rev. Lett.* **50**, 1903–1906 (1983).

[10] J. M. Raimond, M. Brune & S. Haroche. Manipulating quantum entanglement with atoms and photons in a cavity. *Rev. Mod. Phys.* **73**, 565–582 (2001).

[11] S. Haroche. Controlling photons in a box and exploring the quantum to classical boundary. Nobel Lecture (2012).

[12] D. P. DiVincenzo. Topics in Quantum Computers. *Mesoscopic Electron Transport. NATO ASI Series E.* **345** (1997).

[13] J. Koch, T. M. Yu, J. Gambetta, A. A. Houck, D. I. Schuster, J. Majer, A. Blais, M. H. Devoret, S. M. Girvin & R. J. Schoelkopf. Charge-insensitive qubit design derived from the Cooper pair box. *Phys. Rev. A* **76**, 042319 (2007).

[14] J. A. Schreier, A. A. Houck, J. Koch, D. I. Schuster, B. R. Johnson, J. M. Chow, J. M. Gambetta, J. Majer, L. Frunzio, M. H. Devoret, S. M. Girvin & R. J. Schoelkopf. Suppressing charge noise decoherence in superconducting charge qubits. *Phys. Rev. B* **77**, 180502 (2008).

[15] A. Houck, J. Koch, M. Devoret, S. Girvin & R. Schoelkopf. Life after charge noise: recent results with transmon qubits. *Quantum Information Processing* **8**, 105–115 (2009).

[16] T. P. Orlando, J. E. Mooij, L. Tian, C. H. van der Wal, L. S. Levitov, S. Lloyd & J. J. Mazo. Superconducting persistent-current qubit. *Phys. Rev. B* **60**, 15398–15413 (1999).

[17] I. Chiorescu, Y. Nakamura, C. J. P. M. Harmans & J. E. Mooij. Coherent Quantum Dynamics of a Superconducting Flux Qubit. *Science* **299**, 1869–1871 (2003).

[18] A. Lupaşcu, C. J. M. Verwijs, R. N. Schouten, C. J. P. M. Harmans & J. E. Mooij. Nondestructive Readout for a Superconducting Flux Qubit. *Phys. Rev. Lett.* **93**, 177006 (2004).

[19] I. Chiorescu, P. Bertet, K. Semba, Y. Nakamura, C. J. P. M. Harmans & J. E. Mooij. Coherent dynamics of a flux qubit coupled to a harmonic oscillator. *Nature* **431**, 159–162 (2004).

[20] T. Yamamoto, M. Neeley, E. Lucero, R. C. Bialczak, J. Kelly, M. Lenander, M. Mariantoni, A. D. O'Connell, D. Sank, H. Wang, M. Weides, J. Wenner, Y. Yin, A. N. Cleland & J. M. Martinis. Quantum process tomography of two-qubit controlled-Z and controlled-NOT gates using superconducting phase qubits. *Phys. Rev. B* **82**, 184515 (2010).

[21] R. C. Bialczak, M. Ansmann, M. Hofheinz, E. Lucero, M. Neeley, A. D. O/'Connell, D. Sank, H. Wang, J. Wenner, M. Steffen, A. N. Cleland & J. M. Martinis. Quantum process tomography of a universal entangling gate implemented with Josephson phase qubits. *Nat Phys* **6**, 409–413 (2010).

[22] M. Mariantoni, H. Wang, T. Yamamoto, M. Neeley, R. C. Bialczak, Y. Chen, M. Lenander, E. Lucero, A. D. O'Connell, D. Sank, M. Weides, J. Wenner, Y. Yin, J. Zhao, A. N. Korotkov, A. N. Cleland & J. M. Martinis. Implementing the Quantum von Neumann Architecture with Superconducting Circuits. *Science* **334**, 61–65 (2011).

[23] A. Fedorov, L. Steffen, M. Baur, M. P. da Silva & A. Wallraff. Implementation of a Toffoli gate with superconducting circuits. *Nature* **481**, 170–172 (2012).

[24] E. Lucero, R. Barends, Y. Chen, J. Kelly, M. Mariantoni, A. Megrant, P. O'Malley, D. Sank, A. Vainsencher, J. Wenner, T. White, Y. Yin, A. N. Cleland & J. M. Martinis. Computing prime factors with a Josephson phase qubit quantum processor. *Nat Phys* **8**, 719–723 (2012).

[25] M. D. Reed, L. DiCarlo, S. E. Nigg, L. Sun, L. Frunzio, S. M. Girvin & R. J. Schoelkopf. Realization of three-qubit quantum error correction with superconducting circuits. *Nature* **482**, 382–385 (2012).

[26] J. Kelly, R. Barends, A. G. Fowler, A. Megrant, E. Jeffrey, T. C. White, D. Sank, J. Y. Mutus, B. Campbell, Y. Chen, Z. Chen, B. Chiaro, A. Dunsworth, I.-C. Hoi, C. Neill, P. J. J. O'Malley, C. Quintana, P. Roushan, A. Vainsencher, J. Wenner, A. N. Cleland & J. M. Martinis. State preservation by repetitive error detection in a superconducting quantum circuit. *Nature* **519**, 66–69 (2015).

[27] Y. Chen, C. Neill, P. Roushan, N. Leung, M. Fang, R. Barends, J. Kelly, B. Campbell, Z. Chen, B. Chiaro, A. Dunsworth, E. Jeffrey, A. Megrant, J. Y. Mutus, P. J. J. O'Malley, C. M. Quintana, D. Sank, A. Vainsencher, J. Wenner, T. C. White, M. R. Geller, A. N. Cleland & J. M. Martinis. Qubit Architecture with High Coherence and Fast Tunable Coupling. *Phys. Rev. Lett.* **113**, 220502 (2014).

[28] A. G. Fowler, M. Mariantoni, J. M. Martinis & A. N. Cleland. Surface codes: Towards practical large-scale quantum computation. *Phys. Rev. A* **86**, 032324 (2012).

[29] R. Barends, J. Kelly, A. Megrant, A. Veitia, D. Sank, E. Jeffrey, T. C. White, J. Mutus, A. G. Fowler, B. Campbell, Y. Chen, Z. Chen, B. Chiaro, A. Dunsworth, C. Neill, P. O'Malley, P. Roushan, A. Vainsencher, J. Wenner, A. N. Korotkov, A. N. Cleland & J. M. Martinis. Superconducting quantum circuits at the surface code threshold for fault tolerance. *Nature* **508**, 500–503 (2014).

[30] C. Eichler, D. Bozyigit, C. Lang, L. Steffen, J. Fink & A. Wallraff. Experimental State Tomography of Itinerant Single Microwave Photons. *Phys. Rev. Lett.* **106**, 220503 (2011).

[31] I.-C. Hoi, T. Palomaki, J. Lindkvist, G. Johansson, P. Delsing & C. Wilson. Generation of nonclassical microwave states using an artificial atom in 1D open space. *Phys. Rev. Lett.* **108**, 263601 (2012).

[32] B. Vlastakis, G. Kirchmair, Z. Leghtas, S. E. Nigg, L. Frunzio, S. M. Girvin, M. Mirrahimi, M. H. Devoret & R. J. Schoelkopf. Deterministically Encoding Quantum Information Using 100-Photon Schrödinger Cat States. *Science* **342**, 607–610 (2013).

[33] L. DiCarlo, M. D. Reed, L. Sun, B. R. Johnson, J. M. Chow, J. M. Gambetta, L. Frunzio, S. M. Girvin, M. H. Devoret & R. J. Schoelkopf. Preparation and measurement of three-qubit entanglement in a superconducting circuit. *Nature* **467**, 574–578 (2010).

[34] C. Eichler, C. Lang, J. M. Fink, J. Govenius, S. Filipp & A. Wallraff. Observation of Entanglement between Itinerant Microwave Photons and a Superconducting Qubit. *Phys. Rev. Lett.* **109**, 240501 (2012).

[35] M. Baur, A. Fedorov, L. Steffen, S. Filipp, M. P. da Silva & A. Wallraff. Benchmarking a Quantum Teleportation Protocol in Superconducting Circuits Using Tomography and an Entanglement Witness. *Phys. Rev. Lett.* **108**, 040502 (2012).

[36] L. Steffen, Y. Salathe, M. Oppliger, P. Kurpiers, M. Baur, C. Lang, C. Eichler, G. Puebla-Hellmann, A. Fedorov & A. Wallraff. Deterministic quantum teleportation with feed-forward in a solid state system. *Nature* **500**, 319–322 (2013).

[37] T. Niemczyk, F. Deppe, H. Huebl, E. P. Menzel, F. Hocke, M. J. Schwarz, J. J. Garcia-Ripoll, D. Zueco, T. Hummer, E. Solano, A. Marx & R. Gross. Circuit quantum electrodynamics in the ultrastrong-coupling regime. *Nat Phys* **6**, 772–776 (2010).

[38] P. Forn-Díaz, J. Lisenfeld, D. Marcos, J. J. García-Ripoll, E. Solano, C. J. P. M. Harmans & J. E. Mooij. Observation of the Bloch-Siegert Shift in a Qubit-Oscillator System in the Ultrastrong Coupling Regime. *Phys. Rev. Lett.* **105**, 237001 (2010).

[39] A. Baust, E. Hoffmann, M. Haeberlein, M. J. Schwarz, P. Eder, J. Goetz, F. Wulschner, E. Xie, L. Zhong, F. Quijandria, D. Zueco, J.-J. Garcia Ripoll, L. Garcia-Alvarez, G. Romero, E. Solano, K. G. Fedorov, E. P. Menzel, F. Deppe, A. Marx & R. Gross. Ultrastrong coupling in two-resonator circuit QED (2014). `arXiv:cond-mat/1412.7372`.

[40] A. A. Houck, H. E. Tureci & J. Koch. On-chip quantum simulation with superconducting circuits. *Nat Phys* **8**, 292–299 (2012).

[41] T. Johnson, S. Clark & D. Jaksch. What is a quantum simulator? *EPJ Quantum Technology* **1**, 10 (2014).

[42] C. M. Wilson, G. Johansson, A. Pourkabirian, M. Simoen, J. R. Johansson, T. Duty, F. Nori & P. Delsing. Observation of the dynamical Casimir effect in a superconducting circuit. *Nature* **479**, 376–379 (2011).

[43] D. G. Angelakis, M. F. Santos & S. Bose. Photon-blockade-induced Mott transitions and XY spin models in coupled cavity arrays. *Phys. Rev. A* **76**, 031805 (2007).

[44] S. Schmidt, D. Gerace, A. A. Houck, G. Blatter & H. E. Türeci. Nonequilibrium delocalization-localization transition of photons in circuit quantum electrodynamics. *Phys. Rev. B* **82**, 100507 (2010).

[45] J. Raftery, D. Sadri, S. Schmidt, H. E. Türeci & A. A. Houck. Observation of a Dissipation-Induced Classical to Quantum Transition. *Phys. Rev. X* **4**, 031043 (2014).

[46] Y. Salathé, M. Mondal, M. Oppliger, J. Heinsoo, P. Kurpiers, A. Potočnik, A. Mezzacapo, U. Las Heras, L. Lamata, E. Solano, S. Filipp & A. Wallraff. Digital quantum simulation of spin models with circuit quantum electrodynamics (2015). `arXiv:quant-ph/1502.06778`.

[47] H. A. Gersch & G. C. Knollman. Quantum Cell Model for Bosons. *Phys. Rev.* **129**, 959–967 (1963).

[48] M. J. Hartmann. Polariton Crystallization in Driven Arrays of Lossy Nonlinear Resonators. *Phys. Rev. Lett.* **104**, 113601 (2010).

[49] M. Leib, F. Deppe, A. Marx, R. Gross & M. J. Hartmann. Networks of nonlinear superconducting transmission line resonators. *New Journal of Physics* **14**, 075024 (2012).

[50] S. Felicetti, G. Romero, D. Rossini, R. Fazio & E. Solano. Photon transfer in ultrastrongly coupled three-cavity arrays. *Phys. Rev. A* **89**, 013853 (2014).

[51] J. Bourassa, J. M. Gambetta, A. A. Abdumalikov, O. Astafiev, Y. Nakamura & A. Blais. Ultrastrong coupling regime of cavity QED with phase-biased flux qubits. *Phys. Rev. A* **80**, 032109 (2009).

[52] T. Niemczyk. *From strong to ultrastrong coupling in circuit QED architectures*. Ph.D. thesis, Technische Universität München (2011).

[53] Y. Yin, Y. Chen, D. Sank, P. J. J. O'Malley, T. C. White, R. Barends, J. Kelly, E. Lucero, M. Mariantoni, A. Megrant, C. Neill, A. Vainsencher, J. Wenner, A. N. Korotkov, A. N. Cleland & J. M. Martinis. Catch and Release of Microwave Photon States. *Phys. Rev. Lett.* **110**, 107001 (2013).

[54] M. Pierre, I.-M. Svensson, S. Raman Sathyamoorthy, G. Johansson & P. Delsing. Storage and on-demand release of microwaves using superconducting resonators with tunable coupling. *Applied Physics Letters* **104**, 232604 (2014).

[55] R. C. Bialczak, M. Ansmann, M. Hofheinz, M. Lenander, E. Lucero, M. Neeley, A. D. O'Connell, D. Sank, H. Wang, M. Weides, J. Wenner, T. Yamamoto, A. N. Cleland & J. M. Martinis. Fast Tunable Coupler for Superconducting Qubits. *Phys. Rev. Lett.* **106**, 060501 (2011).

[56] S. H. W. van der Ploeg, A. Izmalkov, A. M. van den Brink, U. Hübner, M. Grajcar, E. Il'ichev, H.-G. Meyer & A. M. Zagoskin. Controllable Coupling of Superconducting Flux Qubits. *Phys. Rev. Lett.* **98**, 057004 (2007).

[57] T. Hime, P. A. Reichardt, B. L. T. Plourde, T. L. Robertson, C.-E. Wu, A. V. Ustinov & J. Clarke. Solid-State Qubits with Current-Controlled Coupling. *Science* **314**, 1427–1429 (2006).

[58] M. S. Allman, J. D. Whittaker, M. Castellanos-Beltran, K. Cicak, F. da Silva, M. P. DeFeo, F. Lecocq, A. Sirois, J. D. Teufel, J. Aumentado & R. W. Simmonds. Tunable Resonant and Nonresonant Interactions between a Phase Qubit and *LC* Resonator. *Phys. Rev. Lett.* **112**, 123601 (2014).

[59] H. Kamerlingh Onnes. The Superconductivity of Mercury. *Leiden Commun.* **120b, 122b, 124c** (1911).

[60] J. Schuler. *Ferromagnetische Einzelladungs-Transistoren*. Ph.D. thesis, Technische Universität München (2005).

[61] R. Gross & A. Marx. *Festkörperphysik* (Oldenburg Verlag München, 2012).

[62] C. Kittel. *Einführung in die Festkörperphysik* (Oldenbourg Verlag, 2013).

[63] M. J. Schwarz, J. Goetz, Z. Jiang, T. Niemczyk, F. Deppe, A. Marx & R. Gross. Gradiometric flux qubits with a tunable gap. *New Journal of Physics* **15**, 045001 (2013).

[64] D. M. Pozar. *Microwave Engineering* (John Wiley & Sons, New York, 2005), 3rd edn.

[65] R. E. Collin. *Foundations for Microwave Engineering* (Wiley-IEEE Press, New Jersey, 2000), 2nd edn.

[66] R. N. Simons. *Coplanar Waveguide Circuits, Components, and Systems* (John Wiley & Sons, New York, 2001).

[67] M. Göppl, A. Fragner, M. Baur, R. Bianchetti, S. Filipp, J. M. Fink, P. J. Leek, G. Puebla, L. Steffen & A. Wallraff. Coplanar waveguide resonators for circuit quantum electrodynamics. *Journal of Applied Physics* **104**, 113904 (2008).

[68] C. Nguyen. *Analysis Methods for RF, Microwave, and Millimeter-Wave Planar Transmission Line Structures* (John Wiley & Sons, New York, 2001).

[69] D. I. Schuster. *Circuit Quantum Electrodynamics*. Ph.D. thesis, Yale University (2007).

[70] A. D. O'Connell, M. Ansmann, R. C. Bialczak, M. Hofheinz, N. Katz, E. Lucero, C. McKenney, M. Neeley, H. Wang, E. M. Weig, A. N. Cleland & J. M. Martinis. Microwave dielectric loss at single photon energies and millikelvin temperatures. *Applied Physics Letters* **92**, 112903 (2008).

[71] J. M. Martinis, K. B. Cooper, R. McDermott, M. Steffen, M. Ansmann, K. D. Osborn, K. Cicak, S. Oh, D. P. Pappas, R. W. Simmonds & C. C. Yu. Decoherence in Josephson Qubits from Dielectric Loss. *Phys. Rev. Lett.* **95**, 210503 (2005).

[72] A. Megrant, C. Neill, R. Barends, B. Chiaro, Y. Chen, L. Feigl, J. Kelly, E. Lucero, M. Mariantoni, P. J. J. O´Malley, D. Sank, A. Vainsencher, J. Wenner, T. C. White, Y. Yin, J. Zhao, C. J. Palmstrøm, J. M. Martinis & A. N. Cleland. Planar superconducting resonators with internal quality factors above one million. *Applied Physics Letters* **100**, 113510 (2012).

[73] M. Reagor, H. Paik, G. Catelani, L. Sun, C. Axline, E. Holland, I. M. Pop, N. A. Masluk, T. Brecht, L. Frunzio, M. H. Devoret, L. Glazman & R. J. Schoelkopf. Reaching 10 ms single photon lifetimes for superconducting aluminum cavities. *Applied Physics Letters* **102**, 192604 (2013).

[74] D. Cardwell & D. Ginley. *Handbook of Superconducting Materials*. 1 (Institute of Physics, 2003).

[75] A. J. Annunziata, D. F. Santavicca, L. Frunzio, G. Catelani, M. J. Rooks, A. Frydman & D. E. Prober. Tunable superconducting nanoinductors. *Nanotechnology* **21**, 445202 (2010).

[76] T. Orlando & K. Delin. *Foundations of Applied Superconductivity*. Electrical Engineering Series (Addison-Wesley, 1991).

[77] A. Görür & C. Karpuz. Analytic formulas for conductor-backed asymmetric CPW with one lateral ground plane. *Microwave and Optical Technology Letters* **22**, 123–126 (1999).

[78] M. Devoret, B. Huard, R. Schoelkopf & L. F. Cugliandolo. *Quantum Machines: Measurement and Control of Engineered Quantum Systems* (Oxford University Press, Oxford, 2014).

[79] F. Schwabl. *Quantenmechanik* (Springer, Berlin, 1998), 5th edn.

[80] D. F. Walls & G. Milburn. *Quantum Optics* (Springer, 2008), 2nd edn.

[81] M. P. da Silva, D. Bozyigit, A. Wallraff & A. Blais. Schemes for the observation of photon correlation functions in circuit QED with linear detectors. *Phys. Rev. A* **82**, 043804 (2010).

[82] E. Menzel. *Propagating Quantum Microwaves: Dual-path State Reconstruction and Path Entanglement*. Ph.D. thesis, Technische Universität München (2013).

[83] C. Sames, H. Chibani, C. Hamsen, P. A. Altin, T. Wilk & G. Rempe. Antiresonance Phase Shift in Strongly Coupled Cavity QED. *Phys. Rev. Lett.* **112**, 043601 (2014).

[84] M. H. Devoret, A. Wallraff & J. M. Martinis. Superconducting Qubits: A Short Review (2004). `arXiv:cond-mat/0411174`.

[85] B. Josephson. Possible new effects in superconductive tunnelling. *Physics Letters* **1**, 251 – 253 (1962).

[86] J. M. Rowell, P. W. Anderson & D. E. Thomas. Image of the Phonon Spectrum in the Tunneling Characteristic Between Superconductors. *Phys. Rev. Lett.* **10**, 334–336 (1963).

[87] B. K. Likharev. *Dynamics of Josephson Junctions and Circuits* (CRC Press, 1986).

[88] M. Tinkham. *Introduction to Superconductivity*. Dover Books on Physics (Dover Publications, 2004), 2nd edn.

[89] R. Gross & A. Marx. *Applied Superconductivity* (Lecture Notes, 2005).

[90] W. Buckel & R. Kleiner. *Supraleitung* (Wiley-VCH, Weinheim, 2004), 6th edn.

[91] J. Clarke & A. I. Braginski (eds.) *The SQUID Handbook* (Wiley-VCH, Weinheim, 2004).

[92] W. C. Stewart. Current-Voltage Characteristics of Josephson Junctions. *Applied Physics Letters* **12**, 277–280 (1968).

[93] D. E. McCumber. Effect of ac Impedance on dc Voltage-Current Characteristics of Superconductor Weak-Link Junctions. *Journal of Applied Physics* **39**, 3113–3118 (1968).

[94] F. London. *Superfluids* (1950).

[95] R. Doll & M. Näbauer. Experimental Proof of Magnetic Flux Quantization in a Superconducting Ring. *Phys. Rev. Lett.* **7**, 51–52 (1961).

[96] B. S. Deaver & W. M. Fairbank. Experimental Evidence for Quantized Flux in Superconducting Cylinders. *Phys. Rev. Lett.* **7**, 43–46 (1961).

[97] E. Hoffmann. *Experiments on Two-Resonator Circuit Quantum Electrodynamics: A Superconducting Quantum Switch.* Ph.D. thesis, Technische Universität München (2013).

[98] F. Paauw. *Superconducting flux qubits: Quantum chains and tunable qubits.* Ph.D. thesis, TU Delft (2009).

[99] G. Ithier, E. Collin, P. Joyez, P. J. Meeson, D. Vion, D. Esteve, F. Chiarello, A. Shnirman, Y. Makhlin, J. Schriefl & G. Schön. Decoherence in a superconducting quantum bit circuit. *Phys. Rev. B* **72**, 134519 (2005).

[100] F. Deppe. *Superconducting flux quantum circuits: characterization, quantum coherence, and controlled symmetry breaking.* Ph.D. thesis, Technische Universität München (2009).

[101] R. K. Wangsness & F. Bloch. The Dynamical Theory of Nuclear Induction. *Phys. Rev.* **89**, 728–739 (1953).

[102] A. Redfield. On the Theory of Relaxation Processes. *IBM Journal of Research and Development* **1**, 19–31 (1957).

[103] F. Deppe, M. Mariantoni, E. P. Menzel, S. Saito, K. Kakuyanagi, H. Tanaka, T. Meno, K. Semba, H. Takayanagi & R. Gross. Phase coherent dynamics of a superconducting flux qubit with capacitive bias readout. *Phys. Rev. B* **76**, 214503 (2007).

[104] S. Gustavsson, O. Zwier, J. Bylander, F. Yan, F. Yoshihara, Y. Nakamura, T. P. Orlando & W. D. Oliver. Improving Quantum Gate Fidelities by Using a Qubit to Measure Microwave Pulse Distortions. *Phys. Rev. Lett.* **110**, 040502 (2013).

[105] J. Bylander, S. Gustavsson, F. Yan, F. Yoshihara, K. Harrabi, G. Fitch, D. G. Cory, Y. Nakamura, J.-S. Tsai & W. D. Oliver. Noise spectroscopy through dynamical decoupling with a superconducting flux qubit. *Nat Phys* **7**, 565–570 (2011).

[106] C. Rigetti, J. M. Gambetta, S. Poletto, B. L. T. Plourde, J. M. Chow, A. D. Córcoles, J. A. Smolin, S. T. Merkel, J. R. Rozen, G. A. Keefe, M. B. Rothwell, M. B. Ketchen & M. Steffen. Superconducting qubit in a waveguide cavity with a coherence time approaching 0.1 ms. *Phys. Rev. B* **86**, 100506 (2012).

[107] M. Brune, E. Hagley, J. Dreyer, X. Maître, A. Maali, C. Wunderlich, J. M. Raimond & S. Haroche. Observing the Progressive Decoherence of the "Meter" in a Quantum Measurement. *Phys. Rev. Lett.* **77**, 4887–4890 (1996).

[108] S. Haroche & J. M. Raimond. Cavity Quantum Electrodynamics. *Scientific American* **268**, 54–62 (1993).

[109] D. Zueco, G. M. Reuther, S. Kohler & P. Hänggi. Qubit-oscillator dynamics in the dispersive regime: Analytical theory beyond the rotating-wave approximation. *Phys. Rev. A* **80**, 033846 (2009).

[110] T. Lindström, C. H. Webster, J. E. Healey, M. S. Colclough, C. M. Muirhead & A. Y. Tzalenchuk. Circuit QED with a flux qubit strongly coupled to a coplanar transmission line resonator. *Superconductor Science and Technology* **20**, 814 (2007).

[111] I. Rabi. On the Process of Space Quantization. *Phys. Rev.* **49**, 324–328 (1936).

[112] D. Braak. Integrability of the Rabi Model. *Phys. Rev. Lett.* **107**, 100401 (2011).

[113] E. Jaynes & F. Cummings. Comparison of quantum and semiclassical radiation theories with application to the beam maser. *Proceedings of the IEEE* **51**, 89–109 (1963).

[114] B. W. Shore & P. L. Knight. The Jaynes-Cummings Model. *Journal of Modern Optics* **40**, 1195–1238 (1993).

[115] M. O. Scully & Z. M. S. *Quantum Optics* (Cambridge University Press, Cambridge, 1997).

[116] E. Dynkin, A. Yushkevich, G. Seitz & A. Onishchik. *Selected Papers of E.B. Dynkin with Commentary*. Collected Works Series (American Mathematical Society, 2000).

[117] A. Abragam. *The Principles Of Nuclear Magnetism* (Oxford University Press, Oxford, 1961).

[118] A. Wallraff, D. I. Schuster, A. Blais, L. Frunzio, J. Majer, M. H. Devoret, S. M. Girvin & R. J. Schoelkopf. Approaching Unit Visibility for Control of a Superconducting Qubit with Dispersive Readout. *Phys. Rev. Lett.* **95**, 060501 (2005).

[119] F. Bloch & A. Siegert. Magnetic Resonance for Nonrotating Fields. *Phys. Rev.* **57**, 522–527 (1940).

[120] M. Mariantoni, F. Deppe, A. Marx, R. Gross, F. K. Wilhelm & E. Solano. Two-resonator circuit quantum electrodynamics: A superconducting quantum switch. *Phys. Rev. B* **78**, 104508 (2008).

[121] G. M. Reuther, D. Zueco, F. Deppe, E. Hoffmann, E. P. Menzel, T. Weißl, M. Mariantoni, S. Kohler, A. Marx, E. Solano, R. Gross & P. Hänggi. Two-resonator circuit quantum electrodynamics: Dissipative theory. *Phys. Rev. B* **81**, 144510 (2010).

[122] A. Baust, E. Hoffmann, M. Haeberlein, M. J. Schwarz, P. Eder, J. Goetz, F. Wulschner, E. Xie, L. Zhong, F. Quijandría, B. Peropadre, D. Zueco, J.-J. García Ripoll, E. Solano, K. Fedorov, E. P. Menzel, F. Deppe, A. Marx & R. Gross. Tunable and switchable coupling between two superconducting resonators. *Phys. Rev. B* **91**, 014515 (2015).

[123] L. F. Wei, Y.-x. Liu & F. Nori. Generation and Control of Greenberger-Horne-Zeilinger Entanglement in Superconducting Circuits. *Phys. Rev. Lett.* **96**, 246803 (2006).

[124] L. Davidovich, A. Maali, M. Brune, J. M. Raimond & S. Haroche. Quantum switches and nonlocal microwave fields. *Phys. Rev. Lett.* **71**, 2360–2363 (1993).

[125] R. C. Bialczak, M. Ansmann, M. Hofheinz, M. Lenander, E. Lucero, M. Neeley, A. D. O'Connell, D. Sank, H. Wang, M. Weides, J. Wenner, T. Yamamoto, A. N. Cleland & J. M. Martinis. Fast Tunable Coupler for Superconducting Qubits. *Phys. Rev. Lett.* **106**, 060501 (2011).

[126] T. Losinger. *Time-domain control of light-matter interaction with superconducting circuits.* Diploma thesis, Technische Universität München (2012).

[127] M. Pechal, L. Huthmacher, C. Eichler, S. Zeytinoğlu, A. A. Abdumalikov, S. Berger, A. Wallraff & S. Filipp. Microwave-Controlled Generation of Shaped Single Photons in Circuit Quantum Electrodynamics. *Phys. Rev. X* **4**, 041010 (2014).

[128] E. P. Menzel, R. Di Candia, F. Deppe, P. Eder, L. Zhong, M. Ihmig, M. Haeberlein, A. Baust, E. Hoffmann, D. Ballester, K. Inomata, T. Yamamoto, Y. Nakamura, E. Solano, A. Marx & R. Gross. Path Entanglement of Continuous-Variable Quantum Microwaves. *Phys. Rev. Lett.* **109**, 250502 (2012).

[129] L. Zhong, E. P. Menzel, R. D. Candia, P. Eder, M. Ihmig, A. Baust, M. Haeberlein, E. Hoffmann, K. Inomata, T. Yamamoto, Y. Nakamura, E. Solano, F. Deppe, A. Marx & R. Gross. Squeezing with a flux-driven Josephson parametric amplifier. *New Journal of Physics* **15**, 125013 (2013).

[130] P. Roushan, C. Neill, Y. Chen, M. Kolodrubetz, C. Quintana, N. Leung, M. Fang, R. Barends, B. Campbell, Z. Chen, B. Chiaro, A. Dunsworth, E. Jeffrey, J. Kelly, A. Megrant, J. Mutus, P. J. J. O'Malley, D. Sank, A. Vainsencher, J. Wenner, T. White, A. Polkovnikov, A. N. Cleland & J. M. Martinis. Observation of topological transitions in interacting quantum circuits. *Nature* **515**, 241–244 (2014).

[131] T. Niemczyk, F. Deppe, M. Mariantoni, E. P. Menzel, E. Hoffmann, G. Wild, L. Eggenstein, A. Marx & R. Gross. Fabrication technology of and symmetry breaking in superconducting quantum circuits. *Superconductor Science and Technology* **22**, 034009 (2009).

[132] T. Niemczyk, F. Deppe, E. P. Menzel, M. J. Schwarz, H. Huebl, F. Hocke, M. Häberlein, M. Danner, E. Hoffmann, A. Baust, E. Solano, J. J. Garcia-Ripoll, A. Marx & R. Gross. Selection rules in a strongly coupled qubit-resonator system (2011). `arXiv:cond-mat/1107.0810`.

[133] M. Schwarz. *Superconducting Flux Qubits with Tunable Gap.* Ph.D. thesis, Technische Universität München (2011).

[134] Y. Chen, P. Roushan, D. Sank, C. Neill, E. Lucero, M. Mariantoni, R. Barends, B. Chiaro, J. Kelly, A. Megrant, J. Y. Mutus, P. J. J. O'Malley, A. Vainsencher, J.

Wenner, T. C. White, Y. Yin, A. N. Cleland & J. M. Martinis. Emulating weak localization using a solid-state quantum circuit. *Nat Commun* **5**, 5184 (2014).

[135] O.-P. Saira, J. P. Groen, J. Cramer, M. Meretska, G. de Lange & L. DiCarlo. Entanglement Genesis by Ancilla-Based Parity Measurement in 2D Circuit QED. *Phys. Rev. Lett.* **112**, 070502 (2014).

[136] A. Dewes, R. Lauro, F. R. Ong, V. Schmitt, P. Milman, P. Bertet, D. Vion & D. Esteve. Quantum speeding-up of computation demonstrated in a superconducting two-qubit processor. *Phys. Rev. B* **85**, 140503 (2012).

[137] A. Dewes, F. R. Ong, V. Schmitt, R. Lauro, N. Boulant, P. Bertet, D. Vion & D. Esteve. Characterization of a Two-Transmon Processor with Individual Single-Shot Qubit Readout. *Phys. Rev. Lett.* **108**, 057002 (2012).

[138] E. Flurin, N. Roch, J.-D. Pillet, F. Mallet & B. Huard. Superconducting quantum node for entanglement and storage of microwave radiation (2014). `arXiv:quant-ph/1401.5622`.

[139] B. Peropadre, D. Zueco, F. Wulschner, F. Deppe, A. Marx, R. Gross & J. J. Garcia-Ripoll. Tunable coupling engineering between superconducting resonators: From sidebands to effective gauge fields. *Phys. Rev. B* **87**, 134504 (2013).

[140] A. O. Niskanen, Y. Nakamura & J.-S. Tsai. Tunable coupling scheme for flux qubits at the optimal point. *Phys. Rev. B* **73**, 094506 (2006).

[141] A. O. Niskanen, K. Harrabi, F. Yoshihara, Y. Nakamura, S. Lloyd & J. S. Tsai. Quantum Coherent Tunable Coupling of Superconducting Qubits. *Science* **316**, 723–726 (2007).

[142] I.-C. Hoi, A. F. Kockum, T. Palomaki, T. M. Stace, B. Fan, L. Tornberg, S. R. Sathyamoorthy, G. Johansson, P. Delsing & C. M. Wilson. Giant Cross-Kerr Effect for Propagating Microwaves Induced by an Artificial Atom. *Phys. Rev. Lett.* **111**, 053601 (2013).

[143] A. J. Hoffman, S. J. Srinivasan, J. M. Gambetta & A. A. Houck. Coherent control of a superconducting qubit with dynamically tunable qubit-cavity coupling. *Phys. Rev. B* **84**, 184515 (2011).

[144] S. J. Srinivasan, A. J. Hoffman, J. M. Gambetta & A. A. Houck. Tunable Coupling in Circuit Quantum Electrodynamics Using a Superconducting Charge Qubit with a V-Shaped Energy Level Diagram. *Phys. Rev. Lett.* **106**, 083601 (2011).

[145] J. M. Gambetta, A. A. Houck & A. Blais. Superconducting Qubit with Purcell Protection and Tunable Coupling. *Phys. Rev. Lett.* **106**, 030502 (2011).

[146] Y. Makhlin, G. Scohn & A. Shnirman. Josephson-junction qubits with controlled couplings. *Nature* **398**, 305–307 (1999).

[147] M. A. Sillanpää, J. I. Park & R. W. Simmonds. Coherent quantum state storage and transfer between two phase qubits via a resonant cavity. *Nature* **449**, 438–442 (2007).

[148] J. Majer, J. M. Chow, J. M. Gambetta, J. Koch, B. R. Johnson, J. A. Schreier, L. Frunzio, D. I. Schuster, A. A. Houck, A. Wallraff, A. Blais, M. H. Devoret, S. M. Girvin & R. J. Schoelkopf. Coupling superconducting qubits via a cavity bus. *Nature* **449**, 443–447 (2007).

[149] G. Romero, D. Ballester, Y. M. Wang, V. Scarani & E. Solano. Ultrafast Quantum Gates in Circuit QED. *Phys. Rev. Lett.* **108**, 120501 (2012).

[150] I. Lizuain, J. Casanova, J. J. García-Ripoll, J. G. Muga & E. Solano. Zeno physics in ultrastrong-coupling circuit QED. *Phys. Rev. A* **81**, 062131 (2010).

[151] D. Ballester, G. Romero, J. J. García-Ripoll, F. Deppe & E. Solano. Quantum Simulation of the Ultrastrong-Coupling Dynamics in Circuit Quantum Electrodynamics. *Phys. Rev. X* **2**, 021007 (2012).

[152] M. Wallquist, V. S. Shumeiko & G. Wendin. Selective coupling of superconducting charge qubits mediated by a tunable stripline cavity. *Phys. Rev. B* **74**, 224506 (2006).

[153] M. Sandberg, C. M. Wilson, F. Persson, T. Bauch, G. Johansson, V. Shumeiko, T. Duty & P. Delsing. Tuning the field in a microwave resonator faster than the photon lifetime. *Applied Physics Letters* **92**, 203501 (2008).

[154] M. D. Jenkins, U. Naether, M. Ciria, J. Sesé, J. Atkinson, C. Sánchez-Azqueta, E. d. Barco, J. Majer, D. Zueco & F. Luis. Nanoscale constrictions in superconducting coplanar waveguide resonators. *Applied Physics Letters* **105**, 162601 (2014).

[155] F. Terman. *Radio Engineers Handbook* (McGraw-Hill, 1945).

[156] J. Casanova, G. Romero, I. Lizuain, J. J. García-Ripoll & E. Solano. Deep Strong Coupling Regime of the Jaynes-Cummings Model. *Phys. Rev. Lett.* **105**, 263603 (2010).

[157] J. M. Fink, L. Steffen, P. Studer, L. S. Bishop, M. Baur, R. Bianchetti, D. Bozyigit, C. Lang, S. Filipp, P. J. Leek & A. Wallraff. Quantum-To-Classical Transition in Cavity Quantum Electrodynamics. *Phys. Rev. Lett.* **105**, 163601 (2010).

Acknowledgements

This work would not have been possible without the help of the principal investigators and my colleagues at the Walther-Meißner-Institut, our external research partners, and the moral support of my friends and family.

First of all, I would like to express my gratitude to my Ph.D. advisor, **Prof. Dr. Rudolf Gross**. For the last eight years, he gave me the opportunity to be part of the qubit group, first as a working student, then as a diploma student and finally as a doctoral researcher. His office door was always open for me, he was always happy to discuss my research plans and to share his impressive knowledge about solid state physics. I also would like to thank him for supporting my research visit to Tsukuba, Japan and for giving me the opportunity to present my scientific results at various international conferences.

I would like to thank the principal investigators of the qubit group, **Dr. Achim Marx** and **Dr. Frank Deppe** for intensively supporting and mentoring my doctoral project and for their excellent organization of the qubit group. **Dr. Frank Deppe** also initiated my research stay in Japan for which I am very thankful.

I am especially thankful to **Dr. Elisabeth Hoffmann** who developed, fabricated and characterized the flux qubit coupler and who encouraged me to do further research on her sample. It is her groundwork on which this thesis is built and it it safe to say that without her flux qubit coupler sample this thesis would not be finished by now. Furthermore, I would like to thank Elly for two great years of joint research in the qubit lab.

Max Häberlein has fabricated the flux qubit sample which provided the basis of the successful implementation of the time domain measurement setup.

I am grateful towards **Dr. Edwin Menzel**, **Max Häberlein** and **Dr. Elisabeth Hoffmann** for their thorough and efficient work when we upgraded the qubit lab's cryostat.

Even though not directly involved in my doctoral project, **Dr. Hans Huebl** always was willing to discuss my measurement results and to share his knowledge about time domain measurements.

I would like to thank my present and former colleagues of the qubit group, **Michael Fischer, Jan Goetz, Max Häberlein, Dr. Elisabeth Hoffmann, Dr. Tomasz Niemczyk, Dr. Manuel Schwarz, Friedrich Wulschner, Edwar Xie** and **Ling Zhong**, the principal investigators **Dr. Hans Huebl, Dr. Edwin Menzel, Dr. Kirill Fedorov, Dr. Frank Deppe** and **Prof. Dr. Rudolf Gross** and our master students for the great working atmosphere in the WMI qubit group. Their helpfulness and their willingness to share their knowledge was always motivating and encouraging to me.

I would like to express my gratitude towards the group of **Prof. Jaw-Shen Tsai, Ph.D.** and his colleagues at the NEC Smart Energy Research Laboratories in Tsukuba, Japan for giving me the opportunity to do research in their labs for two months. I would especially like to mention **Tsuyoshi Yamamoto, Ph.D., Kunihiro Inomata, Ph.D.** and **Koichi Kusuyama** for their outstanding support and supervision during my stay. Besides the scientific part of my visit, it was a great honor for me to experience the Japanese culture and the Japanese hospitality. Arigatō gozaimasu!

The best experimentalist would be lost without the help of theoretical physicists. In that sense, I would like to thank **Prof. Dr. Enrique Solano, Dr. Guillermo Romero, Laura García-Álvarez, Dr. Juan-Jose Garciá Ripoll** and **Dr. David Zueco** for their theoretical support and for the many helpful telephone conferences we had over the last years.

I also would like to thank my diploma students M**arta Krawczyk** and **Thomas Losinger** for their thorough work which also helped to bring my doctoral project forward.

My office partners **Dr. Manuel Schwarz, Johannes Lotze, Reinhard Rossner, Peter Eder** and **Michael Fischer** are to be thanked for the great atmosphere in our office and for the daily cheerful chit-chat.

The WMI workshop staff under the direction of **Helmut Thies** has made an important contribution to this work as they fabricated most parts of the cryostat and the sample packages. Their impressive technical and engineering skills allowed to put the qubit lab's cryostat back into operation in the shortest possible time.

I would like to thank **Emel Dönertas** and **Ludwig Ossiander** for taking care of all administrative tasks in an exemplary way and thus allowing the researchers at WMI to focus on their scientific challenges.

I would like to thank **Dr. Jinming Lu** and **Dr. Sergej Truschin** for true friendship. When things again were not going well in my doctoral project or in my private life, they were always there to listen to me when I needed someone to talk to. And they always reminded me that there is life beyond the lab.

Finally I would like to express my deepest gratitude to my parents **Margot and Werner Baust**. It is their support which provided the basis for this thesis. When I decided to become a physicist more than ten years ago, I could not imagine the challenges I would face. It was to my parents where I could bring all my sorrows, fears, worries and sometimes even desperation which did not make life easier for my parents. Nevertheless, they never stopped encouraging me to pursue my goal of earning a doctoral degree in physics and to look ahead despite all obstacles my studies had set for me. Today, when they hold these pages in their hands, I hope they will realize that it was all worth it. Thank you so much.